Technische Universität München
Fakultät für Elektrotechnik und Informationstechnik
Lehrstuhl für Hochfrequenztechnik

Frequency Selective Surfaces Using Tightly Coupled Miniaturized Metamaterial Resonators

Safiullah Khan

Vollständiger Abdruck der von der Fakultät für Elektrotechnik und Informationstechnik der Technischen Universität München zur Erlangung des akademischen Grades eines

- Doktor-Ingenieurs -

genehmigten Dissertation.

Vorsitzender:	Prof. Dr.-Ing. Gerhard Rigoll
Prüfer der Dissertation:	1. Prof. Dr.-Ing. Thomas F. Eibert
	2. Prof. Dr. rer. nat. Alessio Gagliardi,

Die Dissertation wurde am 16.10.2019 bei der Technischen Universität München eingereicht und durch die Fakultät für Elektrotechnik und Informationstechnik am 23.03.2020 angenommen.

Printed and/or published with the support of the German Academic Exchange Service.

To my beloved parents, siblings and dear ones

Acknowledgments

All praises be to Allah the Almighty, the most Gracious and the most Merciful. He is the Creator of everything tangible and intangible, visible and invisible, love and fear, thoughts and emotions, and the things that a man can not perceive today. His knowledge is beyond measures. It was His blessing and kindness without which the presented work would not have been possible.

The research for this dissertation was conducted in the Chair of High-Frequency Engineering at the Department of Electrical and Computer Engineering of Technical University of Munich. The financial support for the work was provided by the Deutscher Akademischer Austauschdienst (DAAD).

I would like to thank my advisor Prof. Dr.-Ing. Thomas Eibert for his constant support, guidance, feedback, counsel, and encouragement at each and every step. I am grateful to him for his compassionate and understanding behavior throughout my doctoral research journey. I will always remember him and the enriching discussions we had about different academic as well as non-academic topics with meaningful impact on my personality. I express my heartiest gratitude to Prof. Eibert who put enough confidence in me to complete this work.

I am deeply thankful to my parents and family for their prayers, motivation and moral support. I appreciate the cooperation and support provided by Dr. Uwe Siart during my research to resolve my issues. I must also express my gratitude to all my colleagues Thomas Mittereder and Dr. Gerhard Hamberger for their support in fabrication of the structures, Arslan Azhar, Daniel Ostrzyharczik, Fabian Faul, Faisal Bashir, and Dr. Ilya Sukharevsky for great discussions during lunch breaks, Alexander Paulus, Jonas Kornprobst, Joseph Knapp, Mehmet Taygur, and Ole Neitz for making conference trips memorable, Bernd Hofmann, Björn Möhring, Clemens Moroder, Christian Koenen, Christoph Eisner, Carlos Lopez, Raimund Mauermayer, Dr. Simon Adrian for their pleasant and sportive company.

Finally, I am thankful to Dr. Anwar Ul Haq, Faisal Ikhlaq, Dr. Rameez Hayat, Turab Ul Hassan, and other friends for their contribution in various ways and with whom I shared some of the memorable moments of my life during my stay in Munich.

Safiullah Khan
Munich, Germany
September, 2019

Abbrevations and Symbols

AC	alternating current
A	absorption
A_e	absorption efficiency
AIS	artificial impedance surface
$\boldsymbol{B}$	magnetic flux density
B_w	bandwidth
c	speed of light which equals to 3.0×10^8 m/s
$\boldsymbol{C}$	capacitance
C_e	conversion efficiency
DC	direct current
$\boldsymbol{D}$	electric flux density
$\boldsymbol{E}$	electric field
EM	electromagnetic
EMI	electromagnetic interference
EMC	electromagnetic compatibility
FET	field effect transistor
FSS	frequency selective surface
$\boldsymbol{H}$	magnetic field
H_e	harvesting efficiency
HEMT	high-electron-mobility transistor
$inc.$	incident wave
IL	insertion loss
$\boldsymbol{J}$	electric current density
L	inductance
LH medium	left hand medium
LHCP	left hand circular polarization
MTM	metamaterial
$\boldsymbol{M}$	magnetic current density
MPT	microwave power transmission
n	refractive index
NIM	negative index media
PSS	polarization selective surface
PEC	perfect electric conductor
PMC	perfect magnetic conductor
PER	polarization extinction ratio
PCR	polarization conversion ratio

$P_\circ$	output power
P_{in}	input power
P_a	power absorbed by metamaterial unit cell
P_l	power delivered to load
P_r	power incident per square unit
p_s	average unit cell size
p	inter-element spacing
Q_l	loaded quality factor
Q_u	unloaded quality factor
Q_e	external quality factor
QEU	quad element unit
RH medium	right hand medium
RSRR	rectangular split-ring resonator
RL	return loss
RCS	radar cross-section
$ref.$	reflected wave
$\boldsymbol{S}$	Poynting vector
SEU	single element unit
SSPS	space solar power satellite
SRR	split-ring resonator
S_{ii}	reflection coefficient at port i
S_{ij}	transmission coefficient from port j to port i
TW	thin-wire
TE	transverse electric
TM	transverse magnetic
TRL	through-reflect-line
$trans.$	transmitted wave
v_p	phase velocity
v_g	group velocity
V_{gs}	source voltage
V_{dg}	drain voltage
WSN	wireless sensor network
WPT	wireless power transmission
$Z_\circ$	characteristic impedance
Z_{in}	input impedance

α	attenuation
β	phase constant
γ	complex propagation constant
ε_r	relative permittivity
$\varepsilon_\circ$	free space permittivity which equals to $8.858 \times 10^{-12}\,\mathrm{F/m}$
ζ	damping factor
η	ellipticity
η_z	intrinsic impedance
Γ	reflection coefficient
θ_r	angle of reflection
θ_{inc}	incidence angle
κ	chirality
λ_{LC}	LC resonance wavelength
λ_g	operating wavelength
μ_r	relative pemeability
$\mu_\circ$	free space permeability which equals $4\pi \times 10^{-7}\,\mathrm{H/m}$
ρ	electric charge density
ϱ_m	magnetic charge density
$\nabla\times$	curl operator
$\nabla\cdot$	divergence operator
∇^2	Laplace operator
τ	transmission coefficient
χ	reciprocity
ω_{LC}	LC resonance frequency
ω_{pe}	electric plasma frequency
ω_{pm}	magnetic plasma frequency

Abstract

The concept of metamaterials and miniaturization is extended by using distinct types of resonators in a single unit cell to introduce mutual coupling for electromagnetic wave manipulation. Using distinct types of resonators gives a multi-band response, strong mutual coupling, compact unit cell, and tunability. The resonance frequencies can be controlled independently with very few design parameters. In this context a novel unit cell is designed to show the benefits of multi-resonant metamaterial structures, especially on the performance characteristics of frequency selective surfaces, polarization rotators and converters, absorbers, waveguide filters, and energy harvesters.

The unit cell has an electrically small size rectangular split-ring resonator coupled together with a T-type resonator. Thin, planar, dual-band frequency selective surfaces are designed by arranging the unit cells in a periodic array with three geometric configurations to operate in the X and Ku-bands. The first two configurations are single layer designs. In a first design configuration, the frequency selective surface is designed with a single unit cell structure to have a polarization dependent response. The second design configuration has a 2×2 supercell with four unit cells, rotated by 90° to achieve a rotationally symmetric structure for polarization independent behavior. The structures show incident angle stability in the transmission mode with very low insertion loss. In addition, the second configuration has strong polarization stability as well at the resonance frequencies. CST Microwave Studio is used for full-wave simulation of the frequency selective surfaces with periodic boundary conditions in x- and y-direction and Floquet ports in the direction of propagation. For the experiments, a dipole excited ultrawideband dielectric rod antenna with reflector is used as a quasi plane wave source in a free-space bistatic transmit-mode measurement setup. The frequency selective surfaces are also investigated as filters within a rectangular hollow waveguide. Futhermore, to use the frequency selective surface as a perfect absorber, it is optimised to obtain large absorption of incident waves at 7.82 GHz. Simulated and measured results are compared and good agreement is found. It is found that the mutual coupling between the coupled resonators in a unit cell can be used to control the resonance frequencies.

In a third configuration, a polarization conversion screen is designed by utilizing the mutual interactions between the two distinct types of resonators. In order to enhance the cross polarization conversion, the unit cell is rotated by 90° to obtain a chiral geometry and the right diagonal elements are scaled down to construct a rotationally asymmetric 2×2 supercell. The supercells are arranged periodically on either side of the substrate. In the bottom layer, each element is rotated by 90° with respect to the corresponding element in the top layer to achieve an asymmetric transmission property and to introduce

the desired phase difference between the two orthogonal linear vector components of the transmitted wave. The presented design has two layers and exhibits very good circular polarization efficiency, which is primarily achieved by transverse mangetic dipole-magnetic dipole coupling. The polarizer has an ellipticity of 44.4° and a polarization extinction ratio of 37.30 dB at 14.79 GHz. Furthermore, the polarization conversion ratio for both linear orthogonal components is identical at this frequency. At 9.15 GHz strong orthogonal polarization rotation is observed. The electrical size of the unit cell is $0.25\lambda_0 \times 0.25\lambda_0 \times 0.035\lambda_0$.

The unit cell design has been further investigated for advanced energy harvester solutions with high efficiencies and low power handling capabilities. The design is presented for single-band and dual-band functionalities, which support the realization of smart sensor node concepts within widely distributed sensor networks. In single-band design, both the resonators are physically joined such that a single absorption band is produced. The structure resonates at 6.75 GHz and captures the incident electromagnetic waves. Perfect impedance matching is implemented to channel the captured electromagnetic power to the load. About 92.2% of the incident power is captured from which 78.3% of the energy is converted to real power in the resistive load of 490 Ω at 6.75 GHz. The total efficiency amounts to 72.2%. Investigations for oblique angles of incidence show stability up to 45°. In the dual-band design, each resonator has an individual resonance frequency. The resonance frequencies are 7.16 GHz and 9.25 GHz and they can be controlled independently with very few parameters. The power conversion efficiency and the power harvesting efficiency for the structure at resonance frequencies (7.16 GHz, 9.25 GHz) are (74.7%, 65.6%) and (60.5%, 51%), respectively. The structures are backed by a metal film. A via on the resonators is used to divert the current to resistive loads.

Contents

List of Figures

List of Tables

CHAPTER 1

Introduction

The advancement in wireless communication technology is markedly seen in defence and commercial applications. In military ships, the top of the mast is loaded with multifunctional radars, satellite communication systems, and sensors operating in the same or nearby frequency bands. Degradation of performance in such applications is highly undesirable. In commercial applications, it is likely that the spectrum in which more and more wireless devices are used becomes saturated. The increasing number of radiating sources may cause interference and due to the increase in the number of devices operating in the same band, mutual interference will occur [AJH14, SIP14, KON11]. In such cases, apart from useful techniques of limiting the coverage area (reducing the cell size / multi-beam forming) or establishing point-to-point connections, an efficient technique would be to use frequency selective surfaces (FSSs) to increase the capacity and reduce the interference [GKRW06, Wu14, Mit04]. FSSs can keep a wireless system isolated from undesired radiation.

FSSs are used to allow certain bands of frequencies to pass with a good transmission coefficient and to block other out-of-band frequencies or vice-versa [Mun05]. The characteristics that evaluate the performance and determine the advantage of using FSSs are high selectivity, polarization stability, incident angle stability, behavior at harmonic frequencies, low loss, and thickness, etc. [WC16, ZHW+14, DLPG07, EFCD10]. FSSs can be designed as filters with band-pass, band-stop, high-pass or low-pass behavior, such as in microwave filters used in waveguides [YZXYJ14, HKS15, EAA15]. FSSs have been widely used as antenna radomes to reduce the radar cross section of antennas as well as for polarization conversion and tuning, beam shaping, gain improvement, or electromagnetic shielding to avoid mutual coupling [LHW+15, HHS+13, THC13, GLS+19, AGF+16, GYM+18, CLL+15, LWZ+10]. FSSs are also used in reflectarrays, transmitarrays and insertions for waveguide filters. They play an important role in satellite communication

and radar systems where multi-band responses are required for applications such as military, and meteorology, etc. It is highly desirable to operate in multi-bands without replacing the feed. In the simplest configuration a subreflector is used along with the main reflector.

Frequency filtering can be implemented by integrating filters into the antenna feeding systems. However, this approach is not favorable due to space constraints in systems, where antenna elements are small compared to the wavelength of operation. Also, the design complexity increases if there are multiple feed lines as, e.g., in phased arrays. In this context, using a spatial filter to block the incident signals from approaching the antenna aperture is beneficial and reduces complexity.

When designing FSSs, problems of undesired coupling, band edges, roll-off and large spaces between the resonating bands need to be considered. These problems have been addressed and eliminated by using lumped elements (capacitively loaded ring) [XZZW08]. The main drawbacks of this solution are the limitations associated with the capacitors. The values of the loaded capacitors will limit the separation between the bands and a large number of capacitors may be required for large FSS panels. Some of the other design procedures to construct multiband FSSs include multilayered structures, single layered perturbed structures, multi-resonant structures, fractal structures, and substrate integrated waveguide technology etc. [WC16, VHS93, Del12, YWM$^+$16, OS17]. Recently, the use of liquid crystal materials have opened up an approach that enables the voltage controlled reconfiguration and/or tunability of the FSSs. The permittivity and dielectric loss of liquid crystals is a function of the applied voltage.

FSSs composed of resonators with metallic elements can be used on curved surfaces due to sufficiently small element sizes. FSSs also reduce grating lobes in the operating band, which may otherwise occur. Mulitlayered techniques were first used in [VHS93, WM99]. In [Del12, MMZ09], layers with multi-periodicity and multi-resonant elements have been used to design FSSs. Multilayer designs can provide high selectivity and sharp band edge roll-offs, where mutual coupling among the different layers must, however, carefully be considered in the design process. The cascading technique improves the filter order but results in a more bulky and thicker structure. Moreover, the frequency dependence may vary considerably with the angle of incidence. In single-layer higher-order designs, the number of identical resonators in a unit cell are increased to increase the order of the FSS and different resonators are used to achieve multiband response. With complicated geometries of the resonators it may be very challenging to cope with the coupling effects to obtain a desired response. FSSs can also be realized by printing metallic patches and wire grids on either side of a dielectric substrate to construct a multilayered FSS, as, e.g., done in [SB07]. The demonstrated FSS had a single transmit band in the $(2-20)$ GHz frequency range and was sensitive to the incident angle. The substrate-integrated waveguide technique has also been used in [WC16, LHT$^+$07]. However, new

structure designs with single-layer technology and operating in multiple bands are still being proposed using passive resonating elements for miniaturization of FSSs. Therefore, the design of a single-layer metamaterial (MTM) multiband FSS, controlling the propagation direction and polarization of electromagnetic waves, provides motivation to design and fabricate structures for the microwave and terahertz (THz) frequency regime.

In wireless communication systems, polarization mismatch at the receiver antenna can impact the systems' propagation link budget. For example, in satellite communication a linearly polarized wave may experience rotation while propagating through the atmosphere. This effect is called Faraday rotation and it can affect the link budget [LA02]. Thus, a linearly polarized wave is not always suitable for transmission. Some other issues associated with linearly polarized waves are multipath fading and receiver antenna orientation. Under such circumstances, circular polarization is preferred because it shows strong immunity to environmental effects. This provides an opportunity to explore structures, which can perform linear-to-circular polarization conversion efficiently because it is not always convenient to generate circularly polarized waves at element level in planar radiating arrays. For this purpose, FSSs are a convenient solution as they can be used on top of the arrays at very small distances.

Polarization selective surfaces (PSSs) are a type of FSSs that can convert the polarization of an incident wave in a certain band of frequencies and leave the polarization state of the out-of-band frequencies unchanged [CCZ+13, LWLG16]. It is important to understand the difference between a polarization converter and a rotator. In a polarization rotator, the out-going wave has the same polarization state as the incoming wave, but the plane of polarization is rotated by a certain angle for the out-going wave. In a polarization converter, the polarization state of the out-going wave is changed, i.e., linear polarization to circular polarization. Using polarization converters on top of a linearly polarized antenna allows to separate the antenna array design and the creation of circularly polarized waves.

Polarization conversion occurs because of a phase difference between the orthogonal components of a reflected or a transmitted wave. The phase difference can be artificially achieved in different ways: 1) by using an anisotropic chiral structure geometry [FMP+06], whose no-mirror symmetry ensures the twisting response [FGBV17], i.e., 2D Archimedes spiral or 3D helix; 2) by using a cascaded capacitive impedance layer and an inductive impedance layer, both having a different response for the two orthogonal components of an incident electromagnetic (EM) wave [AB16], leading to a phase difference of 90° after tuning; and 3) by using an active metasurface which has embedded varactor diodes to impose a phase difference between the orthogonal components of the incident plane wave [GYM+18].

Due to the importance of polarization converters based on FSSs, many designs have

been presented by researchers. A comparative study of various designs of flexible chiral metamaterials for the terahertz regime was presented in [KZS+12]. Chiral properties, such as optical activity (polarization rotation of the linearly polarized wave), circular polarization generation, circular dichroism (the absorption difference between right- and left-handed circularly polarized waves) and filtering capabilities, for the designs were compared. Large optical activity in all the designs was observed, but the ellipticity remained below 35°. In [CCZ+13], a tri-layered metasurface was proposed to achieve polarization rotation. The metallic gratings on each layer were successively rotated by 0°, 45°, and 90° to demonstrate rotation of the incident linearly x-polarized wave to the transmitted linearly y-polarized wave. Recently, polarization converters based on triple twisted SRRs, substrate integrated waveguides, and miniaturized-element FSSs have been proposed [CWCG16, JASS18, AB16]. Most of the work has been focused around single-band polarization conversion. Multilayered structures have been used where an increase in the bandwidth or multi-band operation was reported [ZZHM17, LZL+17]. A better and wider axial ratio could also be achieved. However, this approach introduces higher insertion loss and may increase the return loss due to poor matching. Multilayered structures also require careful fabrication and alignment. The quantities insertion loss and return loss are important factors while designing structures for radar applications and satellite communication [HH17]. For example, in an imaging system, poor matching will damage the quality of the image due to multiple interactions within the system [DLPG07].

In the context of the above discussion, in this thesis a unique metamaterial unit cell is designed, investigated and used in single-layer FSSs and double-layer PSS designs for X- and Ku-band. An equivalent circuit model for the FSS is presented, which depicts the topology of a dual band-stop microwave filter and includes the effects of mutual coupling as well. In the multi-resonator based, double-layered PSS design longitudinal dipole-dipole coupling and transverse (interlayer) coupling are exploited to achieve high cross polarization transmission. Moreover, the unit cell design is used to harvest electromagnetic energy with good angle stability.

The content of the thesis is organized as follows: Chapter 2 discusses the state-of-the-art about metamaterials and important concepts that are used in this thesis. It also discusses the LC equivalent circuit construction for a planar resonator. Chapter 3 discusses the fundamentals of frequency selective surfaces and defines the design objectives for frequency selective surfaces. The development of a unique unit cell, its equivalent circuit, and periodic arrangement to form frequency selective surfaces are presented in Chapter 4. It also discusses the application of frequency selective surfaces as waveguide filters and microwave absorbers. Chapter 5 presents the polarization selective surface design and its tunability. Chapter 6 presents the state-of-the-art, motivation, and single-band and multi-band energy harvester systems with performance analysis. A summary of the thesis is given in Chapter 7.

CHAPTER 2

Background of Metamaterials

After the discovery of the split-ring resonator (SRR) [SPV+00] and the experimental verification of a negative index of refraction [SSS01], composite materials gained considerable attention among researchers over the past two decades. Such composite structures are also known as metamaterials. It is very interesting for engineers and researchers to design structures, which give freedom to control their electromagnetic response. In this thesis metamaterials are discussed in the context of frequency selective surfaces. Therefore, this chapter briefly discusses the history, which led to the experimental demonstration of negative index materials; a classification of materials, definition and types of such composite materials, wave interaction with materials, and towards the end, metamaterial inspired applications.

2.1 History

The discovery of radio waves, which was reported by Hertz in 1888 led to a series of experiments with these waves. In 1898, twisted structures were used by Jagadis Chunder Bose to rotate the polarization of electric waves[1] [BS98]. In 1914, Lindman performed a first experiment to look for radio wave activity [LSTV94]. The experiment used twisted small helices made from copper wires and positioned them arbitrarily with random orientation in a cardboard box. He observed polarization rotation by measuring

[1] The term "electric waves" was perhaps used because a single spark from an electric discharge produced a flash of radiation in the experiment performed.

a linearly polarized transmitted wave as a function of the angle of rotation of the receiver antenna, which was also linearly polarized [Lin20]. The basis for this work was that a molecular dissymmetry produces optical activity so the synthesis of materials, which cause such phenomena, were to be investigated. Today, these materials are known as artificial chiral media. In 1945, it was Mandelshtam who directed the attention of the scientific community to the existence of a medium whose group velocity and phase velocity has opposite direction for a certain range of frequencies. In order to support his view, he considered wave propagation in crystal lattices where the wavelength of the wave is larger than the lattice constant [Man45]. In 1948, Kock presented metallic delay lenses in which focusing was achieved by reducing the phase velocity of radio waves passing through the lens. The lenses were made by periodically arranging conducting strips, disks, and spheres to tailor the effective refractive index of the artificial medium [Koc48]. In 1951, Malyuzhinets studied backward-wave media and showed that the phase velocity of waves point toward the source from infinity. He presented an equivalent transmission line model for a backward propagating wave with series capacitance and shunt inductances [Mal51]. In 1957, Sivukhin discussed the general properties of backward-wave media. He noticed that backward-wave media are continuous and homogenous with negative permittivity and permeability [Siv57]. Until the 1960s, microwave tubes were designed from backward-wave structures and the negative refraction phenomenon had been discovered, but theoretical explanations were still insufficient [CSL10]. A major step forward was made by Veselago in 1967. He proposed the concept of materials with simultaneous negative permittivity (ε) and permeability (μ). He termed these materials as left-handed (LH) materials. The term LH was used to indicate the fact that the phase velocity is negative compared to that in normal materials. This means that the electric field, the magnetic field, and the phase constant vectors make a left-hand triad. Alternatively, for a plane wave in a LH medium the phase velocity and the Poynting vector have opposite directions, unlike in conventional materials (discussed in Section 2.5). He also discussed some new features, i.e., backward Cerenkov radiation and Doppler shift [Ves68].

The ambition to create a perfect lens required the synthesis of an artificial material with some specific properties that are not available in natural materials. Pendry et al. after almost three decades revived this topic. In 1996, they proposed that metallic wires with a specific radius arranged periodically in an array with a specific spacing produce an electromagnetic response of negative permittivity (the medium is also called artificial electric plasma) [PHSY96]. Three years later, metallic split-rings were proposed which produce a negative permeability for a certain frequency band (the medium is also called artificial magnetic plasma) [PHRS99]. Electromagnetic response characterization of lattices of rings and wires was a significant achievement and perhaps the first revolution on LH media. It was the year 1999 when the term "metamaterial" was coined by Rodger Walser [CSL10]. The realization of simultaneously negative permittivity and permeability was still a challenge. In 2000, Smith et al. came up with the design to create such a structure. Metallic wire and split-ring were combined together to form a unit cell, which

produced negative permittivity due to the wire element and negative permeability due to the ring element [SPV+00]. The composite unit cell was arranged periodically to achieve the response that was predicted by Veselago over thirty years ago. This way artificial materials proposed by Pendry et al. led to the creation of composite materials, which are also known as metamaterials. In the following year, the design was modified to experimentally demonstrate the negative index of refraction [SSS01]. Since then metamaterial based designs have been extensively used for a wide range of applications [AHR15, CCJC10, CCZ+13, Che12].

2.2 What are metamaterials?

In the historical development different terminologies have been used by researchers before the term metamaterial was introduced. In modern days the word "metamaterial" is used in the design of antenna arrays and elements, filters, and feeding lines etc., without a solid understanding of the term. It will be fair to say that metamaterials are not a technology itself, but a technology enabling design philosophy. It is essential to understand that many well known and familiar "ordinary" materials which were previously called random, composite, and inhomogeneous materials may well be classified as metamaterials [ZSA02]. The word metamaterial is a combination of the Greek word *meta*, meaning "beyond" and the Latin word *materia*, meaning "material or matter". So metamaterial would mean beyond naturally occurring materials. Some of the definitions of metamaterials found in literature are

> 1. "Metamaterials are macroscopic composites having a man-made, three-dimensional, periodic cellular architecture designed to produce an optimized combination, not available in nature, of two or more responses to a specific excitation." [Mun09, CSL10]

> 2. "Electromagnetic metamaterials are artificial effectively homogeneous electromagnetic structures with unusual properties not readily available in nature." [CI05]

Numerous other definitions can be found in [ZSA02], all the definitions mention certain properties of metamaterials, but not all. Almost all the definitions mention two important properties that the material should exhibit:

- electromagnetic properties that are not found in nature, and/or
- electromagnetic properties different than those of the constituent materials.

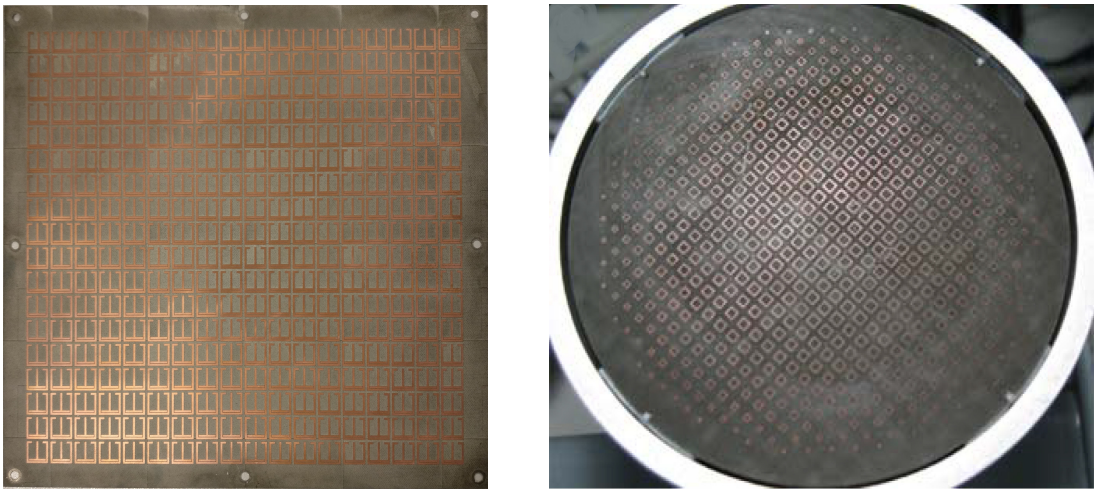

(a) **(b)**

Figure 2.2.1: Typical subwavelength sized metamaterial designs (a) a periodic structure (b) a non-periodic structure [CSL10].

A structure whose structural average cell size (p_s) is much smaller than the wavelength of operation (λ_g) is called an *effectively homogeneous* electromagnetic structure. In order to have a medium in which phenomena of refraction dominate over diffraction or scattering it is recommended that the medium obeys the $p_s \leq \lambda_g/4$ condition. Thus, the medium is *electromagnetically uniform* along the propagation direction [CI05].

In 2010, Smith et al. [CSL10] presented another definition:

3. "A metamaterial is a macroscopic composite of periodic or non-periodic structure, whose function is due to both the cellular architecture and the chemical composition."

It can be said that the extra ordinary properties of metamaterial structures are primarily due to both the *cellular architecture* and the *constituting materials*. Moreover, a metamaterial will be regarded as an effective medium when the cellular size is equal to or smaller than subwavelength ($\lambda_g/4$). In this thesis, unit cells are designed to be much smaller than the operating wavelength, i.e., they have subwavelength dimensions. Fig. 2.2.1 shows examples of metamaterial structures. Fig. 2.2.1(a) represents a homogeneous medium that is also equivalent to a periodic structure because of the arrangement of the subwavelength unit cells. Fig. 2.2.1(b) represents an inhomogeneous medium that is equivalent to a gradient medium or non-periodic structure. The dependence on the cellular architecture allows metamaterials to control the electromagnetic properties using its geometrical parameters. However, the properties are also dependent on the type of substrate used for metallization and, therefore, it must be chosen carefully.

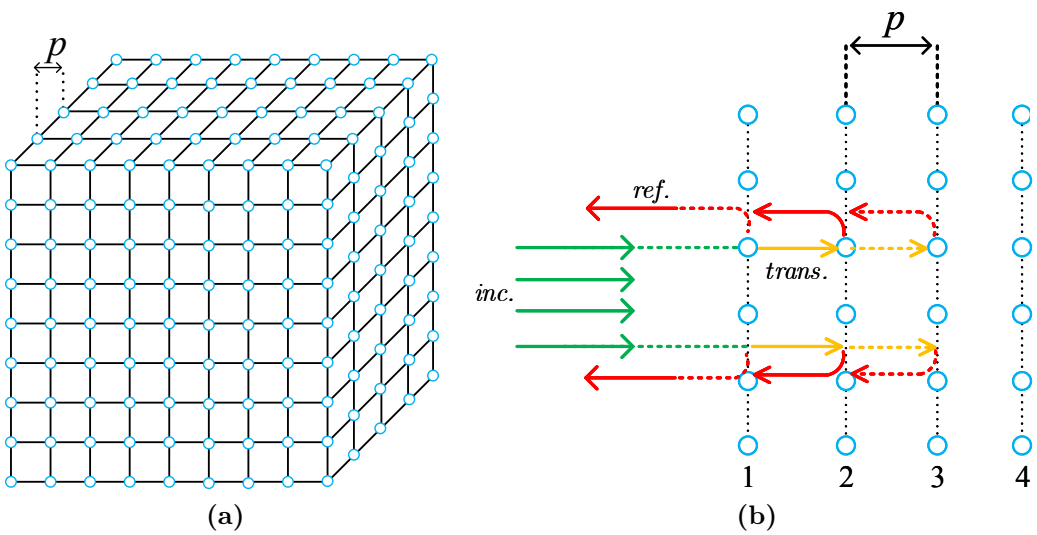

Figure 2.2.2: (a) Cubic lattice with spacing between elements equal to p. (b) Normally incident (green color) electromagnetic wave interaction with the lattice. Reflected and transmitted waves are represented by red and yellow colors, respectively.

2.2.1 Wave and material interaction

In order to understand the electromagnetic wave interaction with artificial materials or metamaterials it is important to understand the interaction of the electromagnetic wave with natural materials. Natural materials are made of tiny elements, i.e., atoms and/or molecules. There are two types of natural materials commonly known *amorphous materials* and *crystalline materials*. Materials in which the elements are randomly arranged with no fixed shape are called *amorphous materials*. Materials in which the elements are periodically arranged in a regular pattern are called *crystalline materials*. The important parameters are distance or spacing between elements, which is denoted by p and the free-space wavelength $\lambda_\circ$. The factor $p/\lambda_\circ$ will determine the type of interaction between waves and materials. For example, consider a cubic lattice where elements are arranged in a periodic pattern as shown in Fig. 2.2.2(a). The cubic lattice is examined for two cases: when the wavelength of the incident wave is much larger than p or comparable to p.

Fig. 2.2.2(b) illustrates the reflection and the transmission of a normally incident wave on the lattice. If the wavelength is comparable with p, the wave will then propagate from column 1 to column 2 covering a path p. At column 2, the wave will be partly reflected and partly transmitted towards column 3. The reflected wave from column 2, while propagating towards column 1 will cover an additional distance p. All the reflected waves when they arrive at column 1 will have the same phase if the distance p is equal to half a wavelength. Since there are many elements in the crystal, there will

be many reflected waves, which will reinforce each other. These reflections are called *Bragg reflections*. Therefore, the *Bragg effect* occurs when the wavelength is on the order of distance between the elements constituting the lattice (medium). These materials are often referred to as *photonic bandgap materials*.

On the other hand, when the element spacing (period) is much smaller than to the wavelength, there are no significant reflection or diffraction phenomena (electromagnetic wave does certainly get affected when propagating through the material). The medium appears to be homogeneous and continuous for the incident wave. The relevant material properties in such a scenario are conductivity and the dielectric constant. These materials are often categorized under *effective medium theory* and are referred to as metamaterials. The electromagnetic behavior of such materials is the result of the effective-medium response.

2.2.2 Classification of materials

The properties of materials can be characterized by the macroscopic parameters electric permittivity (ε) and magnetic permeability (μ). The classification distinguishes the macroscopic properties of each type of material, which is useful in describing the performance of wave-matter interactions. The electric permittivity of a material is defined as the ability of the material to store electrical energy when an electric field is applied. Similarly, the magnetic permeability of the material is its ability to get magnetized in response to an applied magnetic field. The permittivity and the permeability of free space or air are denoted by $\varepsilon_\circ$ and $\mu_\circ$, respectively, where $\varepsilon_\circ = 8.858 \times 10^{-12}\,\mathrm{F/m}$ and $\mu_\circ = 4\pi \times 10^{-7}\,\mathrm{H/m}$. The permittivity (permeability) of all other materials is determined relative to the free space permittivity (permeability). The relative permittivity (ε_r) and the relative permeability (μ_r) are defined as $\varepsilon_r = \varepsilon/\varepsilon_\circ$ and $\mu_r = \mu/\mu_\circ$, respectively. Moreover, the refractive index of a material is given by $n = \sqrt{\varepsilon_r \mu_r}$. Fig. 2.2.3 illustrates the classification of materials based on the values of their permittivity and permeability. It also shows the behavior of an incident electromagnetic wave on an air-material interface. In the first quadrant lie the materials, which have both quantities positive (ε_r, μ_r) and are called double positive materials. These are mostly naturally occurring materials. The second quadrant represents epsilon negative materials that have positive permeability and negative permittivity. These materials strongly react to electromagnetic fields and may support surface waves, as often observed for optical frequencies (infrared / visible frequency range). The third quadrant denotes double negative materials whose permittivity and permeability are both negative. The distinctive feature of such materials is that the wave propagates in the backward direction but energy is transferred in the forward direction. It is also observed that these materials obey a reverse Snell's law. Therefore, they are known as negative index media (NIM) or

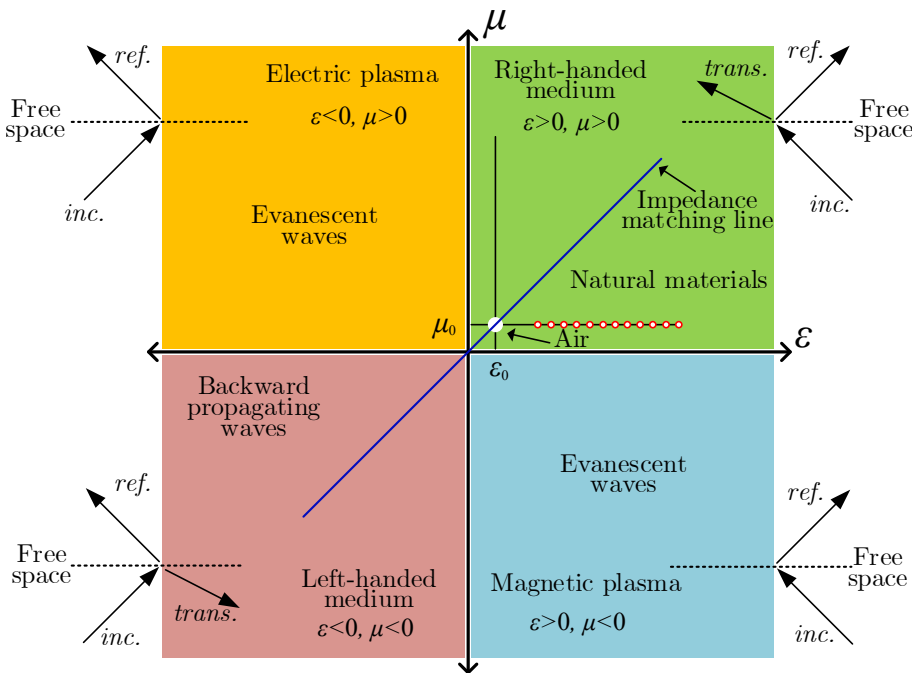

Figure 2.2.3: Classification of materials based on constitutive parameters, permittivity ε and permeability μ. Incident, reflected and transmitted waves are represented by $inc.$, $ref.$, and $trans.$, respectively.

Veselago's material (LH medium). The fourth quadrant denotes materials with negative permeability and positive permittivity. They are also called mu-negative materials. This property is observed in Gyrotropic materials. These materials may also exhibit the effect of Faraday rotation. Most of the natural materials lie on the $\mu = \mu_\circ$ line with $\varepsilon \geq \varepsilon_\circ$.

In Fig. 2.2.3, the diagonal line represents the impedance matching condition with free space. It means that materials that have identical permittivity and permeability ($\varepsilon_r = \mu_r$) result in perfect matching at the material interface for normal incidence (no reflection) because then the intrinsic impedance of the materials is $\eta_z = \sqrt{\frac{\mu}{\varepsilon}} = \sqrt{\frac{\mu_\circ \mu_r}{\varepsilon_\circ \varepsilon_r}} = \sqrt{\frac{\mu_\circ}{\varepsilon_\circ}} = 376.7\,\Omega$, which is the free space impedance. Interestingly when the permittivity and the permeability are simultaneously zero the medium is called nihility, which can yield a perfect tunneling effect.

2.2.3 Modeling and realization of metamaterials

The first metamaterial model was realized using thin metallic conducting wires of specific radius a and conductivity σ arranged periodically with a fixed space p between the elements such that $p \ll \lambda_g$, where λ_g was the wavelength of operation. Therefore, the structure was effectively homogeneous. The structure was inspired by the work of

Pendry [PHSY96]. The structure is also known as artificial electric plasma because of its negative-$\boldsymbol{\varepsilon}$ and it is shown in Fig. 2.2.4(left). When a z-polarized electromagnetic wave (electric field vector $\boldsymbol{E}$ parallel to the z-axis) is incident on the thin-wire (TW) structure, current is induced along the wires resulting in an electric dipole moment. The permittivity of this metamaterial as a function of the electric plasma frequency is given by [CI05]

$$\varepsilon_r(\omega) = 1 - \frac{\omega_{pe}^2}{\omega^2 + \zeta^2} + j\frac{\zeta\ \omega_{pe}^2}{\omega\ (\omega^2 + \zeta^2)}\,, \tag{2.2.1}$$

where the electric plasma frequency is denoted by $\omega_{pe} = \sqrt{2\pi c^2/[p^2 \ln(p/a)]}$ with c denoting the speed of light. Since the metallic wires are associated with metallic losses, eq. (2.2.1) contains the damping factor $\zeta = \varepsilon_\circ(p\omega_{pe}/a)^2/(\pi\sigma)$. Therefore, it can be seen that

$$\mathrm{Re}(\varepsilon_r) < 0, \quad \text{when} \quad \omega^2 < \omega_{pe}^2 - \zeta^2\,, \tag{2.2.2}$$

which can be further simplified if $\zeta = 0$, then

$$\varepsilon_r < 0, \quad \text{for} \quad \omega < \omega_{pe}. \tag{2.2.3}$$

It is assumed that the electrical length of the TWs is much larger than the wavelength. This means that the resonant frequency of the TWs must be larger than the excitation frequencies. Moreover, in the absence of magnetic dipole moments the structure has a permeability $\mu = \mu_\circ$.

Fig. 2.2.4(center) shows the periodic arrangement of the metallic split-ring res-

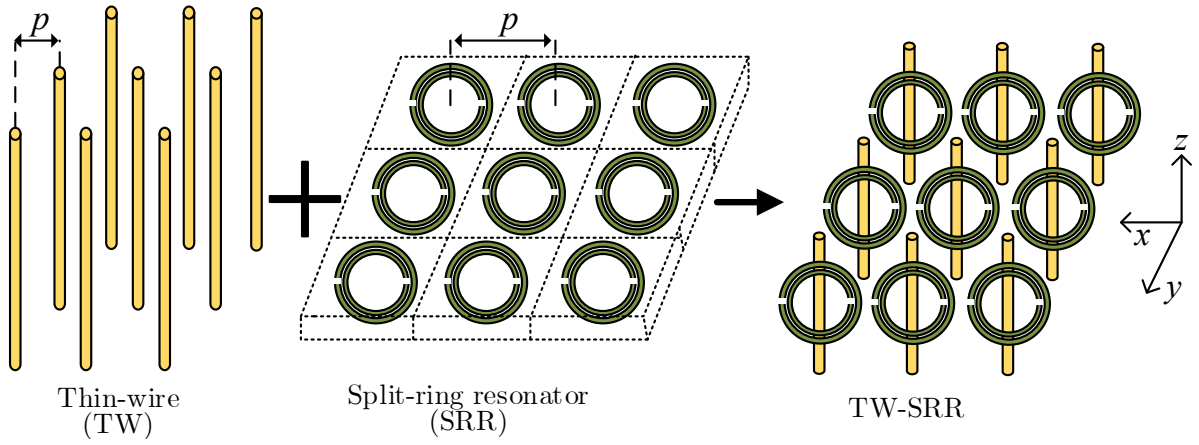

Figure 2.2.4: A combined Thin-wire (TW) and split-ring resonator (SRR) structure was the first material to demonstrate $(-\varepsilon,-\mu)$ properties.

onators (SRRs) that are also known as artificial magnetic plasma. When the magnetic field vector $\boldsymbol{H}$ of the excited electromagnetic wave is perpendicular to the plane of the SRRs ($\boldsymbol{H} \perp y$), the structure resonates and a current is induced in the loop. As a result, an equivalent magnetic dipole moment is generated. The plasmonic-type permeability of the SRR as function of frequency is given as

$$\mu_r(\omega) = 1 - \frac{F\omega^2(\omega^2 - \omega_{0m}^2)}{(\omega^2 - \omega_{0m}^2) + (\omega\zeta)^2} + j\frac{F\omega^2\zeta}{(\omega^2 - \omega_{0m}^2) + (\omega\zeta)^2}\,, \tag{2.2.4}$$

where the magnetic resonance frequency and the damping factor are $\omega_{0m} = c\sqrt{\frac{3p}{\pi \ln(2wa^3/\delta)}}$ and $\zeta = 2pR'/a\mu_\circ$, respectively. The other unknown quantities are

$F = \pi(a/p)^2$,
a: radius of the inner SRR,
w: width of the rings,
δ: radial gap between the rings,
R': metal resistance per unit length.

Eq. (2.2.4) shows that for certain frequency ranges when $\zeta \neq 0$, it is possible to have $\mathrm{Re}(\mu_r) < 0$, but for the loss-less case ($\zeta = 0$), we have

$$\mu_r < 0\,, \quad \text{for} \quad \omega_{0m} < \omega < \omega_{pm}, \tag{2.2.5}$$

where $\omega_{pm} = \frac{\omega_{0m}}{\sqrt{1-F}}$, is the magnetic plasma frequency.

The TWs and the SRRs can be combined together to form a volumetric metamaterial structure as shown in Fig. 2.2.4(right). The unique feature of the composite TW-SRR structure is that it has simultaneous negative permittivity and permeability. This is achieved by operating the TWs and the SRRs in the overlapped frequency ranges where the TWs have negative-ε and the SRRs have negative-μ. The disadvantages of such an assembly are that: 1) it does not account for the coupling between the constituent structures, which can result in totally different properties compared to simple superposition; 2) due to its resonant nature it has narrow bandwidth and exhibits high losses. Thus, bulk composite structures such as TW-SRR metamaterials do not have significant use in engineering applications. Therefore, the transmission-line approach of metamaterials was developed.

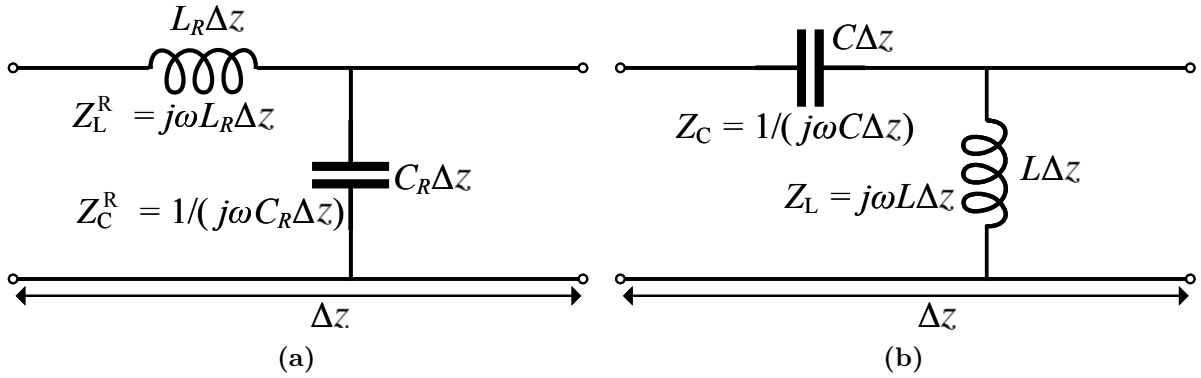

Figure 2.2.5: Incremental transmission line equivalent circuit for (a) RH materials (b) LH metamaterials.

2.2.4 Transmission line metamaterials

Unlike electric circuit analysis where voltage and current do not vary with the physical position of the lumped elements, it is known that on a transmission line voltage and current can vary in magnitude and phase over its length. Thus a transmission line is a distributed parameter network. Fundamentally the transmission line concept for metamaterials is the same as for elementary transmission line theory. In the conventional transmission line model a series inductor and a shunt capacitor constitute the circuit model as shown in Fig. 2.2.5(a). A loss-less, infinitesimal length $\triangle z$ transmission line model is used to represent normal materials (RH materials). The equivalent lumped-element circuit model shown in Fig. 2.2.5(b) is used to represent typical LH materials.

Metmaterials designed using transmission line theory exhibit wide bandwidth and low loss because they operate at non-resonant frequencies. These designs have planar configurations, which allow good matching to the excitation sources and control over a cutoff frequency due to optimized LC parameters. The expressions that define the characteristic of the circuit in Fig. 2.2.5(b) are

$$\gamma = j\beta = \frac{1}{j\omega \triangle z \sqrt{LC}}, \tag{2.2.6}$$

$$\beta = -\frac{1}{\omega \triangle z \sqrt{LC}} < 0, \tag{2.2.7}$$

$$Z_\circ = \sqrt{Z_C Z_L} = \sqrt{\frac{L}{C}} > 0, \tag{2.2.8}$$

$$v_p = \frac{\omega}{\beta} = -\omega^2 \triangle z \sqrt{LC} < 0, \tag{2.2.9}$$

$$v_g = \left(\frac{\partial \beta}{\partial \omega}\right)^{-1} = \omega^2 \triangle z \sqrt{LC} > 0, \tag{2.2.10}$$

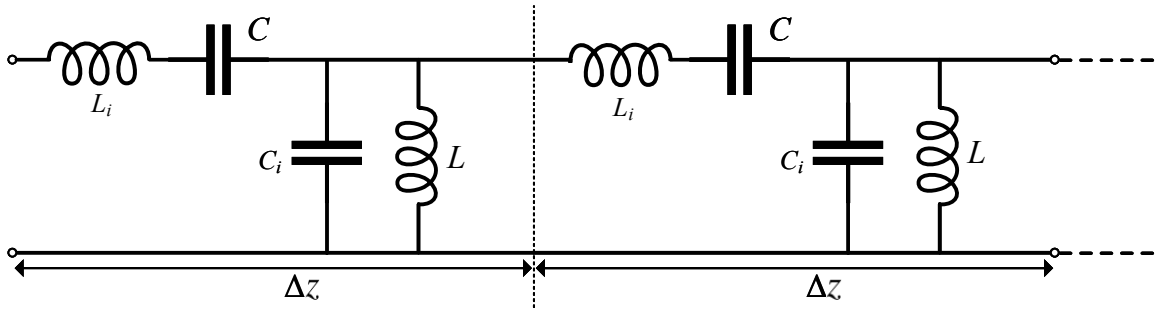

Figure 2.2.6: Cascaded CRLH transmission line equivalent circuit. Each section of length $\triangle z$ represents a unit cell.

where γ, β, $Z_\circ$, v_p and v_g represent the complex propagation constant, the propagation constant, the characteristic impedance, the phase velocity and the group velocity, respectively, of the transmission line metamaterial. The opposite signs of eq. (2.2.9) and eq. (2.2.10) indicate that the phase velocity and the group velocity are antiparallel to each other, which supports the property of backward wave propagation. Since pure left-hand structures do not exist, the circuit in Fig. 2.2.5(b) needs to be modified in order to include the effect of magnetic fluxes induced due to the current flow through C. This can be done by introducing a series inductor L_i. Furthermore, to compensate for the voltage gradient between the ground plane and the conductors, a shunt capacitor C_i is introduced. The modified circuit for LH media that is more practical is shown in Fig. 2.2.6. This type of configuration has been termed as "composite right/left-handed" (CRLH) because the additional effects (L_i, C_i) included in the circuit account for the right-hand response, without which the circuit is not the actual representation of practical LH media [CI05]. It is also important to mention here that the condition of the average cell size to remain much smaller than the wavelength of operation must be obeyed while designing such structures. The transmission line method was used for the first time to realize a microstrip based design in [CI02].

2.2.5 Resonant and non-resonant structures

In the design of metamaterials, the constituent materials have an important role in determining the behavior of the metamaterial structure, more specifically, the elements of the unit cell must be carefully chosen to achieve a desired effective permittivity and permeability. The elements can either be resonant or non-resonant, both have their own advantages and disadvantages. Due to the high quality factor of resonant structures, the frequency response is narrowband and the effective permittivity and permeability around the resonance frequency change very sharply. A little change in the frequency shows large variation in the values of ε and μ. This means that any change in the geometric size of the resonating element will shift the resonance frequency and this in turn will cause changes

in the ε and μ values. The benefit of such a behavior is that large dynamic-range material parameters can be realized. Resonant metamaterials are useful in sensor devices where narrowband selectivity is required. In these narrowband regions, the impedance of the structure is matched to the impedance of the incident medium. Changes in the material parameters cause a shift in the resonance frequency because the surface impedance is a function of frequency, permittivity, and permeability. The shift in the resonance frequency is often exploited in sensing devices. In a resonant structure, the loaded quality factor (Q_l) is related to the transmission loss. Q_l can be obtained from the magnitude of the transmission parameter (S_{21}) as [CI05]

$$Q_l = \frac{f_r}{B_w}, \tag{2.2.11}$$

where f_r and B_w are the resonance frequency and the $-3\,\mathrm{dB}$ bandwidth, respectively. Q_l will be maximum for narrow-bandwidth and minimum for wide bandwidth. It means that a trade-off between transmission level and bandwidth has to be made. The unloaded quality (Q_u) factor in terms of the stored energy and the power dissipated in a resonator is defined as

$$Q_u = \omega \frac{\text{average energy stored in resonator}}{\text{power dissipated in resonator}}. \tag{2.2.12}$$

In a resonator, the total transmission loss occurs due to the dielectric and Ohmic losses [CI05], and the coupling losses at the input/output transitions with the external circuit. Maximizing Q_l is equivalent to minimizing the transmission loss. According to eq. (2.2.11), Q_l is maximum at the resonance frequency f_r when the resonator in narrowband (very small B_w) because minimum power will be dissipated in the resonator cavity due to extremely narrow bandwidth. Thus, according to eq. (2.2.12), Q_u will also be maximized. As a result, a good transmission characteristics can be achieved. The loaded quality factor, the unloaded quality factor and the external quality factor (Q_e accounts for the coupling losses) are related by the expression

$$\frac{1}{Q_l} = \frac{1}{Q_u} + \frac{1}{Q_e}. \tag{2.2.13}$$

Non-resonant metamaterial elements are deployed in designs, which do not require large dynamic-range material parameters. In non-resonant metamaterials, the effective permittivity and permeability change slowly over a wide band. Non-resonant elements based frequency selective surfaces have only been used to obtain bandpass response. They consist of metallic patches which act as capacitances and wire grids act as inductances for the incident waves. As a result, a first-order band-pass response is achieved for these structures [Beh08]. The fact is that the non-resonant metamaterials do have a resonant

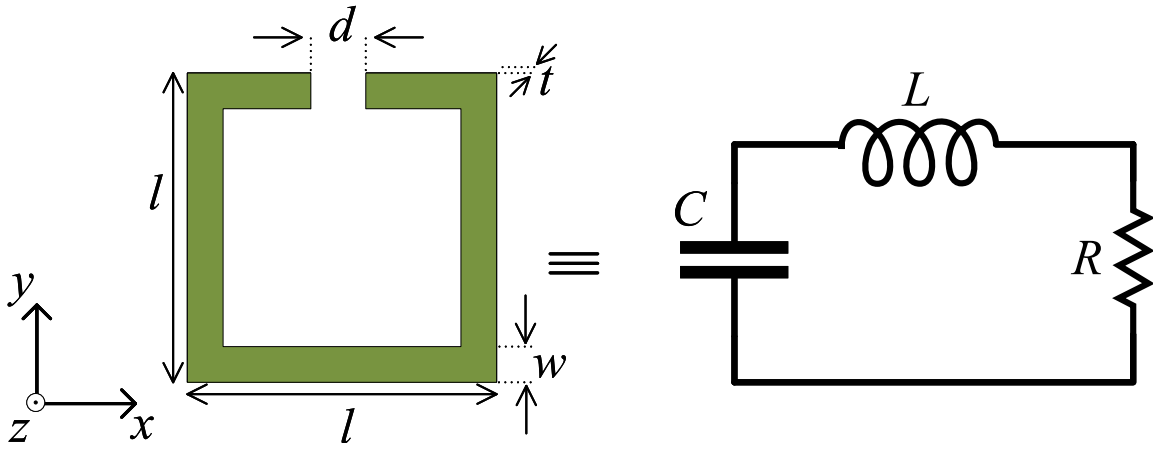

Figure 2.2.7: Planar rectangular split-ring resonator equivalent circuit model.

frequency, but it is much higher than the frequencies a particular structure is designed for. This way non-resonant metamaterials operate at low losses. Generally, dielectric metamaterials can also be categorized as non-resonant, which are quite often used in absorbers.

2.2.6 Electromagnetic response of a Split-Ring Resonator

It is known that a current carrying coil or loop wire produces a magnetic field along its central axis. Similarly, a planar metallic ring placed on a dielectric would have a magnetic response when a current circulates in the ring. A ring can be modelled by an equivalent inductor of inductance L. A small split in the ring will create a capacitive region with capacitance C. This split-ring will behave like an LC oscillating circuit and it will resonate at $f = 1/(2\pi\sqrt{LC})$. In addition, the resonance wavelength will be much larger than its physical dimensions. The equivalent circuit for the rectangular split-ring resonator (RSRR) is shown in Fig. 2.2.7 where R represents the losses. The electromagnetic response of the unit cell RSRR is polarization dependent. When an x-polarized electric field of the incident wave passes through the RSRR of Fig. 2.2.7, it couples with the capacitance of the RSRR and the current circulates in the loop as shown in Fig. 2.2.8(a). In other words, the gap of the RSRR acts as short and a magnetic field is induced due to the circulating currents. This way a magnetic dipole is created and the frequency that results in such a response is called magnetic resonance frequency, which is also known as an LC resonance [LED+04]. Similarly, when a y-polarized wave is incident on the RSRR of Fig. 2.2.7, the electric field vectors can not couple with the capacitance of the RSRR ($\boldsymbol{E_i} \parallel y$) as a result an electric dipole is created at the electric resonance frequency as shown in Fig. 2.2.8(b).

The LC resonance frequency (ω_{LC}) and the LC resonance wavelength (λ_{LC}) for the

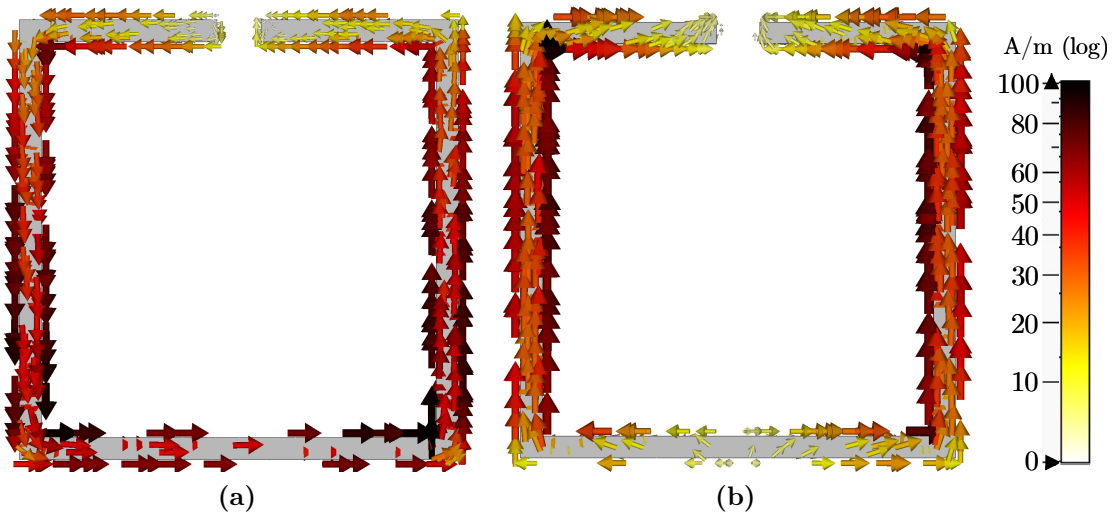

Figure 2.2.8: Electric surface current distribution on planar RSRR for (a) normal transverse magnetic (TM) wave incidence ($\boldsymbol{E_i} \parallel x$) (b) normal transverse electric (TE) wave incidence ($\boldsymbol{E_i} \parallel y$).

RSRR are [LED+06]

$$\omega_{LC} = \frac{1}{\sqrt{LC}} = \frac{1}{l}\frac{c}{\sqrt{\varepsilon_c}}\sqrt{\frac{d}{w}} \propto \frac{1}{\text{size}}, \tag{2.2.14}$$

$$\lambda_{LC} = \frac{2\pi c}{\omega_{LC}} = 2\pi l\sqrt{\varepsilon_c}\sqrt{\frac{w}{d}} \propto \text{size}, \tag{2.2.15}$$

where l, d, and w are length, gap and width as shown in Fig. 2.2.7. c and ε_c are the speed of light and the permittivity of the material between the gap (substrate relative permittivity). From eq. (2.2.14) and eq. (2.2.15), it can be seen that the LC resonance wavelength is directly proportional to the length for fixed w/d as well as the permittivity of the material ε_c. In addition if the gap closes, $C \to \infty$, the resonance wavelength will be infinity. It is clear from these equations that the material and geometric parameters, except the thickness t, influence the resonance frequency.

2.3 Scattering matrix

Metamaterial structures can be represented by equivalent circuit models, which allow to use circuit analysis concepts to solve microwave problems instead of Maxwell's equations. At low frequencies the dimensions of the circuit are very small relative to the wavelength, as a result there is negligible phase change along the circuit between any two

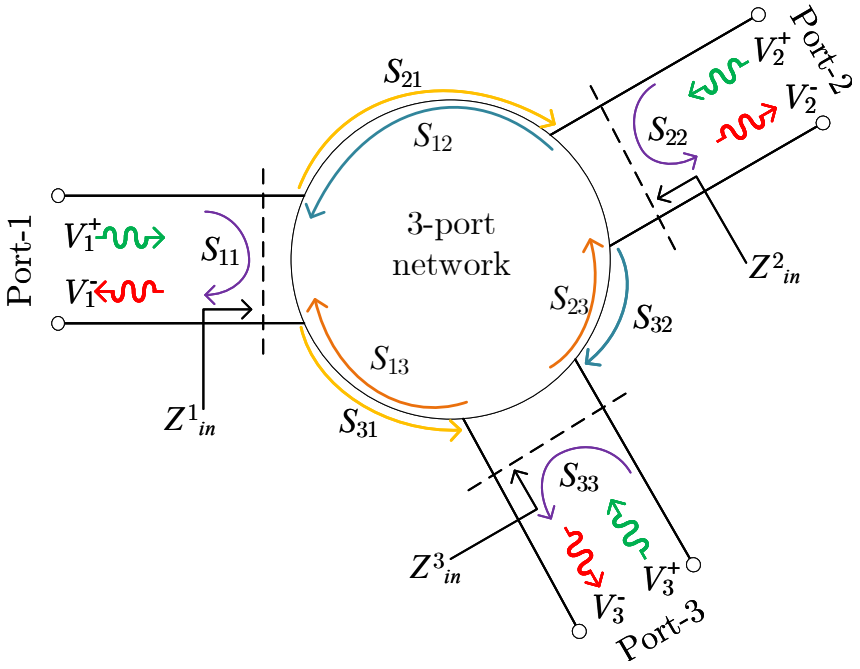

Figure 2.3.1: S-parameters and three port microwave network.

points, but for high frequencies this is not true. At high frequencies voltages and currents along the transmission line may not be the same at different points. Therefore, microwave network analysis is used for the transmission line network, which contains distributed elements. Network analysis is simpler than field analysis using Maxwell's equations and it can be easily modified to combine several distributed elements. However, in some situations, the solution using circuit analysis may be oversimplified, leading to incorrect results. In such situations one must use field analysis using Maxwell's equations (e.g., to find electric or magnetic fields in arbitrary points in space) [Poz11].

The S-parameter analysis provides a complete description of a network and deals with incident, reflected, and transmitted waves more efficiently. The scattering matrix describes relations between the power waves travelling towards the ports (incident) to the power waves travelling away from the ports (reflected) or power waves travelling from one port to the other port. The scattering matrix is constituted by [Poz11]

$$S_{ij} = \left.\frac{V_i^-}{V_j^+}\right|_{V_k^+=0 \text{ for } k\neq j}, \tag{2.3.1}$$

where V_j^+ and V_i^- represent the voltage[2] of the wave incident on a port j and the voltage of the reflected wave from a port i, respectively (subscripts indicate the port number and superscripts indicate the direction of the wave). Furthermore, eq. (2.3.1) also indicates that all ports are commonly matched when S-parameters are determined. A generalized

[2]The voltage description is only used if the same reference impedance is used at all ports.

scattering matrix $[S]$ for an N-port network is

$$\begin{bmatrix} V_1^- \\ V_2^- \\ \vdots \\ V_N^- \end{bmatrix} = \begin{bmatrix} S_{11} & S_{12} & \cdots & S_{1N} \\ S_{21} & S_{22} & \cdots & S_{2N} \\ \vdots & \vdots & \ddots & \vdots \\ S_{N1} & S_{N2} & \cdots & S_{NN} \end{bmatrix} \begin{bmatrix} V_1^+ \\ V_2^+ \\ \vdots \\ V_N^+ \end{bmatrix}. \tag{2.3.2}$$

The reflection coefficient for port i is represented by S_{ii} when all other ports are matched and not excited. Similarly, the transmission coefficient from port j to port i is represented by S_{ij} when all other ports are matched and not excited. A three-port network diagram is shown in Fig. 2.3.1 where reflected waves and transmitted waves can be seen. The dashed line represents the terminal plane which is the reference plane for current and voltage phasors. Z_{in}^i represents the input impedance, seen at port i looking into the network. The input impedance is of the form $Z_{in} = R + jX$, where the real part of the impedance is related to accepted power and the imaginary part of the impedance is related to stored energy in the network. When the network is lossless the real part of the impedance is zero ($R = 0$). All the input power is accepted and the average power dissipated by the network is zero. The imaginary part of the impedance is negative for a capacitive load and positive for an inductive load. Z_{in} is also related to S_{11} by

$$Z_{in}^i = \frac{1 + S_{ii}}{1 - S_{ii}} Z_\circ. \tag{2.3.3}$$

where $Z_\circ$ is the output port impedance (usually $50\,\Omega$).

2.4 Floquet's theorem

Metamaterial structures are usually arranged periodically to achieve desired electromagnetic properties. Therefore, the Floquet theorem can be applied to simplify and understand the wave propagation in periodic structures. It states that a field solution can be form as a product of a non-periodic propagation factor and a periodic function, i.e.,

$$\begin{Bmatrix} \boldsymbol{E}(z) \\ \boldsymbol{H}(z) \end{Bmatrix} = \begin{Bmatrix} \boldsymbol{E}_p(z) \\ \boldsymbol{H}_p(z) \end{Bmatrix} e^{-\gamma z}, \qquad \begin{Bmatrix} \boldsymbol{E}_p(z) \\ \boldsymbol{H}_p(z) \end{Bmatrix} = \begin{Bmatrix} \boldsymbol{E}_p(z + op_z) \\ \boldsymbol{H}_p(z + op_z) \end{Bmatrix}. \tag{2.4.1}$$

Eq. (2.4.1) represents the fields in a periodic structure arranged periodically in the direction of propagation along the z-axis with complex propagation constant γ and periodicity p_z. Therefore, fields at point $z + op_z$ (o is an integer number) can be computed from fields at z by taking the product with the attenuation factor and considering the appropriate phase shift. The complex propagation constant can be written as

$$\gamma = \alpha + j\beta, \tag{2.4.2}$$

where α and β are the attenuation constant and the phase constant (also known as wave number), respectively. If the structure has periodicity in multiple dimensions, e.g., two or three, such as in metasurfaces, then finding a solution for the unit cell will be sufficient to derive the solution at any location in the periodic array. In the more general form the scalar wave number β will be replaced by a wave number vector quantity $\boldsymbol{\beta}$. The unit cell geometry will be represented by a spatial vector $\boldsymbol{r_p}$, and the field solution is, thus, represented as

$$\begin{Bmatrix} \boldsymbol{E}(\boldsymbol{r}) \\ \boldsymbol{H}(\boldsymbol{r}) \end{Bmatrix} = \begin{Bmatrix} \boldsymbol{E}_p(\boldsymbol{r}) \\ \boldsymbol{H}_p(\boldsymbol{r}) \end{Bmatrix} e^{-j\boldsymbol{\beta}\cdot\boldsymbol{r}}, \qquad \begin{Bmatrix} \boldsymbol{E}_p(\boldsymbol{r}) \\ \boldsymbol{H}_p(\boldsymbol{r}) \end{Bmatrix} = \begin{Bmatrix} \boldsymbol{E}_p(\boldsymbol{r}+\boldsymbol{r_p}) \\ \boldsymbol{H}_p(\boldsymbol{r}+\boldsymbol{r_p}) \end{Bmatrix}, \tag{2.4.3}$$

where $\boldsymbol{r_p} = mp_x\hat{x} + np_y\hat{y} + op_z\hat{z}$ (m, n, and o are integer numbers and p_x, p_y, and p_z are unit cell lengths in x-, y-, and z- direction, respectively), and $\boldsymbol{r} = x\hat{x} + y\hat{y} + z\hat{z}$. The wave number vector in three dimensions is represented as $\boldsymbol{\beta} = \beta_x\hat{x} + \beta_y\hat{y} + \beta_z\hat{z}$.

2.5 Maxwell's equations and constitutive relations

The analysis of electromagnetic waves on a macroscopic level is governed by Maxwell's equations. Electric and magnetic phenomena are described by a set of differential equations as given by

$$\nabla \times \boldsymbol{E} = -\frac{\partial \boldsymbol{B}}{\partial t} - \boldsymbol{M}, \tag{2.5.1a}$$

$$\nabla \times \boldsymbol{H} = \frac{\partial \boldsymbol{D}}{\partial t} + \boldsymbol{J}, \tag{2.5.1b}$$

$$\nabla \cdot \boldsymbol{D} = \rho, \tag{2.5.1c}$$

$$\nabla \cdot \boldsymbol{B} = \varrho_m, \tag{2.5.1d}$$

where $\boldsymbol{E}$, $\boldsymbol{B}$, $\boldsymbol{H}$, and $\boldsymbol{D}$ are the electromagnetic field vectors, which are used to represent electric field (V/m), magnetic flux density (Wb/m^2), magnetic field (A/m), and electric flux density (C/m^2), respectively. $\boldsymbol{M}$ is a magnetic source vector representing the magnetic current density (V/m^2), $\boldsymbol{J}$ is an electric current source vector representing an electric current density (A/m^2), ρ is the electric charge density (C/m^3), and ϱ_m is the magnetic charge density (Wb/m^3), where $\boldsymbol{M}$ is in general an equivalent quantity since magnetic sources do not exist in nature.

In a linear (permittivity and permeability not depending on $\boldsymbol{E}$ or $\boldsymbol{H}$), source free

($\boldsymbol{M} = 0$, $\boldsymbol{J} = 0$), non-dispersive (permittivity $\boldsymbol{\varepsilon}$ and permeability $\boldsymbol{\mu}$ not depending on angular frequency $\boldsymbol{\omega}$), isotropic ($\boldsymbol{\varepsilon}$ and $\boldsymbol{\mu}$ are not function of direction of the applied field), homogenous medium ($\boldsymbol{\varepsilon}$ and $\boldsymbol{\mu}$ are not function of position, meaning they are uniform throughout the medium), eq. (2.5.1), after substituting the flux densities $\boldsymbol{B}$ and $\boldsymbol{D}$ from eq. (2.5.3), can be written in phasor form as

$$\nabla \times \boldsymbol{E} = -j\omega\mu\boldsymbol{H}, \tag{2.5.2a}$$
$$\nabla \times \boldsymbol{H} = j\omega\varepsilon\boldsymbol{E}, \tag{2.5.2b}$$
$$\nabla \cdot \boldsymbol{D} = 0, \tag{2.5.2c}$$
$$\nabla \cdot \boldsymbol{B} = 0. \tag{2.5.2d}$$

In eq. (2.5.2) the time-dependence $e^{j\omega t}$ is considered and suppressed throughout the thesis. The four electromagnetic field vectors are linearly related to each other as

$$\boldsymbol{D} = \varepsilon\boldsymbol{E}, \tag{2.5.3a}$$
$$\boldsymbol{B} = \mu\boldsymbol{H}. \tag{2.5.3b}$$

Eqs. (2.5.3) are also known as the constitutive relations and ($\boldsymbol{\varepsilon}$,$\boldsymbol{\mu}$) are known as the consitutive parameters. In free space, $\boldsymbol{\varepsilon} = \boldsymbol{\varepsilon}_\circ$ and $\boldsymbol{\mu} = \boldsymbol{\mu}_\circ$. In order to find a solution for $\boldsymbol{E}$, the curl of eq. (2.5.2a) is taken to give

$$\nabla \times (\nabla \times \boldsymbol{E}) = -j\omega\mu(\nabla \times \boldsymbol{H}), \tag{2.5.4}$$

using eq. (2.5.2b) in eq. (2.5.2a) gives

$$\nabla \times (\nabla \times \boldsymbol{E}) = \omega^2\mu\varepsilon\boldsymbol{E}, \tag{2.5.5}$$

where eq. (2.5.5) now has only the single unknown $\boldsymbol{E}$. Moreover, to simplify the left hand side of eq. (2.5.5), a vector identity is used, that is, $\nabla \times \nabla \times \boldsymbol{A} = \nabla(\nabla \cdot \boldsymbol{A}) - \nabla^2\boldsymbol{A}$. Since $\nabla \cdot \boldsymbol{E} = 0$ in a source free medium, then

$$\nabla^2\boldsymbol{E} + \omega^2\mu\varepsilon\boldsymbol{E} = 0, \tag{2.5.6}$$

which is known as *Helmholtz equation* for $\boldsymbol{E}$. Here it must be noted that the divergence condition for $\boldsymbol{E}$ must be explicitly enforced during the solution of the Helmholtz equation. The propagation constant for a lossless medium is defined as $\beta = \omega\sqrt{\varepsilon\mu}$ (previously discussed as phase constant and wave number) and has the unit 1/m. Using β in eq. (2.5.6) further simplifies it to

$$\nabla^2\boldsymbol{E} + \beta^2\boldsymbol{E} = 0. \tag{2.5.7}$$

Following a similar procedure, a Helmholtz equation for $\boldsymbol{H}$ can be derived as

$$\nabla^2\boldsymbol{H} + \beta^2\boldsymbol{H} = 0. \tag{2.5.8}$$

Eq. (2.5.7) and eq. (2.5.8) are eigenvalue equations and one of their solutions is a plane wave of the form

$$\boldsymbol{E} = \boldsymbol{E}_\circ e^{-j\boldsymbol{\beta}\cdot\boldsymbol{r}}, \tag{2.5.9a}$$
$$\boldsymbol{H} = \boldsymbol{H}_\circ e^{-j\boldsymbol{\beta}\cdot\boldsymbol{r}}, \tag{2.5.9b}$$

where $\boldsymbol{r}$ is the position vector (x,y,z) in meters and $\boldsymbol{E}_\circ = A\hat{x} + B\hat{y} + C\hat{z}$ is the amplitude vector of the plane wave in a Cartesian coordinate system. The relation between electric field vector, propagation constant, and magnetic field vector can be derived by substituting eq. (2.5.9a) in eq. (2.5.2a) as

$$\boldsymbol{H} = \frac{j}{\omega\mu}\nabla \times (\boldsymbol{E}_\circ e^{-j\boldsymbol{\beta}\cdot\boldsymbol{r}}), \tag{2.5.10}$$

using the vector identity $\nabla \times (f\boldsymbol{A}) = (\nabla f) \times \boldsymbol{A} + f(\nabla \times \boldsymbol{A})$ and with $(\nabla \times \boldsymbol{E}_\circ) = 0$ gives

$$\boldsymbol{H} = \frac{-j}{\omega\mu}\boldsymbol{E}_\circ \times \nabla e^{-j\boldsymbol{\beta}\cdot\boldsymbol{r}}, \tag{2.5.11}$$
$$= \frac{-j}{\omega\mu}\boldsymbol{E}_\circ \times (-j\boldsymbol{\beta}) e^{-j\boldsymbol{\beta}\cdot\boldsymbol{r}}, \tag{2.5.12}$$

$$\omega\mu\boldsymbol{H} = \boldsymbol{\beta} \times (\boldsymbol{E}_\circ e^{-j\boldsymbol{\beta}\cdot\boldsymbol{r}}), \tag{2.5.13}$$

$$\boldsymbol{\beta} \times \boldsymbol{E} = \omega\mu\boldsymbol{H}, \tag{2.5.14}$$

similarly substituting eq. (2.5.9b) in eq. (2.5.2b) gives

$$\boldsymbol{\beta} \times \boldsymbol{H} = -\omega\varepsilon\boldsymbol{E}. \tag{2.5.15}$$

Eq. (2.5.14) and eq. (2.5.15) make a right handed triad and represent a RH medium ($\varepsilon, \mu > 0$) as shown in Fig. 2.5.1(a). In case of an LH medium ($\varepsilon, \mu < 0$), a left handed triad is built, hence the modified equations are [CI05]

$$\boldsymbol{\beta} \times \boldsymbol{E} = -\omega|\mu|\boldsymbol{H}, \tag{2.5.16}$$

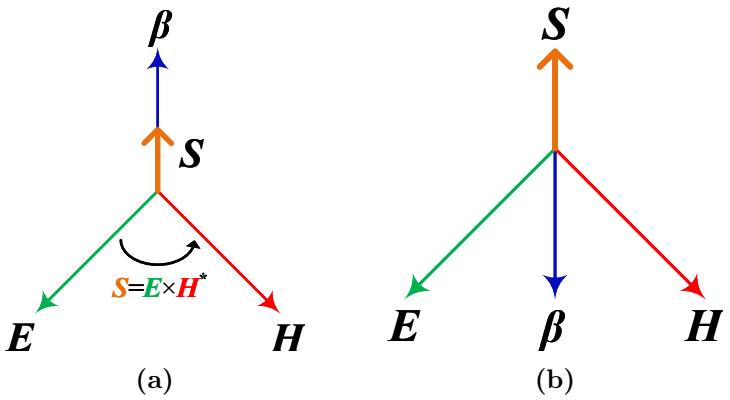

Figure 2.5.1: Electric field vector ($\boldsymbol{E}$) - magnetic field vector ($\boldsymbol{H}$) - wave vector ($\boldsymbol{\beta}$) triad along with Poynting vector ($\boldsymbol{S}$) displayed for (a) Normal materials (right hand materials) with $\varepsilon, \mu > 0$ and (b) LH materials (or negative index materials) with $\varepsilon, \mu < 0$.

$$\boldsymbol{\beta} \times \boldsymbol{H} = \omega |\varepsilon| \boldsymbol{E}. \tag{2.5.17}$$

Eq. (2.5.14) implies that the plane of the magnetic field vector is normal to the vector pointing into the direction of propagation, the magnetic field vector is perpendicular to the electric field vector, and the direction of power flow and the direction of propagation are the same ($\boldsymbol{S} \parallel \boldsymbol{\beta}$), as shown in Fig. 2.5.1(a). The formation of a right-hand triad indicates that the medium has a phase velocity $v_p = \omega/\beta$ and a group velocity in the same direction, which is the characteristic of normal materials. On the contrary, Fig. 2.5.1(b) shows the characteristics of LH materials. Since, for LH materials, ε and μ are negative, which makes $\boldsymbol{\beta}$ negative. Resultantly, the phase velocity becomes negative and anti-parallel to the group velocity, the latter is associated with the direction of power flow. This is the reason that such materials support backward-wave propagation. The Poynting vector ($\boldsymbol{S}$) represents the direction of power flow (energy flux) of an electromagnetic field and is given by

$$\boldsymbol{S} = \frac{1}{2} \boldsymbol{E} \times \boldsymbol{H}^*. \tag{2.5.18}$$

It has the units of power density ($\mathrm{W/m^2}$). Fig. 2.5.1 shows that in both materials the Poynting vector is directed into the forward direction.

Bi-isotropic media

Materials that have the ability to rotate the polarization of an incident electromagnetic wave due to *optical activity* phenomena are called bi-isotropic materials. The measure of this optical activity is known as *chirality*. Chirality is a twisting effect caused

Table 2.5.1: Classification of bi-isotropic media

Medium	Non-chiral ($\kappa = 0$)	Chiral ($\kappa \neq 0$)
reciprocal ($\chi = 0$)	simple isotropic medium	Pasteur medium
non-reciprocal ($\chi \neq 0$)	Tellegen medium	general bi-isotropic medium

when a polarized wave passes through the medium. This happens due to different orientations of the crystals, e.g., right-hand and/or left-hand[3], within a material. The phenomenon of chirality is different from *magnetic optical activity*, which is caused by an external magnetic field, and is the basis for *Faraday rotation*. Materials with an equal amount of right- and left-handed elements do not display polarization rotation and are called *recemic* materials. An element is called *chiral* if it is non-superposable on its mirror image, i.e., Archimedes spiral or 3D helix. The simplest example of a chiral geometry are the human hands, a right hand with palm facing upward when placed on the left hand with palm facing upward do not overlap on each other completely. Therefore, it is a geometric property that leads to the rotation of the plane of polarization of the incident wave. Some naturally occurring molecules with such a geometry are amino acids and sugars etc. The mirror images are usually known as enantiomers. The concept of chiral geometry can be applied to design a unit cell structure that is not symmetric to achieve desirable electromagnetic properties, e.g., polarization rotation (explained in Chapter 5).

The constitutive relations of bi-isotropic materials contain additional material parameters, which gives additional freedom in designing microwave structures and devices. In a bi-isotropic medium, frequency domain constitutive relations are of the form

$$\boldsymbol{D} = \varepsilon \boldsymbol{E} + (\chi - j\kappa)\sqrt{\mu_\circ \varepsilon_\circ}\boldsymbol{H}, \tag{2.5.19}$$

$$\boldsymbol{B} = \mu \boldsymbol{H} + (\chi + j\kappa)\sqrt{\mu_\circ \varepsilon_\circ}\boldsymbol{E}, \tag{2.5.20}$$

where the additional parameters are κ, which is the chirality parameter and measures the handedness of the material, and χ, which represents the magnetoelectric effect (not within the scope of discussion). Both the material parameters are dimensionless when the free-space constant ($\sqrt{\mu_\circ \varepsilon_\circ}$) is separated as represented in eq. (2.5.19) and eq. (2.5.20). Bi-isotropic media can be classified based on the values of κ and χ as shown in Table 2.5.1 [LSTV94].

The first two Maxwell's equations for a source free medium take the form, after

[3]The right-hand and the left-hand elements may not be confused with the right-hand materials and the left-hand materials discussed in the previous sections. Due to the geometric orientation of the elements, right-hand elements produce right elliptical polarized waves and left-hand elements produce left elliptical polarized waves.

substituting eq. (2.5.19) and eq. (2.5.20),

$$\nabla \times \boldsymbol{E} = -j\omega\mu\boldsymbol{H} - j\omega(\chi - j\kappa)\sqrt{\varepsilon_\circ\mu_\circ}\boldsymbol{E}, \tag{2.5.21}$$
$$\nabla \times \boldsymbol{H} = j\omega\varepsilon\boldsymbol{E} + j\omega(\chi + j\kappa)\sqrt{\varepsilon_\circ\mu_\circ}\boldsymbol{H}. \tag{2.5.22}$$

The total electric field and the total magnetic field in a medium are a combination of the fields as shown in Fig. 2.5.2 and can be mathematically written as

$$\boldsymbol{E} = \boldsymbol{E}^+ + \boldsymbol{E}^- \tag{2.5.23}$$
$$\boldsymbol{H} = \boldsymbol{H}^+ + \boldsymbol{H}^- \tag{2.5.24}$$

where $\boldsymbol{E}^+$, $\boldsymbol{E}^-$, $\boldsymbol{H}^+$, $\boldsymbol{H}^-$ are the field quantities, which represent the clockwise rotating fields (with superscript +) and the anticlockwise rotating fields (with superscript −) that are produced because of the presence of different types of elements in a medium. Interestingly, in a homogenous bi-isotropic medium the two fields ($\boldsymbol{E}^+$,$\boldsymbol{H}^+$) and ($\boldsymbol{E}^-$,$\boldsymbol{H}^-$) do not couple and are totally independent. Moreover, for each field the medium behaves as an equivalent isotropic medium with respective material parameters (μ^+, ε^+) and (μ^-, ε^-). The general independent plane waves can be written as [LSTV94]

$$\boldsymbol{E}^+(\boldsymbol{r}) = \boldsymbol{E}_\circ^+ e^{-j\boldsymbol{\beta}^+\cdot\boldsymbol{r}}, \tag{2.5.25a}$$
$$\boldsymbol{E}^-(\boldsymbol{r}) = \boldsymbol{E}_\circ^- e^{-j\boldsymbol{\beta}^-\cdot\boldsymbol{r}}, \tag{2.5.25b}$$
$$\boldsymbol{H}^+(\boldsymbol{r}) = \boldsymbol{H}_\circ^+ e^{-j\boldsymbol{\beta}^+\cdot\boldsymbol{r}}, \tag{2.5.25c}$$
$$\boldsymbol{H}^-(\boldsymbol{r}) = \boldsymbol{H}_\circ^- e^{-j\boldsymbol{\beta}^-\cdot\boldsymbol{r}}. \tag{2.5.25d}$$

The wave vectors for the field components can be defined by assuming that the real unit vector $\hat{\boldsymbol{u}}$ represents the propagation direction for both components then

$$\boldsymbol{\beta}^+ = \hat{u}\beta^+, \qquad \beta^+ = \omega\sqrt{\mu^+\varepsilon^+} = \beta_\circ n^+, \tag{2.5.26a}$$
$$\boldsymbol{\beta}^- = \hat{u}\beta^-, \qquad \beta^- = \omega\sqrt{\mu^-\varepsilon^-} = \beta_\circ n^-, \tag{2.5.26b}$$

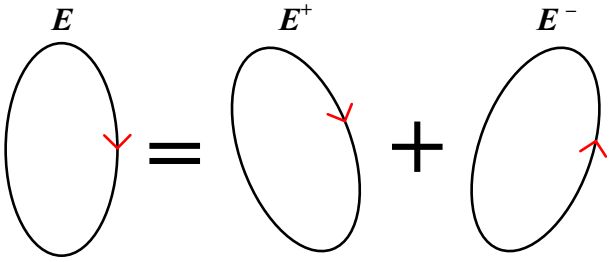

Figure 2.5.2: Electric field vector as a sum of right-hand electric field vector and left-hand electric field vector in a bi-isotropic medium.

$$n_{\pm} = \sqrt{\mu_r \varepsilon_r}\cos\theta \pm \kappa = n(\cos\theta \pm \kappa_r), \tag{2.5.27}$$

where $\beta_\circ = \omega\sqrt{\mu_\circ \varepsilon_\circ}$,$\kappa_r = \kappa/\sqrt{\mu_r \varepsilon_r}$, and $n = \sqrt{\mu_r \varepsilon_r}$ (see Appendix A.1 for μ^+, μ^-, ε^+, and ε^-). Since the plane wave equations are defined, these equations can be used to see how a plane wave propagates in a bi-isotropic medium. Consider a linearly polarized electric field propagating in z-direction having amplitude $\boldsymbol{E}_\circ$ along $\hat{x}$ that can be decomposed into right circularly polarized and left circularly polarized fields as

$$\boldsymbol{E}(z) = \boldsymbol{E}_\circ \hat{x}, \tag{2.5.28}$$

$$\boldsymbol{E}(z) = \boldsymbol{E}_\circ[\frac{1}{2}(\hat{x} - j\hat{y}) + \frac{1}{2}(\hat{x} + j\hat{y})], \tag{2.5.29}$$

$$\boldsymbol{E}(z) = \underbrace{\frac{E_\circ e^{-j\beta^+ z}}{2}(\hat{x} - j\hat{y})}_{\boldsymbol{E}^+} + \underbrace{\frac{E_\circ e^{-j\beta^- z}}{2}(\hat{x} + j\hat{y})}_{\boldsymbol{E}^-}, \tag{2.5.30}$$

substituting eq. (2.5.27) in eq. (2.5.26) and using it in eq. (2.5.30) gives

$$\boldsymbol{E}(z) = \frac{E_\circ e^{-j(\beta\cos\theta+\beta_\circ\kappa)z}}{2}(\hat{x} - j\hat{y}) + \frac{E_\circ e^{-j(\beta\cos\theta-\beta_\circ\kappa)z}}{2}(\hat{x} + j\hat{y}), \tag{2.5.31}$$

$$\boldsymbol{E}(z) = \hat{x}E_\circ e^{-j\beta z\cos\theta}\frac{\left(e^{-j\beta z\kappa_r} + e^{j\beta z\kappa_r}\right)}{2} - j\hat{y}E_\circ e^{-j\beta z\cos\theta}\frac{\left(e^{-j\beta z\kappa_r} - e^{j\beta z\kappa_r}\right)}{2} \tag{2.5.32}$$

$$\boldsymbol{E}(z) = E_\circ e^{-j\beta z\cos\theta}[\hat{x}\cos(\beta z\kappa_r) - j\hat{y}\sin(\beta z\kappa_r)]. \tag{2.5.33}$$

Using Euler's identity (see Appendix A.2) eq. (2.5.32) is simplified to get eq. (2.5.33). In eq. (2.5.33), the term in square brackets is a vector and it indicates that the wave has been rotated by an angle $\phi = \beta z\kappa_r = \beta_\circ z\kappa$ from position $\hat{x}$ in the right-hand direction with thumb pointing in the direction of propagation. Thus it is to be noted that the chirality of the medium only affects the polarization of the field propagating through that medium and doesn't affects its phase.

2.6 Metamaterial inspired frequency selective surfaces

Frequency selective surfaces (FSSs) are spatial filters, which are used to realize bandpass, bandstop, and absorption behavior in response to an incident electromagnetic wave. FSSs are formed by arranging metallic elements, such as patches, slots, wire grids, and resonators etc., periodically on a dielectric substrate. When an electromagnetic wave

is incident on a surface having resonant elements, it causes strong electric fields in the gaps and strong magnetic fields around the electric currents in metallic strips. In addition, there exists coupling between the resonant elements as well. These two types of interactions are responsible for the overall behavior of the FSS. Therefore, the two controlling factors are unit cell element geometry and spacing between the elements. The major challenge in FSS design is the incident angle stability and polarization angle stability. This is due to the reason that if an FSS has to be placed near an antenna it will be illuminated with different angles in a very small area, and grating lobes will occur due to diffraction phenomena unless a mitigation technique is applied. Moreover, realization of a large FSS is not possible where a uniform phase front is required. The solution to these challenges is to have unit cells, which are small relative to the free space wavelength, and compact so they can be tightly packed. This approach of developing FSSs is inspired by metamaterials. Some of the element designs for FSSs are presented in Fig. 2.6.1.

2.7 Applications of metamaterials

The unusual characteristics of metamaterials have led to simple, compact, and aesthetic designs for numerous applications, for example, filters, sensors, imaging, phase shifters, polarization rotators and converters, frequency selective surfaces, and lenses etc. The dynamic range of material parameters, high quality factor, as well as dependence of surface impedance, reflection and transmission coefficients, and refractive index on constitutive parameters allow us to design structures with unique properties.

2.7.1 Metamaterial absorbers

Metamaterial based microwave absorbers are materials used to attenuate electromagnetic wave energy. The different types of absorbers include ferrite tiles, carbon nanotubes, resonant absorbers, and pyramidal absorbers, etc. [BCL+11, NS71]. Absorbers can be used to reduce or eliminate reflections, which can otherwise cause interference in system operation. Resonant absorbers have the advantage of being nonfragile and nonbulky but they are usually narrow-band and have a limited bandwidth. The absorption bandwidth in planar resonance based designs can be increased by using stacked structures with multiple layers of resistive sheets having the same resistivity, or decrease in resistivity from the incident interface till the end like in Jaumann absorbers [KXXP11]. In another approach, a multilayered structure is designed such that each layer has its own resonance frequency. These layers behave like an anti-reflection surface at the resonance frequency. The layers are combined together such that the successive layers have adjacent resonance peaks. Consequently, a collective broadband absorption pattern is achieved, as discussed

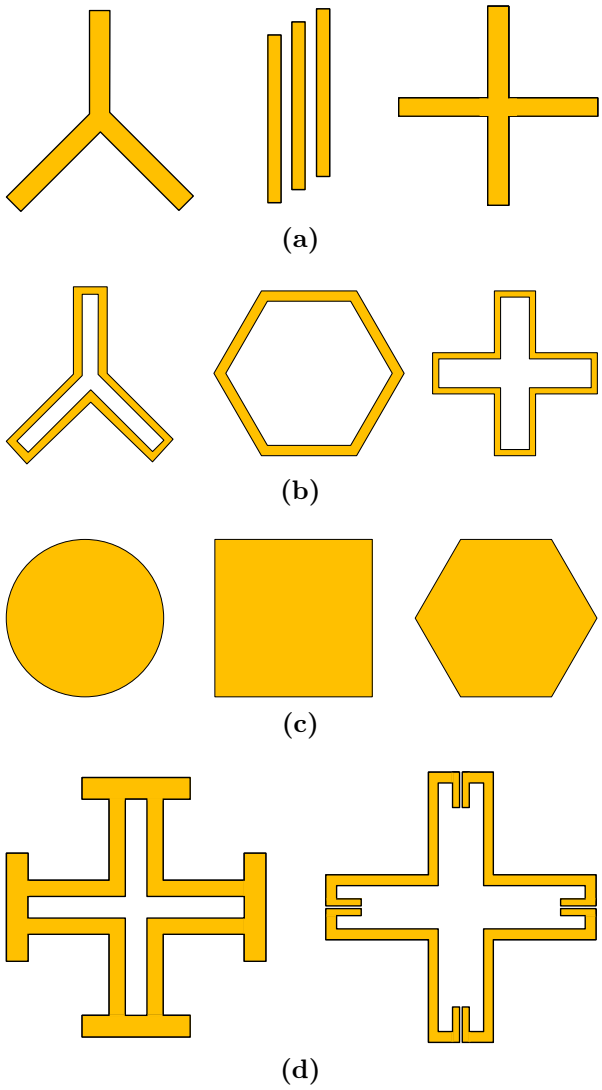

Figure 2.6.1: Typical unit cell elements of four types [Mun05]. (a) Center connected elements (b) Loop type elements (c) Solid interior or plate type elements (d) Combinations.

in [XHLZ13]. A single-layer planar design using hexagonal metal dendritic units having different sizes are arranged in a way that the neighbouring resonant frequencies of different units converge to yield broadband absorption characteristics, as presented in [GSZ13]. In case of non-resonant designs, the impedance gradient technique is used. In the impedance gradient technique the impedance is gradually reduced with respect to the previous layer with no abrupt change to avoid reflections until the wave is completely attenuated within the structure [CZP+11]. This is achieved either by geometric design such as pyramid shape absorbers or by parameter gradients which may be planar sheets with continuously varying material parameters. Tunable absorber designs have also been reported which use lossy elements such as varactor diodes.

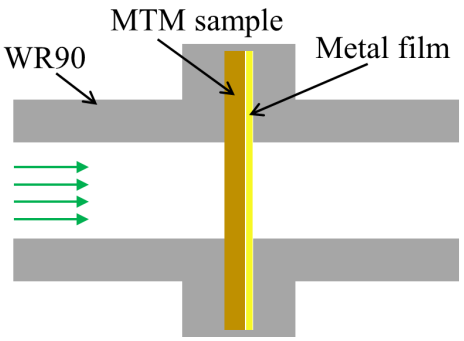

Figure 2.7.1: Metamaterial (MTM) based microwave absorber measurement setup for X-band.

A perfect metamaterial absorber was presented by Landy et al. in 2008 [LSM+08]. It discusses how electric and magnetic resonances can be manipulated to absorb the incident electromagnetic field. Metamaterials allow to produce structures with identical permittivity and permeability that can be easily impedance-matched to free space to decrease the reflection coefficient. In 2010, Cheng et al. experimentally demonstrated an omnidirectional electromagnetic absorber which was theoretically and numerically proposed in 2009 [CCJC10]. Another theoretical interpretation of the metamaterial absorber based on an interference mechanism was presented by Chen [Che12]. Later, a number of tunable designs and applications of metamaterial absorbers were discussed [ZCC+13, KLL16]. One interesting use of metamaterial absorbers is in sensing technologies. Since, the principle of free-space impedance matching is used, any change of the impedance would directly affect the resonance frequency. Therefore, the sensitivity to changes of the dielectric constant or the impedance can be exploited in sensing devices.

Fig. 2.7.1 shows a typical hollow waveguide setup loaded with a metamaterial absorber that is backed by a metal film. Incident electromagnetic waves are absorbed completely at the resonance frequency. Chapter 4 discusses the design and behavior of such an absorber in detail.

2.7.2 Metamaterial filters

Combining the miniaturization technology and passive filtering advantages, metamaterial based microwave filters have been extensively used for filter applications. When an electromagnetic wave interacts with an object, the scattered waves can be used to provide valuable information such as moisture level, geometry of the object and material characterization [Pet11]. Metamaterial based waveguide filter designs can be used to detect cracks on metallic surfaces. Generally the metal fatigue appears on the surface first and detection of these defects is an important task in industry (metal bridges and

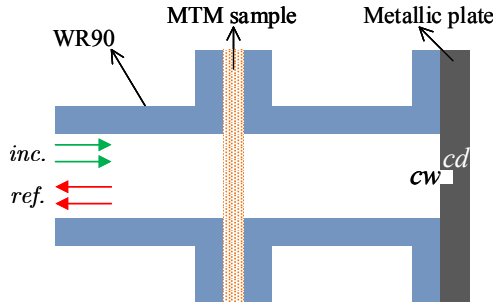

Figure 2.7.2: Metamaterial (MTM) based microwave filter design used in crack detection sensor.

generator turbines, etc.). In addition to microwave and millimetre wave techniques, other non-destructive testing (NDT) techniques include radiographic testing, ultrasonic testing, dye penetrant testing, eddy current and acoustic emission, etc. [Iva84, DW06, HOB+06]. The challenges in detection are when a crack is coated by paint or a non-corrosive substance or it is filled by dielectric fluid or material such as dust. Due to the exploitation of the resonant behavior in microwave sensors the peaks are usually sharp. Since, the sensors can be made to operate at a unique frequency, this means that the sharpness refers to increased sensitivity. The reflected signals from defected plates and from a perfect plate are compared using algorithms for analysis and treatment.

Fig. 2.7.2 shows a general setup of a crack detection system where cw and cd represent the crack width and the crack depth, respectively. Depending on the location of the crack on the metal plate behind the sensor, the input reflection coefficient undergoes a change in the magnitude of the peak or a frequency shift. The presence or absence of a crack is, therefore, observed using a reflection coefficient plot. A detailed system analysis is presented in [AHR15, KE17a].

2.8 Summary

An overview of artificial materials that are relevant to this thesis have been discussed to develop the necessary understanding. In addition, the plane wave equations have been derived and using constitutive relations for bi-isotropic media it has been shown how chirality affects the polarization of a propagating wave. Metamaterial structures and its equivalent circuit model technology have been presented, which are utilized in later chapters to develop a circuit for coupled metamaterial resonators. Moreover, the behavior of the RSRR has been discussed when transverse electric and transverse magnetic polarized waves are incident on it. It is observed that it behaves like an LC oscillating circuit. In most of the applications in this thesis resonant structures are used.

CHAPTER 3

Fundamentals of Frequency Selective Surfaces

Frequency selective surfaces are filters, which allow desired electromagnetic waves to transmit and block un-wanted electromagnetic waves (the definition is further explored in this chapter in detail). The history of frequency selective surfaces dates back to the work of G. Marconi and C. S. Franklin which was patented in the US in the year 1919 [MF19]. They proposed periodic surfaces made of wire sections for parabolic reflectors. Frequency selective surfaces gained significant importance during World War 2 due to their great potential for military applications and devices with filtering capabilities were intensely studied from thereon, specifically for reduction of the radar cross-section. However, the term "frequency selective surface" was patented in the year 1993 by Yee [Yee93]. The most common application of frequency selective surfaces are radomes[1]. Radomes provide protection against the environment and act as frequency selective surface for radiating antennas as shown in Fig. 3.0.1. In other words they are fully transparent for electromagnetic waves just like a glass window for light. In the beginning different types of materials were used in radomes, such as plexiglass, plywood, ceramic, and fiberglass, etc. With time, different approaches were introduced to increase the stealth aspect of military devices, improve communication and navigation systems. After the war, the new knowledge was extensively used for civil and commercial applications. Until now, frequency selective surfaces made up of all-metallic, all-dielectric and hybrid designs have been studied. A simple application of frequency selective surfaces is in microwave ovens to

[1] The word radome is a combination of "radar" and "dome".

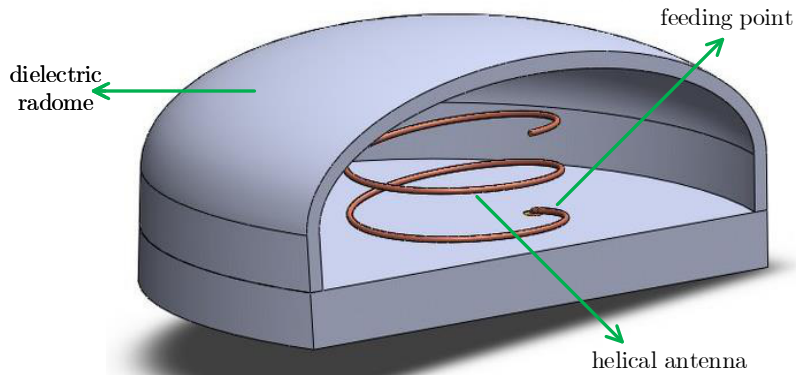

Figure 3.0.1: A helical antenna surrounded by a dielectric radome. Figure courtesy EMWORKS.

reduce the leakage and confine the electromagnetic waves inside. A stop-band frequency selective surface is used on the walls to create a cavity.

In Section 3.1, an introduction to frequency selective surfaces and its utilization in communication systems is discussed. The characteristics, excitation methods, types of frequency selective surfaces, and multilayered surfaces are discussed in Section 3.2. The physical mechanisms behind the filtering response of frequency selective surfaces are presented in Section 3.3. Section 3.4 shows frequency selective surface application with substrates and as superstrates.

3.1 Introduction

Radomes have been known for weather protection long before frequency selective surfaces with filtering capabilities were introduced. Radomes are the structures that protect the antenna from environmental exposure by encapsulating it. It was important that the impedance mismatch between the radome and the antenna must be minimum at the resonance frequency to avoid losses due to reflections. Impedance matching was achieved by setting the optimal thickness of half a wavelength. As a result, due to the presence of a thick radome, the antenna radiation characteristics may deteriorate. The effects on performance characteristics can be quantified by insertion loss (IL), reflected power, radiation pattern distortion, and insertion phase delay (IPD). The IL is directly related to the transmission loss and IPD determines the difference in the phase of the transmitted wave at a particular point in the presence of the radome to the phase of the transmitted wave when the radome does not exists. A high IPD will result in gain loss, beam deflection, grating lobes, and large changes in the bandwidth. Some examples of the radomes are illustrated in Fig. 3.1.1.

(a) Inflatable radome

(b) Metal space frame radome

(c) Aircraft nose designed to function as radome

(d) Kwajalein Mobile Range Safety System (KMRSS)

(e) US Navy amphibious transport dock NEW YORK (LPD-21)

Figure 3.1.1: Some of the radomes examples and applications. (a) Taken from [Sko90] (b) Haystack radio telescope at MIT Haystack Observatory (c) from krotoku.com (d) Remote range safety and control ship. Taken from jalopnik.com (e) Photo by Marc Piche and taken from shipspotting.com

Since the radomes were designed using homogenous dielectric materials arranged in single-layer or multi-layer configuration, the matching properties and the electrical thickness were dependent on the angle of incidence, the polarization and the frequency of the incident wave. Therefore, materials with large permittivity were used to achieve

incident angle stability, but the availability of a wide range of dielectric constant materials and mechanical fragility lead to the idea of metal inclusions in the radome structures. The arrays of metal wires or thin strips allowed wideband matching and reducing the thickness of the radome. Until the 1960s, radomes had already been developed with reactive elements, slots or patches [JCR55, KI61, OKPJ67]. Lee and Munk et al. separately demonstrated a radome with a periodic metallic screen having a dielectric layer on both sides [Lee71, PM74]. This design was considered to be mechanically strong and it improved the selectivity of the transmitted electromagnetic waves due to good matching. Munk also did a systematic study of different types of printed elements and their effect on radome performance. Later, the filtering properties of the metallic radomes were investigated and the design of frequency selective surfaces was introduced. It was studied that frequency selective surfaces can not only perform frequency filtering, but it can also perform filtering based on the incident angle and the polarization angle of the incident wave [FM83, KGR95, Mun05].

Generally, frequency selective surfaces are utilized to mitigate the problems that arise in a communication system due to radar cross-section (RCS), electromagnetic interference (EMI), and electromagnetic compatibility (EMC). They are defined as

Radar cross section is the ratio of the scattered power by an object to the power incident on the object. In [Bal12], it is defined as "the area intercepting the amount of power that, when scattered isotropically, produces at the receiver a density that is equal to the density scattered by the actual target."

Electromagnetic interference is the performance degradation of an electronic equipment, transmission channel or system by an external electromagnetic disturbance.

Electromagnetic compatibility is the ability of an electrical equipment or a system to function satisfactorily in its electromagnetic environment without introducing intolerable electromagnetic disturbances to anything in that environment [Voc].

In addition, frequency selective surfaces are also used to achieve extra-ordinary characteristics and performance enhancement of antenna systems, for example, improving gain or reducing grating lobes, etc.

In communication systems filters play an important role to distinguish signals and decode information or reduce noise and interferences. Similarly, in wireless communication systems often many radiating devices are placed next to each other due to limited space, for example in ships, aircrafts, automobiles, and handheld devices, etc. This arrangement can cause electromagnetic interference among the devices that is highly undesirable. Another aspect, which is of major concern to antenna designers is the radar cross-section. Conventional antennas such as a horn antenna suffer from a large radar cross-section

signature due to large physical size. Planar microstrip antennas such as dipoles and patches require a metallic ground reflector and this can lead to backscattering, which can deteriorate the radar cross-section signature. In such circumstances, frequency selective surfaces are used to transmit, reflect, or absorb specific frequency bands. Frequency selective surfaces are deployed as superstrate on top of an antenna or as high impedance ground plane for an antenna. Frequency selective surfaces can be generally defined as

> Frequency selective surfaces are spatial filters composed of similar or different types of elements arranged periodically to form an array which has a specific response (i.e., reflect, transmit or absorb) to the incident field and incident wave angle and/or polarization for a certain band of frequencies.

3.2 Characteristics of frequency selective surfaces

The spectral selectivity of a frequency selective surface when an electromagnetic wave is incident on it depends on the types of elements it is composed of, geometry of the elements, thickness of the surface, mutual interactions, and periodicity, etc. Therefore, while designing a frequency selective surface careful thoughts must be given to the factors influencing the behavior of the frequency selective surface to achieve the desired characteristics.

3.2.1 Periodic structures

A structure is periodic when identical elements are arranged in the form of an array extended infinitely in one, two or three dimensions with fixed inter-element spacing. Periodic structures make the design process fast and simple because the problem is narrowed down to a unit cell structure. Non-periodic structures can also have spectrally selective responses. Metasurfaces are usually non-periodic and they are primarily used to modify the wave fronts. In metasurfaces, the elements are a function of position to control amplitude, phase, polarization, etc. In this thesis periodic structures are considered for designing frequency selective surfaces (FSSs).

3.2.2 Excitation of frequency selective surfaces

To understand the excitation principle for periodic structures, elements of two types are considered: dipoles and slots. The orientation of the dipole elements or the slot

elements in an array determines the polarization mode of the wave exciting the particular element. To excite a periodic array there are two ways: by an individual source (generator) mounted to each element or by an incident electromagnetic plane wave illuminating the structure. The periodic arrays that are excited by a generator are called *active arrays*. The periodic arrays that are excited by an incident wave are called *passive arrays*.

Dipole arrays

A two dimensional dipole array is formed by periodically arranging metallic strips of length $2l$ and inter-element spacing D_x in x-direction and D_y in y-direction. In the case of an active array formation as shown in Fig. 3.2.1(a), a voltage generator is connected to every element and each voltage generator has the same amplitude $V_\circ$. If m and n represent the indices of the 2D array, which locate the specific position of an element. In order to have a periodic surface with linear phase variation across the active array then the voltage at any element is given by [Mun05]

$$V_{mn} = V_\circ e^{-j\beta m D_x s_x} e^{-j\beta n D_y s_y}, \tag{3.2.1}$$

where s_x and s_y represent the directional cosines along the x- and y-axis, respectively.

The passive dipole array is shown in Fig. 3.2.1(b). An incident plane wave $E_y^i(-z)$ whose electric field vector is positioned in y-direction excites the periodic structure. The elements of the dipole array resonate, resultantly, the incident wave is partly reflected back ($E_y^r(z)$) and partly transmitted ($E_y^t(-z)$) in the forward direction. At the resonance frequency assuming no grating lobes, the reflection coefficient (Γ) and the transmission coefficient (τ) can be defined as

$$\Gamma = \frac{E^r}{E^i}, \tag{3.2.2}$$

$$\tau = \frac{E^t}{E^i}. \tag{3.2.3}$$

The polarization of the incident electric field which excites electric currents on the metallic strips, depends on the orientation of the dipoles.

Slot array

The other type of an array is made of periodic slots as shown in Fig. 3.2.2. It is the complementary array with respect to the dipole array. Two arrays are complementary to one another such that if they are placed on top of each other they form a perfect conducting

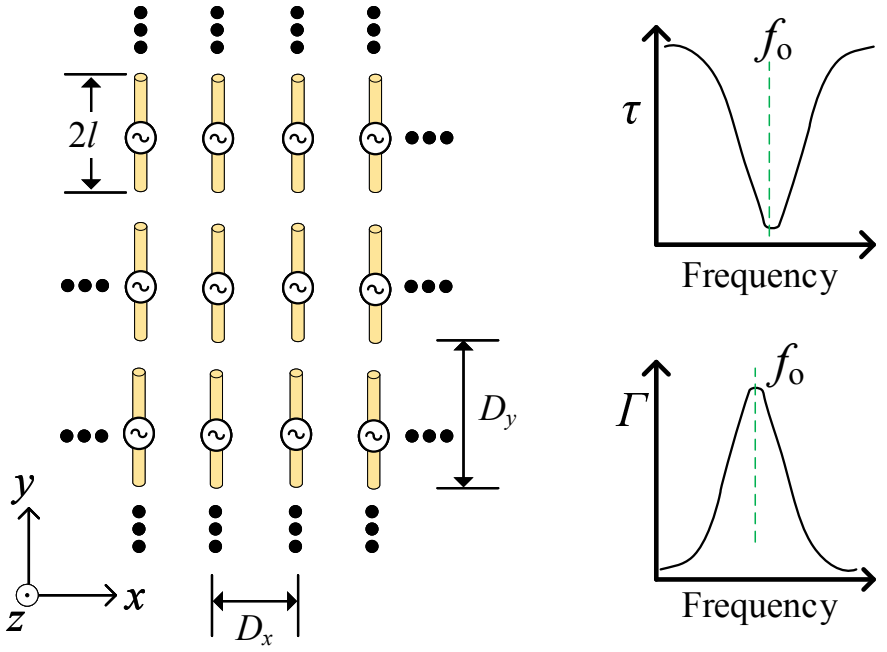

(a)

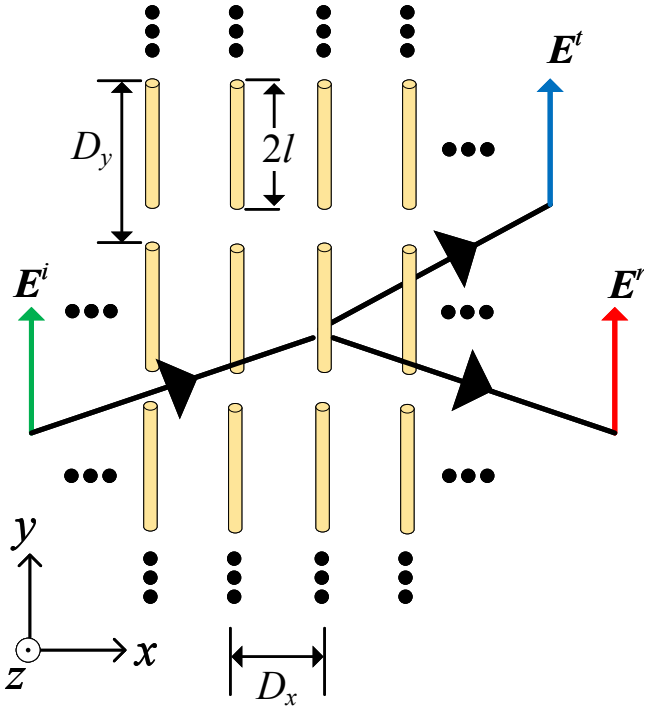

(b)

Figure 3.2.1: Metallic strips periodically arranged in the xy-plane. Each strip behaves like a dipole having an impedance Z_l. (a) An active array formation with voltage generator attached to each element. (b) A passive array formation with an incident wave exciting electric currents in the structure. Figure concept adopted from [Mun05].

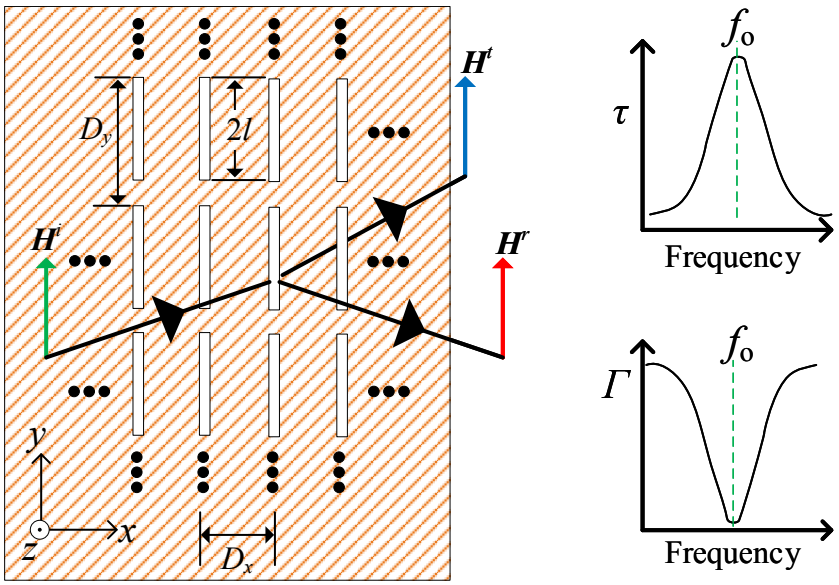

Figure 3.2.2: Slots on metal film are arranged periodically in the xy-plane. Each slot has an admittance Y_l. Magnetic currents do not exist, however, we know that using the equivalence principle electric fields in the slots can be represented by equivalent magnetic current densities. Figure concept adopted from [Mun05].

plane. The slot array can also be excited passively or actively. The difference is that in this type of array equivalent magnetic currents are excited in the slots, unlike electric currents excited on the metallic strips in the dipole array case. Under the conditions that the structure has perfect conducting metal and it is infinitely thin, the Babinet's principle states that the transmission coefficient for one array is equal to the reflection coefficient of the complementary array.

3.2.3 Types of frequency selective surfaces

The physical geometry of the frequency selective surface can be broadly divided into three classes: metallic, all-dielectric and hybrid. The characteristics of frequency selective surfaces based on reflection coefficient and transmission coefficient can be categorized as bandpass, low-pass, high-pass and band-stop.

Metallic frequency selective surfaces

The first class of frequency selective surfaces only have metallic elements that are responsible for frequency selectivity. There are different varieties of geometries possible

to constitute metallic arrays. The most fundamental geometries are metallic patches and wire-grids.

An array of metallic square patches as shown in Fig. 3.2.3(left) is known to have capacitive characteristics and it acts as a low-pass filter. The general first order frequency response of such an array is shown in Fig. 3.2.3(right). It reflects the higher frequencies and transmits low frequencies. The higher-order response is discussed in Section 3.2.4. Metallic patches can take different shapes, e.g., triangular, circular or hexagonal, etc. These arrays are also known as reflective surfaces or capacitive surfaces. The gaps (inter-element spacings) between the square patches in vertical and horizontal direction creates capacitive effects. These gaps also influence the incident angle stability of the surface. In order to maintain the characteristics of the structure at oblique incidence, the inter-element spacing must be very small relative to the free-space wavelength. Furthermore, gaps are related to capacitance that means large gaps will have small capacitance and vice versa. The capacitance can also be controlled by using tunable varactors.

Wire-grids are the complementary form of square patches as shown in Fig. 3.2.4(left). They have inductive characteristics and act as a high-pass filter. The general first order frequency response of such an array is shown in Fig. 3.2.4(right). Such arrays are also known as transparent surfaces or inductive surfaces. When a vertically polarized wave is incident on such surfaces, the vertical metallic lines act as infinitely long, therefore, the frequency response resembles to that of an inductor. However, the horizontal lines have large separation, which show very weak capacitance. This can result in the creation of grating lobes. Moreover, wire-grid arrays also suffer from oblique incidence instability

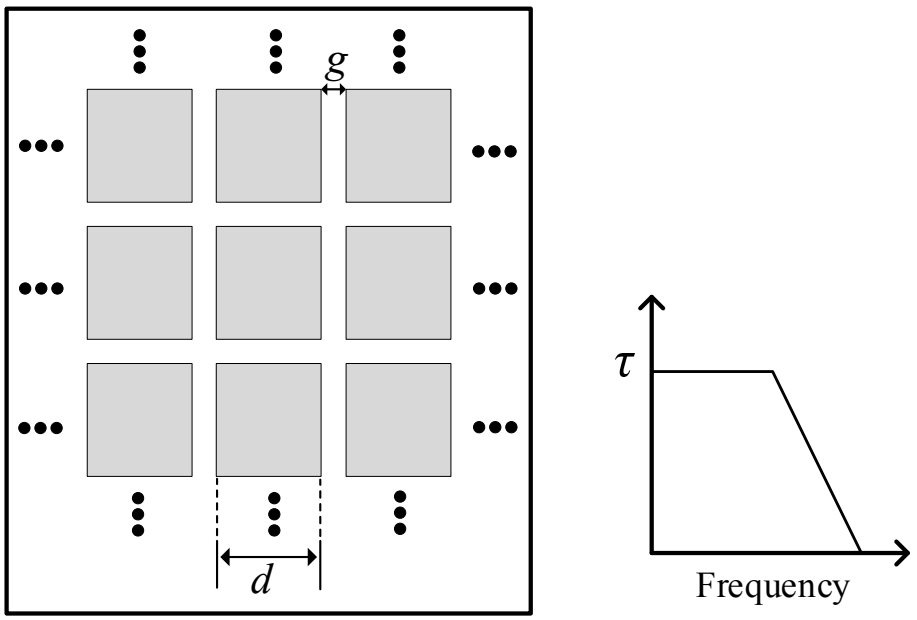

Figure 3.2.3: Periodic metallic square patches (left) whose response is equivalent to a low-pass filter (right).

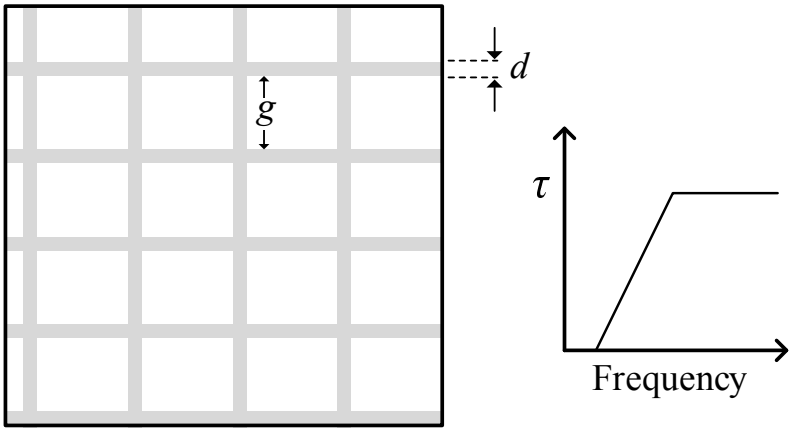

Figure 3.2.4: Metallic wire-grid frequency selective surface (left) whose response is equivalent to a high-pass filter (right).

(relatively larger sensitivity to incidence angle compare to patch arrays due to large spacing). The capacitance can be increased by filling the loop/aperture with a patch type element or dipole type element, which will create regions with strong capacitive coupling.

All-dielectric frequency selective surfaces

In dielectric frequency selective surfaces different techniques are used to achieve spectral selectivity. These include natural absorption, multilayered dielectric materials, and guided-mode resonance. The physical mechanisms behind these techniques are discussed in the subsequent Section 3.3.

Dielectric frequency selective surfaces are mostly used as reflective surfaces or absorption surfaces. They are not ideal for transparent surfaces due to attenuation of the wave passing through the structure. Dielectric absorbers are often used in anechoic chambers to minimize the reflections. There are natural materials which have tendency to absorb electromagnetic waves. The absorbed energy is lost in the form of heat. These materials provide broadband response. A synthetic approach utilizes multiple discrete layers of dielectric material to form a Bragg reflector or impedance gradient index (discussed in Section 2.2.1 and Section 2.7.1). To achieve the desired Bragg reflector frequency response, the all-dielectric frequency selective surfaces need to be multiples of a quarter of a wavelength. This limitation does not have any serious implications for high frequencies, i.e., optical frequencies, however, at microwave frequencies this will lead to a large thickness which may not be desirable. Since dielectric frequency selective surfaces are not the subject of this thesis, for further details and in depth discussion on this topic, the reader is encouraged to refer to the publications [Sav05] and [KLL$^+$13].

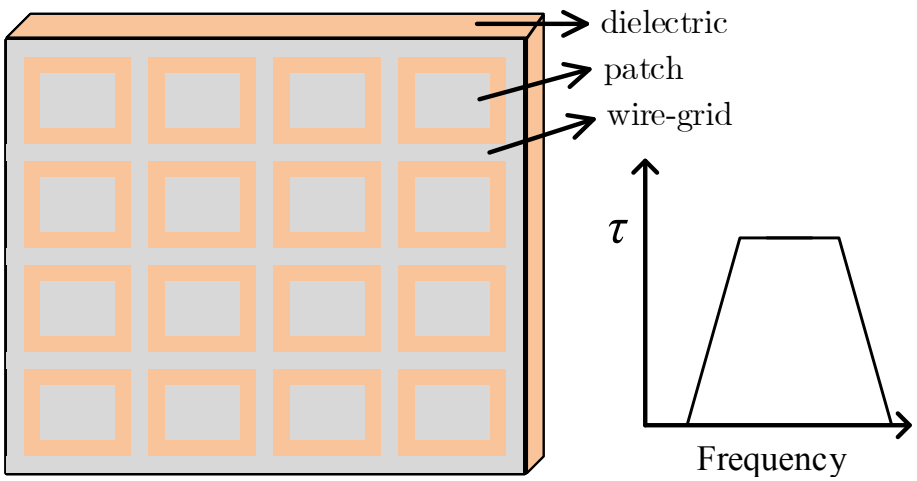

Figure 3.2.5: Metallic patches and wire-grid frequency selective surface (left) whose response is equivalent to a band-pass filter (right).

Hybrid frequency selective surfaces

In hybrid frequency selective surfaces, the metallic type of elements can be used on top of the dielectric substrate to gain mechanical strength, reduction in the thickness, and good impedance matching. In addition the hybrid structures also provide control over the behavior of the surface because of distinct conducting elements that cause mutual coupling, which can be manipulated to achieve the desired characteristics.

It is important to note that the periodic metallic array design can not be treated separately without dielectric layer. The dielectric layer affects the resonance frequency of the periodic structure. Munk illustrated in [Mun05] that if the periodic structure is surrounded by dielectric layers of infinite thickness, its resonance frequency ($f_\circ$) shifts downward to ($f_\circ/\sqrt{\varepsilon_r}$), where ε_r is the dielectric constant of the material surrounding the periodic structure. For dielectric layers with small thicknesses, the resonant frequency shifts between $f_\circ$ and $f_\circ/\sqrt{\varepsilon_r}$. However, for a single dielectric layer on any side of the periodic structure, the largest resonance shift would be $f_\circ/\sqrt{(\varepsilon_r+1)/2}$.

We have seen previously that patch-type frequency selective surfaces give low-pass response and wire-grid type frequency selective surfaces give high-pass response. In order to achieve band-pass or band-stop characteristics, a wire-grid frequency selective surface is loaded with patches as shown in Fig. 3.2.5(left). This will increase the capacitance in the structure and a strong resonance can be obtained. The frequency response of this combined array is shown in Fig. 3.2.5(right). The frequency response of the frequency selective surface obtained by combining wire-grids and patches will not be a simple addition of the two responses, but the affect of the dielectric layer and the mutual coupling will have to be considered. Similarly, the complementary form of Fig. 3.2.5(left) is shown in Fig. 3.2.6(left) and its frequency response is shown in Fig. 3.2.6(right).

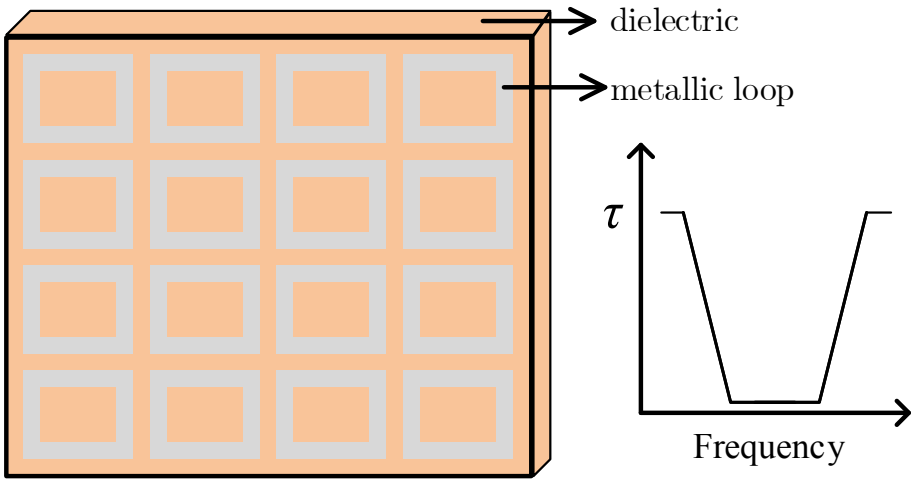

Figure 3.2.6: Periodic array of metallic loops (left) whose response is equivalent to a band-stop filter (right).

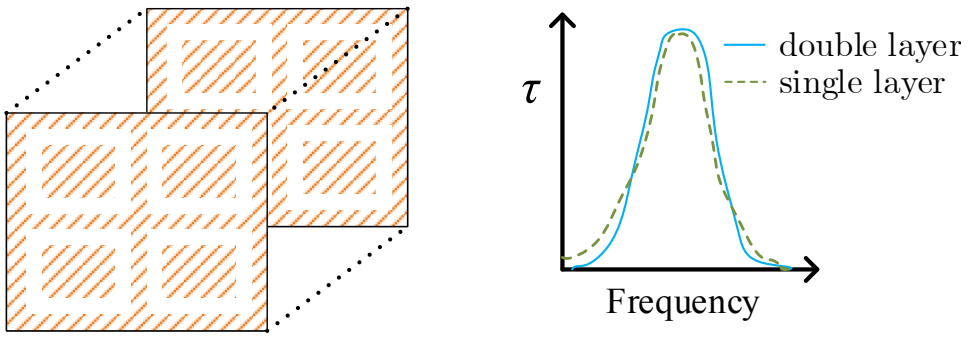

Figure 3.2.7: Two layers of periodic metal surfaces (slot-type) cascaded without dielectric material in between (left). Frequency response for a single-layer design and double-layer design (right). Please note that the frequency response is not the true depiction of the actual structure on the left.

3.2.4 Cascaded periodic structures

Frequency selective surfaces that have been discussed until now show frequency selectivity at the resonance frequency which implies narrowband response. However, in many applications a wideband response is desired as well as incident angle stability and sharp edge roll-offs. There are essentially three ways that we discuss here [Mun05].

Metal-metal cascading: Two or more layers of metallic arrays (periodic surfaces) are cascaded behind each other and there is no dielectric layer between them. Fig. 3.2.7 shows a comparison between a single-layer design and a double-layer design. It can be seen that for the double-layer design the edges fall sharply and the band top is much flatter. However, this kind of design shows considerable bandwidth variation for oblique incidence angles and different polarizations.

Dielectric-metal-dielectric: A traditional approach is to add a dielectric slab on both sides of the metallic array to improve the incident angle stability. The thickness and the dielectric constant of both the dielectric slabs must be the same. It may provide considerable bandwidth as shown in Fig. 3.2.8 but may present a problem where conformal frequency selective surfaces are required to cover the structure on curved surfaces. In addition, a dielectric superstrate would introduce insertion loss and the wide range of dielectric constants may not be commercially available. Though, it does present a relatively stable angular response.

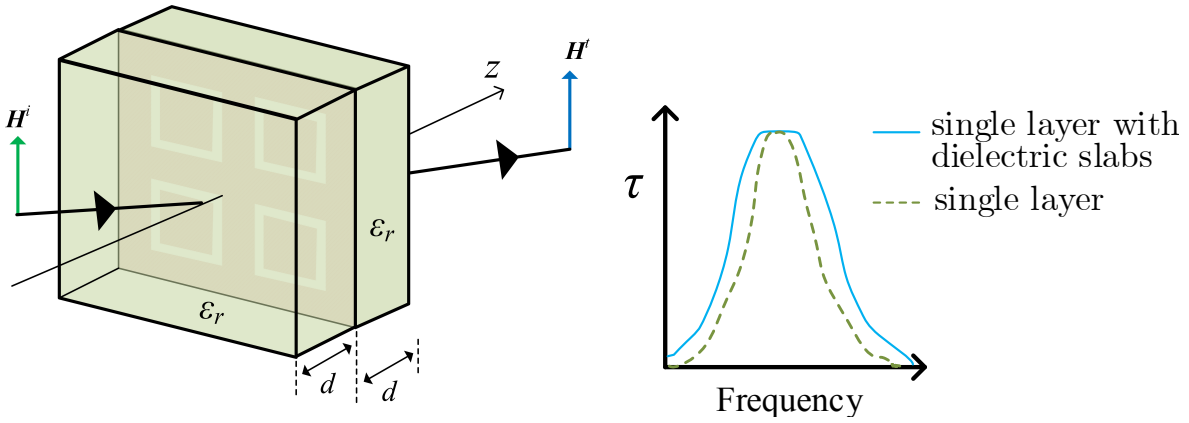

Figure 3.2.8: A single-layer periodic metal surface (slot-type) sandwiched between dielectric slabs of thickness d and dielectric constant ε_r (left). A comparison of the frequency response for a single-layer without dielectric slabs and with dielectric slabs on both sides (right). Please note that the frequency response is not the true depiction of the actual structure on the left.

Miniaturization: The concept behind this approach is to reduce the element size and the inter-element spacing. The former will allow the use of frequency selective surfaces on conformal surfaces and the latter gives a stable angular response and reduced grating lobes due to diffraction. Wideband behavior can be obtained by using multiple elements with overlapping individual resonance frequencies so that when combined it has a wideband response as done by [XHLZ13, GSZ13]. Increasing the number of similar elements per unit cell results in higher order responses as discussed in [OS16].

3.3 Physical mechanisms of frequency selective surfaces

The underlying mechanisms to design fully reflective surfaces, transparent surfaces, or absorption surfaces can be broadly classified into two groups: absorption based designs and redirection based designs. This means that frequency selectivity can be attained by

either absorbing the energy or redirecting it.

3.3.1 Absorption

In absorption parts of the electromagnetic waves are absorbed while other parts are reflected or scattered back to the medium of incidence. Examples include the Salisbury screen as shown in Fig. 3.3.1(a), where a $\lambda_g/4$ (λ_g is the wavelength of operation) lossy material is backed by a metal layer. In order to increase the loss metallic resonators are included in the lossy material as shown in Fig. 3.3.1(b). They are also known as circuit analog absorbers. Similarly, as discussed previously dielectric structures can also be used to trap the energy inside the materials. An example of dielectric absorbers is displayed in Fig. 3.3.1(c).

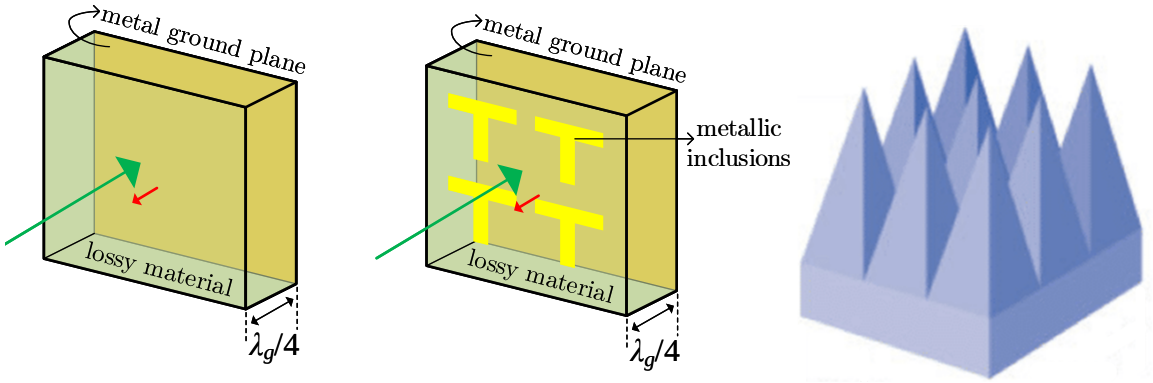

Figure 3.3.1: Absorptive frequency selective surfaces. (a) Salisbury screen (b) Circuit analog absorber (c) Pyramid absorber.

3.3.2 Redirection

In this case, electromagnetic waves are redirected or scattered using interference, guided-mode resonance, or grating structures which can cause diffraction. When an electromagnetic wave is incident on a stack of different material layers (ideally non-lossy) it undergoes partial reflection and partial transmission, the frequency selectivity is the response due to the overall interference of the scattered waves. It is also called longitudinal resonance and is illustrated in Fig. 3.3.2(a). Fig. 3.3.2(b) shows the scattering due to gratings on the structure. These scattered waves are also known as spatial harmonics because the grating period longer than the incident wavelength diffracts the waves into discrete modes as shown in Fig. 3.3.2(c). The mode 0 represents the reflected wave with

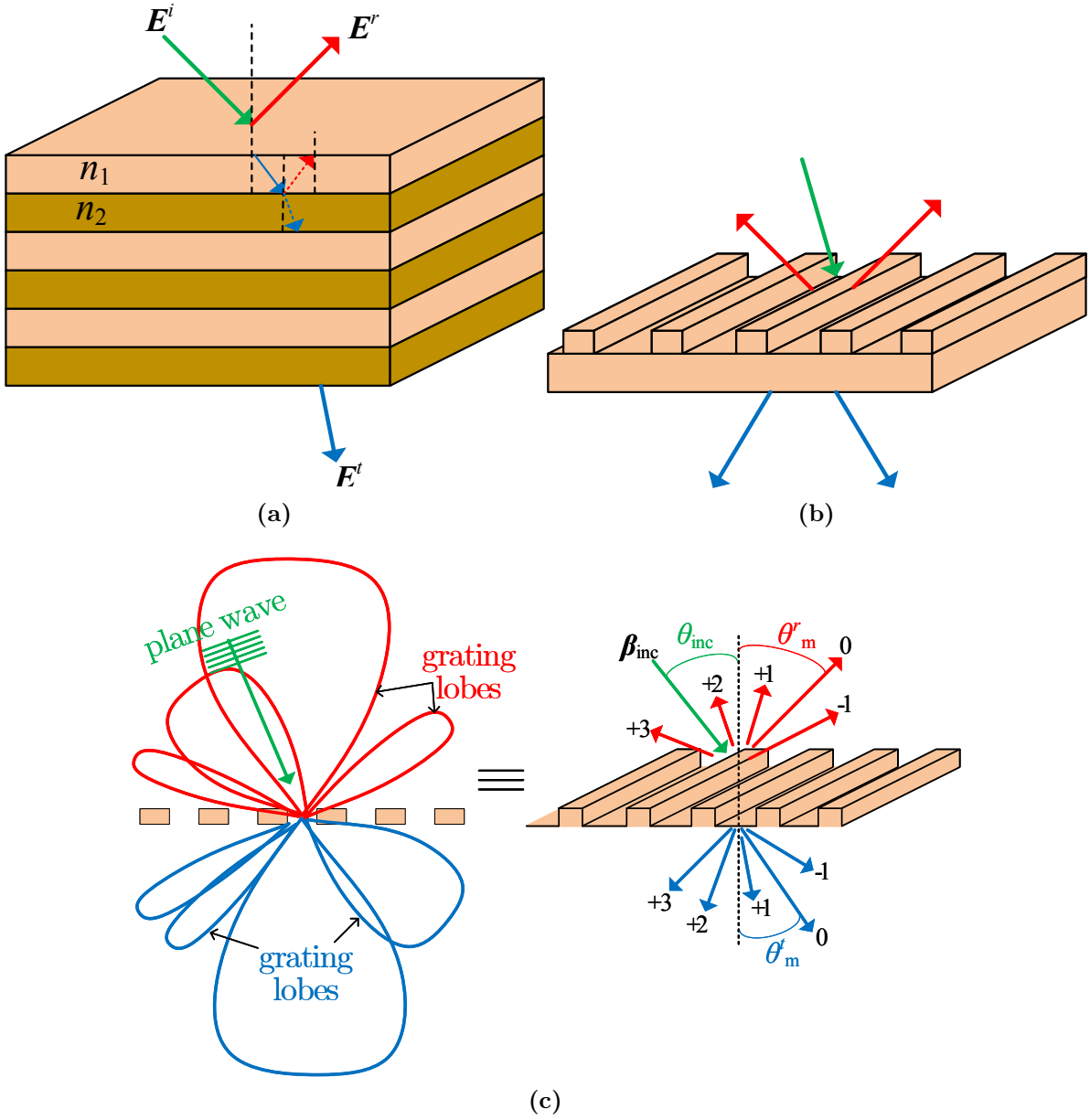

Figure 3.3.2: Redirection mechanisms. (a) Longitudinal resonance (b) Redirection due to grating structure (c) Discrete modes on a typical grating structure.

an angle of reflection θ^r_m. Positive numbers are assigned to modes with angle of diffraction less than the angle of reflection and negative numbers are assigned to modes with angle of diffraction greater than the angle of reflection. The angles of the modes depend on the materials, grating period, diffraction order, and wavelength. This kind of structure may have very limited applications because the diffracted energy will be lost. However, it can be useful in obscuring an object. Therefore, the concept of diffraction from the grating structures is extended to guide a wave in a particular direction to produce frequency selective response. The redirection mechanism is known as guided-mode resonance.

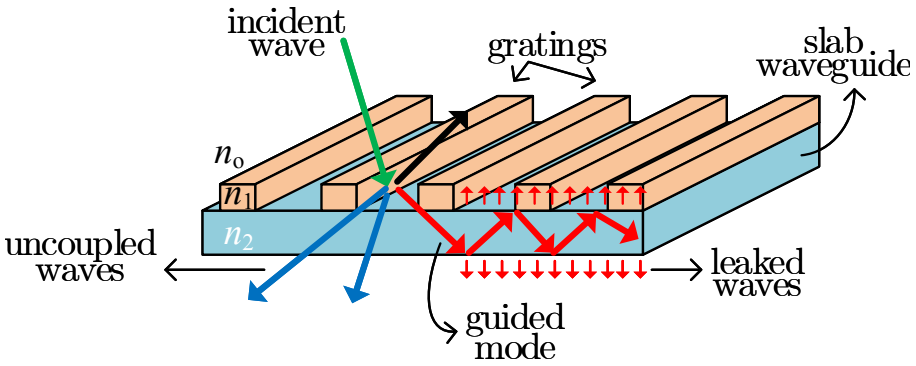

Figure 3.3.3: Guided-mode resonance.

A grating structure and a slab waveguide are brought close to each other so that they are electromagnetically coupled [BRS+12]. The discrete modes from diffraction are coupled into the slab and guided within the waveguide transversely. An illustration of guided-mode resonance is shown in Fig. 3.3.3. The wave can only be coupled and guided under the condition that the effective dielectric constant of the grating structure which produces discrete modes is less than the dielectric constant of the slab waveguide and greater than the dielectric constant of the surrounding media. The overall frequency response due to the mechanism of the guided-mode resonance can be understood from Fig. 3.3.3. When an incident electromagnetic wave (or applied wave) is impinging on the gratings, a number of discrete modes are produced. The diffracted mode, whose phase matches with the phase of the supported mode of the slab waveguide, is coupled to the guided wave. At resonance, a part of the applied wave is coupled into the guided mode and a part of it is reflected or transmitted through the frequency selective surface. The coupled wave propagates through the slab waveguide, however, due to interaction with the gratings it slowly leaks out from the slab waveguide. The interference between the leaked waves and the reflected or the transmitted waves (uncoupled waves) are responsible for the overall frequency selective response. At frequencies other than the resonance frequency, the structure exhibits a response of a multilayer device. The important aspects of this mechanism are: 1) the position of the resonance frequency is a function of the grating period and the angle of incidence. 2) increasing grating period relative to the wavelength will increase the number of diffracted modes, which will result in multiple resonances.

3.4 Frequency selective surfaces based ground planes or superstrates

The deployment of frequency selective surfaces is not limited to radomes but they are also deployed in antenna systems to enhance radiation characteristics. In many applications antenna systems are required to have high performance and low profile.

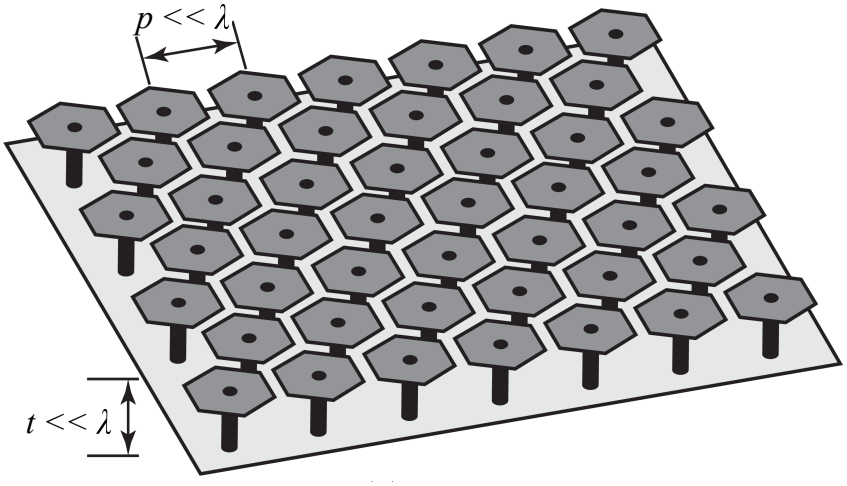

Figure 3.4.1: A common artificial impedance surface [Bal12]. Hexagonal metallic patches connected to metallic ground through a via. An antenna is usually placed over it.

These qualities are accomplished by incorporating frequency selective surfaces on top of antennas as superstrates or by replacing a conducting ground plane of the antenna with a specialized frequency selective surface.

3.4.1 High impedance surface

A special type of metamaterial based frequency selective surfaces are designated as artificial impedance surfaces (AISs) or high impedance surfaces (HISs). We know from image theory that a perfect electrically conducting plane, and a perfect magnetically conducting plane introduce 180° and zero phase shift in the vertically reflected wave, respectively. However, in general the reflection phase of an AIS varies between $-180°$ to 180°. Therefore, AISs are more versatile and unique. AISs are *engineered electromagnetic surfaces* that are "developed to modify the impedance boundary conditions of the surface of the structure that leads to controlling the radiation characteristics, i.e., pattern and radiation efficiency, of an antenna placed at or near them" [Bal12]. They are usually used as a substrate. In microstrip antenna arrays surface waves are produced that travel within the substrate. These surface waves have vital contributions in developing coupling between the array elements, which deteriorate the radiation characteristics of the array. Among many uses of AISs, some of them are controlling the phase of the reflection coefficient, controlling the edge diffraction of the antennas, controlling the frequency response (bandpass, bandstop etc.), reconfiguring the surface impedance or manipulating the propagation of surface waves [Bal12]. AISs exhibit properties similar to perfect magnetic conductors. The most common example of these surfaces is an array of mushroom-like structures as shown in Fig. 3.4.1.

We know that nearly perfect electric conductors (PECs) exists in nature while perfect magnetic conductors (PMCs) do not exist, but structures with PMC-type behavior in a certain band of frequencies can be artificially designed. Furthermore, according to electromagnetic boundary conditions, it is known that the tangential component of the electric field vanishes at PEC surfaces. This is also obvious from the image theory. Therefore, in order for an electric dipole to have maximum radiation in the direction normal to PEC, it must be placed at least $\lambda_\circ/4$ above PEC [Bal12]. This is mostly not desirable in many applications because of aerodynamic considerations as well as a large radar cross-section signature. In such circumstances, it is highly beneficial to design and fabricate PMC surfaces artificially (these surfaces only exhibit PMC-type properties in a certain band of frequencies). The artificial PMC surfaces are also referred to as *band-gap* or *band-limited* surfaces. AISs exhibit PMC-like behavior. Lately, a lot of work has been done to achieve PMC-type properties and many designs have been proposed [KWM$^+$05, MML02, KKM05, NSS17, FS09]. A typical AIS is shown in Fig. 3.4.1 in which a periodic array of metallic hexagon patches is connected to a ground plane through vias. The substrate has a very small thickness ($<\lambda/10$) which could also be air. The vias are essential in this design to suppress surface waves within the substrate. The surface has been discussed in detail in [Sie08].

3.4.2 Superstrate

Frequency selective surfaces that are placed on top of an antenna are often known as superstrate. The advantage of such an arrangement is that the challenges in antenna array

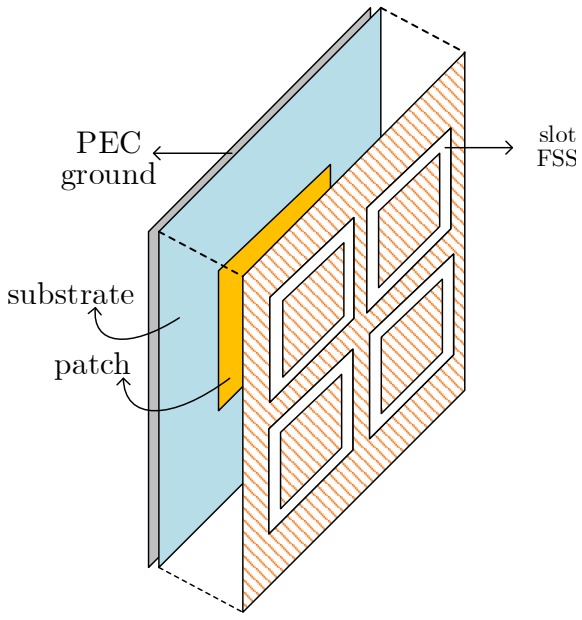

Figure 3.4.2: A slot-type frequency selective surface deployed as a superstrate on a microstrip patch antenna.

design are dealt with separately from the electromagnetic waves manipulation. Frequency selective surface based superstrates have been used to enhance the directivity of microstrip antennas [LYMP04], as reconfigurable passband screen by inserting tunable capacitors in the slot-type element [GLS+19], gain enhancement of the antenna [AGF+16], radar cross-section reduction [CLL+15] and beam steering, etc. Traditionally frequency selective surfaces were placed at a larger distance from the antenna because incident angle stability was a major challenge. Over the period of time as the size of the elements constituting the array has reduced along with reduction in the inter-element spacing, it became possible to place frequency selective surfaces very close to an antenna. Fig. 3.4.2 displays a frequency selective surface used as a superstrate on a simple patch antenna.

3.5 Summary

The scope of frequency selective surfaces was broadened when its filtering characteristics were discovered and explored. They are very effective in terms of design flexibility, efficiency, and cost to: reduce the radar cross-section of objects, and reduce electromagnetic interference of and from communication and electronic systems. Frequency selective surfaces are also very handy for wave manipulation, i.e., polarization conversion or beam steering, etc. The most fundamental elements used are patches and slots while the most common utilization of frequency selective surfaces are in substrates or on top of antenna systems.

Chapter 4

Isotropic Frequency Selective Surface

In this chapter, periodic resonating elements on a dielectric substrate are presented in two configurations. In the first configuration, a T-type resonator is placed inside a rectangular split-ring resonator (RSRR) for the purpose of being used in frequency selective surfaces (FSSs), hollow waveguide filters and absorbers. In the second configuration, each element in the structure is rotated 90° clockwise to eliminate the polarization angle dependency. The behavior of the structures as a function of frequency, incident angle, polarization and the geometric parameters is presented. It is observed that the structures can be operated in multiple bands with good angle and polarization stability. Moreover, these structures can be replicated for higher frequencies by scaling the dimensions. The content of this chapter has been widely taken from [KE18] and [KE19c].

In Section 4.1, basic principles followed to design a unit cell for FSSs are discussed. The structure geometry and the parameters of the unit cell are illustrated as well. The transmission characteristics of the designed FSSs are discussed in Section 4.3. Parametric analyses and the fabricated waveguide filter design and absorber design are discussed in Section 4.4 and Section 4.5, respectively. A performance comparison with some recent FSSs proposed in literature is presented in Section 4.6.

4.1 Methodology and unit cell design

4.1.1 Design Principle

Consider a periodic array of passive resonators with subwavelength unit cell dimensions. The array would ideally behave as a reflector/transparent surface around a resonant frequency and transmit/reflect at non-resonant frequencies. Periodicity is one of the important factors in designing a desired FSS. The guided wavelength, denoted by λ_g, is much greater than the structural average cell size p, so that the structure is effectively homogeneous. In practice, the relationship $p \leq \lambda_g/4$ is obeyed in microwave engineering, to ensure that the screen will be predominantly refractive rather than diffractive [CI05]. The frequency response of an FSS is commonly polarization dependent and sensitive to the incidence angle at the resonance frequency, which may not be a desired behavior. The addition of a dielectric superstrate or miniaturizing the element size of the periodic array can provide a more stable angular response [SB07, OS17]. In this chapter, the approach is to work with a polarization independent 2-by-2 elements unit cell (referred to as quad element unit cell), which utilizes miniaturization of the elements along with a rotationally symmetric arrangement such that the period of the super cell as shown in Fig. 4.1.1(b) is not increased as compared to the single element unit cell with not rotated elements as shown in Fig. 4.1.1(a). The change in the behavior of these structures as a result of changing geometric parameters is mainly due to the change in the reactances of the structure and coupling effects. Another important design factor is the insertion loss (IL). The optimal goal would be to minimize the IL to less than 0.5 dB and to attain sharp roll-off on either side of the passband [YWM+16].

4.1.2 Design Procedure

Two structure configurations, a) single element (SE) unit cell, and b) quad element (QE) unit cell, are discussed in this chapter, which are shown in Fig. 4.1.1(a) and 4.1.1(b). The structures are designed on Rogers RO4350B substrate with relative permittivity $\varepsilon_r = 3.48$, loss tangent 0.0037 and thickness of 0.254 mm. The unit cell structures, its geometric dimensions and other details are presented in Fig. 4.1.1. Copper is used as the conducting layer having a thickness of 0.0175 mm. The QE unit cell is constructed by rotating the SE unit cell 90° clockwise. This design, due to the 90° rotational symmetry is independent of the incident polarization angle (discussed in Section 4.3). The behavior of FSSs based on passive thin resonators is generally narrowband. The bandwidth depends commonly on the number of layers.

The developed structure has a single layer design. It is composed of an inverted-T

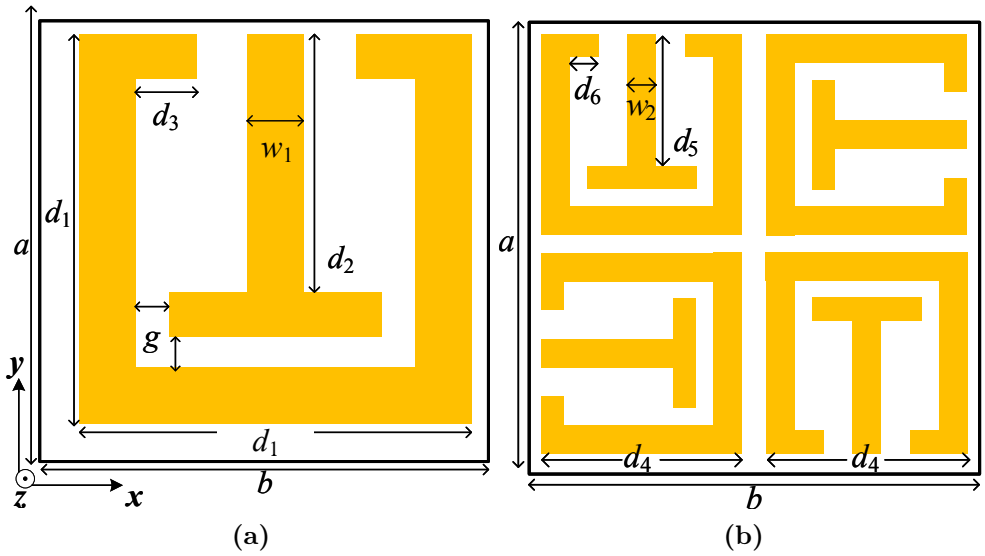

Figure 4.1.1: Unit cell FSS structures (a) single element (SE) unit cell (b) quad element (QE) unit cell, where $a = b = 10\,\text{mm}$, $d_1 = 9\,\text{mm}$, $d_2 = 7.2\,\text{mm}$, $d_3 = 1.5\,\text{mm}$, $d_4 = 4.5\,\text{mm}$, $d_5 = 3.8\,\text{mm}$, $d_6 = 1.0\,\text{mm}$, $w_1 = 0.8\,\text{mm}$, $w_2 = 0.25\,\text{mm}$, and $g = 0.2\,\text{mm}$.

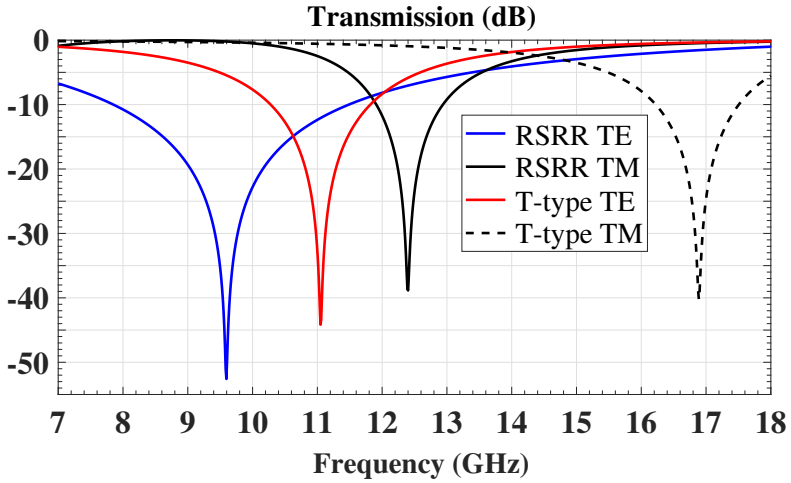

Figure 4.1.2: Simulated transmission coefficient at normal incidence for the RSRR resonator and the T-type resonator.

resonator surrounded by an RSRR. Both of the resonators have a distinct and independent resonance frequency which is affected in particular by the gap between the elements and other geometric parameters. The transmission coefficients obtained for each resonator when transverse electric (TE) and transverse magnetic (TM) polarized waves are incident normally are shown in Fig. 4.1.2. The resonance frequencies for the RSRR and the inverted-T resonator are (9.59, 12.4) GHz and (11.05, 16.9) GHz, respectively, for (TE, TM) incident polarizations. The structure has suppressed harmonics which is a requirement for microwave absorbers that are used in energy harvesting systems. The

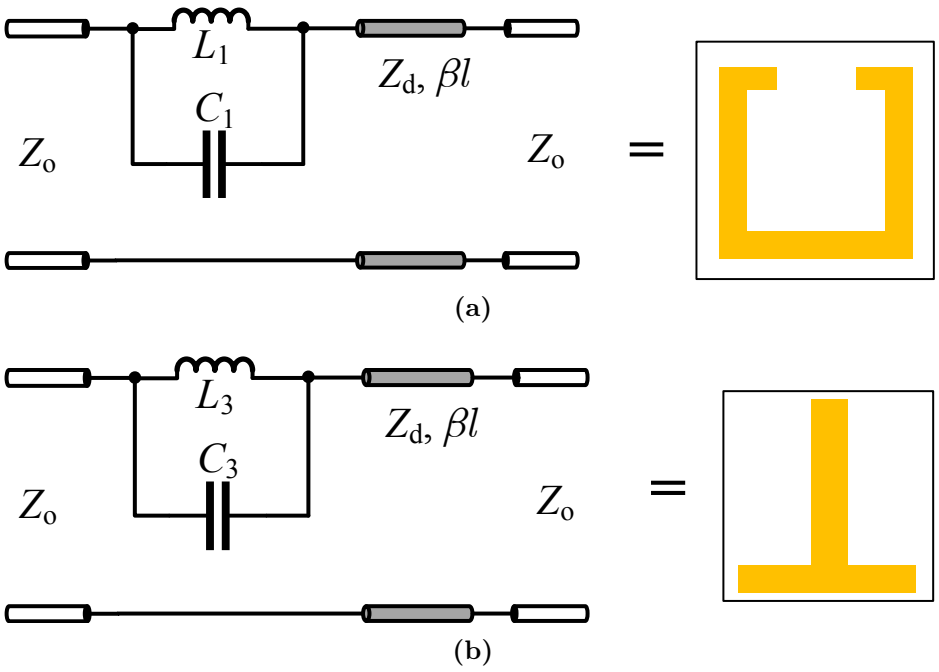

Figure 4.1.3: Equivalent circuit model of the resonating elements based on independent behavior (a) the RSRR (b) the T-type.

designs have been simulated in CST Microwave Studio with the frequency domain solver [CSTom]. The average cell sizes are $p = \lambda_g/2.4$ and $p = \lambda_g/4.8$ for the SE unit cell and the QE unit cell, respectively. Here, the guided wavelength λ_g corresponds to the center frequency of 12.5 GHz. Unit cell boundary conditions are used in (x, y)-direction to have the periodic effect and a perfectly matched layer in z-direction (other boundary conditions for specific cases are mentioned in subsections).

4.1.3 Unit cell equivalent circuit

An equivalent circuit of the proposed FSS structure has been obtained, which depicts the topology of a dual-bandstop microwave filter. It is known that the conducting strips can be modeled with inductors and gaps with capacitors [CI05]. LC resonator circuits behave as filters at particular frequencies because at resonance the capacitive and the inductive reactance of the circuit are equal in magnitude. Alternatively, at resonance the parallel impedance is maximum and the series impedance is minimum, thereby, producing filtering effects at particular frequencies. Two equivalent circuits of the resonating elements of the SE unit cell are constructed as shown in Fig. 4.1.3, keeping in view the independent transmission behavior of each resonator as shown in Fig. 4.1.2.

The first circuit models the RSRR with the parallel L_1C_1 reactive elements and the second circuit models the T-type resonator with the parallel L_2C_2 reactive elements. It

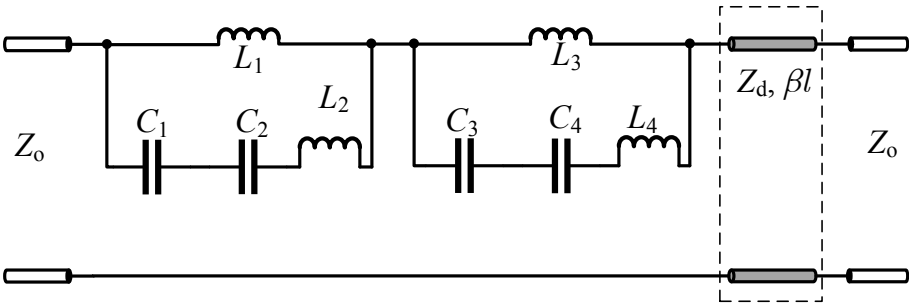

Figure 4.1.4: Equivalent circuit model of the SE unit cell structure where $L_1 = 2.54\,\text{nH}$, $L_2 = 1.781\,\text{nH}$, $L_3 = 7.141\,\text{nH}$, $L_4 = 0.570\,\text{nH}$, $C_1 = 0.108\,\text{pF}$, $C_2 = 1.6\,\text{pF}$, $C_3 = 0.029\,\text{pF}$, $C_4 = 0.0362\,\text{pF}$.

is observed that each of the resonators has a transmission zero at its resonant frequency, f_z^{rsrr} and f_z^t, in the band of operation. The RSRR gives rise to a stopband at a lower frequency than the T-type resonator ($f_z^{rsrr} < f_z^t$). The two equivalent circuits are then combined and the effect of coupling or mutual interactions between the RSRR and the T-type resonator on the behavior of the FSS are accounted for by series (L_2, C_2) and (L_4, C_4) elements as shown in Fig. 4.1.4. The complete equivalent circuit is no more the depiction of the individual resonators (RSSR and T-type resonator) instead it models the overall FSS behavior. The new resonance frequencies are f_{z1} and f_{z2}. The transmission zeros at these frequencies and the comparison of the transmission behavior of the FSS is shown in Fig. 4.1.5. The analysis presented in [LS13] shows that a passband around the frequency f_p can be produced between two stopband frequencies f_{z1} and f_{z2}. The dielectric substrate is represented by a transmission line section with characteristic impedance $Z_d = Z_\circ/\sqrt{\varepsilon_r}$, where $Z_\circ = 376.73\,\Omega$. The transmission line has a $\beta l = 2.43^\circ$ at 8 GHz and it can be modelled as a reactive element at resonance frequency. The resonant frequencies are

$$f_z^{rsrr} = \frac{1}{2\pi\sqrt{L_1 C_1}}, f_z^t = \frac{1}{2\pi\sqrt{L_3 C_3}}, \tag{4.1.1}$$

$$f_{z1} = \frac{1}{2\pi}\sqrt{\frac{C_1 + C_2}{C_1 C_2 (L_1 + L_2)}}, \tag{4.1.2}$$

$$f_{z2} = \frac{1}{2\pi}\sqrt{\frac{C_3 + C_4}{C_3 C_4 (L_3 + L_4)}}, \tag{4.1.3}$$

$$f_p = \frac{1}{2\pi\sqrt{(L_{eq} + (L_{t1}/L_{t2}))(C_{t1}/C_{t2})}}. \tag{4.1.4}$$

where $L_{t1} = L_1 L_3 + L_1 L_4 + L_2 L_3 + L_2 L_4$,
$L_{t2} = L_1 + L_2 + L_3 + L_4$,
$C_{t1} = C_1 C_2 C_3 + C_1 C_2 C_4 + C_1 C_3 C_4 + C_2 C_3 C_4$,

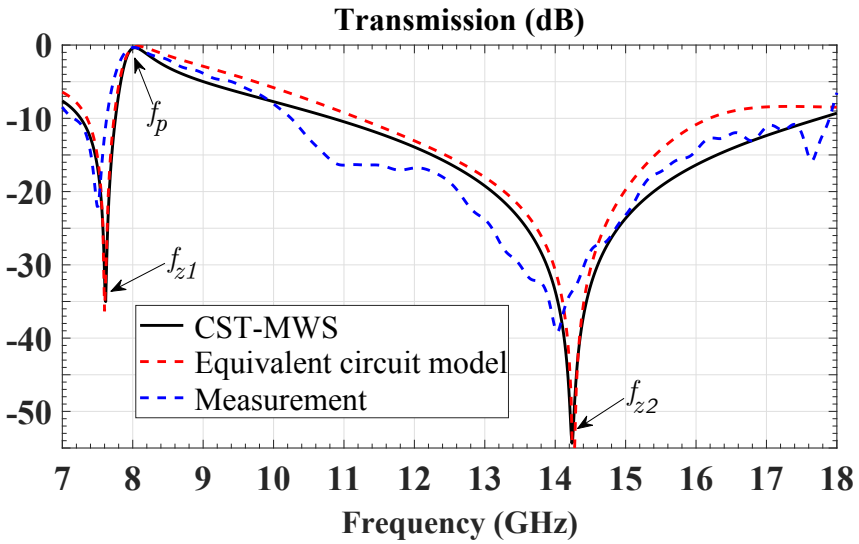

Figure 4.1.5: Transmission behavior of the unit cell structure obtained from CST-MWS, equivalent circuit model and measured experimentally. f_{z1} and f_{z2} indicate the transmission zero due to the RSRR and the T-type resonator, respectively. f_p indicates the passband between the two transmission zeros.

$C_{t2} = C_1C_3 + C_1C_4 + C_2C_3 + C_2C_4$,
and L_{eq} is the equivalent transmission line inductance given by

$$L_{eq} = \frac{Z_d \tan(\beta l)}{\omega}, \tag{4.1.5}$$

where $\beta = \frac{2\pi}{\lambda_g}$.

4.2 Fabrication and measurement setup

The designed structures have been fabricated by using printed circuit board (PCB) technology on a total area of $200 \times 200\,\text{mm}^2$, containing 18×18 unit cells as shown in Fig. 4.2.1(a). Two ultra-wideband dielectric rod antennas with reflector are connected to a Rohde & Schwarz ZVA24 vector network analyzer to measure the behavior of the fabricated FSSs. The input reflection of the used antennas remains below $-10\,\text{dB}$ from 3 GHz up to 20 GHz. The details of the antennas can be found in [BE07]. For the hollow waveguide measurements, standard WR90 waveguides with dimensions $22.86\,\text{mm} \times 10.13\,\text{mm}$ have been used. Fig. 5.2.1 shows the experimental setup for free-space FSS measurements and waveguide filter measurements. The inset of Fig. 4.2.1(b) shows the fabricated samples of the SE unit cell and of the QE unit cell for waveguide filter measurements.

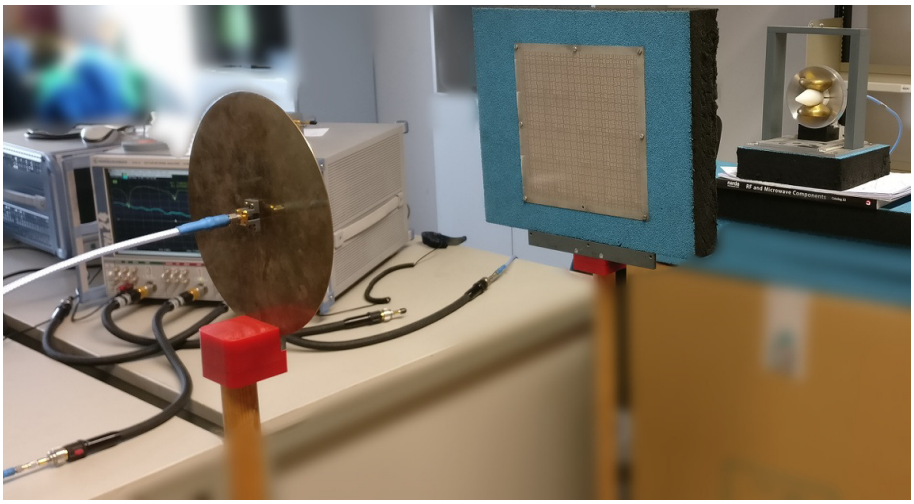

(a)

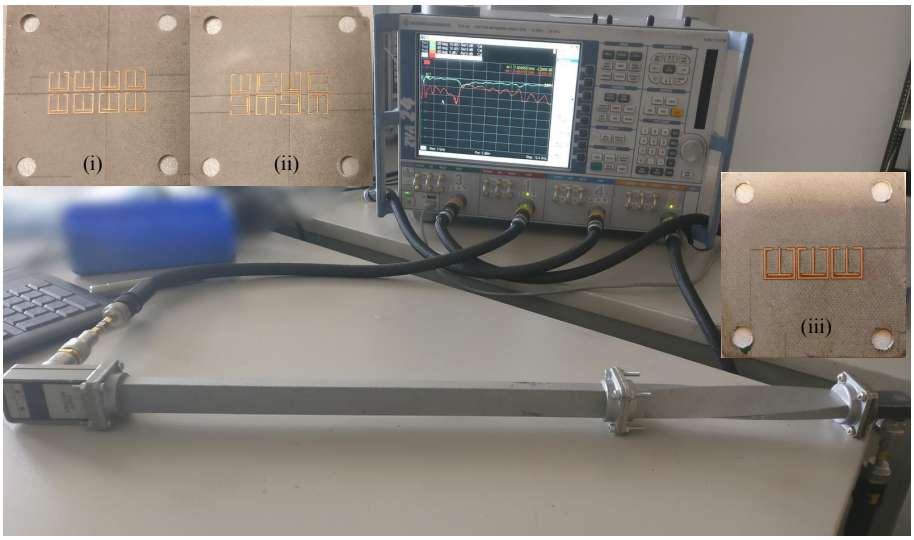

(b)

Figure 4.2.1: Transmission measurement setup for (a) FSS (b) WR90 hollow waveguide, where the subfigures represent (i) SE unit cell configuration (ii) QE unit cell configuration (iii) absorber sample.

The experimental characterization of both FSSs was achieved by a transmission measurement setup as shown in Fig. 4.2.1(a). The transmitting (Tx) antenna and the receiving (Rx) antenna were kept in the farfield of each other. A 96 cm distance between Tx and Rx allowed to approximately satisfy the simulated condition of a plane wavefront for the transmitted wave. Moreover, to remove the effects of ground reflections, the Tx, the Rx and the FSS were aligned at a height of 112 cm above the ground surface. The measurements were performed in the frequency range (7 - 18) GHz with 0 dBm transmit power. The orientation of both the antennas determined the polarization state of the propagating wave. Every FSS measurement was preceded by a reference measurement of the environment. The measured transmission behavior shows good agreement with the simulated results. The differences can be attributed to diffraction at the edges and the

loss characteristics of the material. Due to fabrication limitation a larger sheet size could not be realized.

4.3 Characteristics of frequency selective surfaces

4.3.1 Transmission under normal incidence

To study and analyze the structures as FSS and as filter, its transmission coefficient as a function of frequency at normal incidence for both transverse electric (TE) and transverse magnetic (TM) polarized waves are shown in Fig. 4.3.1. In Fig. 4.3.1(a), the structure with periodic SE unit cells has two resonances for both TE and TM polarization in the considered frequency bands. The resonance frequencies depend on the number of resonators per unit cell. Two resonators with different geometry and type may result in two different resonance frequencies as in the presented case. An additional shift in the resonances is caused by the coupling between these resonators. Geometric parameters such as g and d_3 and reactive elements (L_2, C_2) and (L_4, C_4) influence the resonances due to coupling effects. The stopbands occur at (7.61, 14.24) GHz for TE polarized waves and for TM polarized waves they occur at (11.8, 15.85) GHz. The pass-band for TE polarized waves is at 8 GHz and has a 0.62 GHz bandwidth at −3 dB. The SE unit cell FSS exhibits a relatively sharp roll-off for the first resonance when a TM polarized wave is incident. The structure behaves as an anti-reflective surface for TM polarized waves in a considerably larger band compared to TE polarized waves. At 8 GHz, both polarizations have almost unity transmission. TM polarized waves have a unique pass-band from 12.17 GHz to 14.15 GHz, where the magnitude is greater than −3 dB with a maximum at 12.71 GHz. In this entire pass-band of TM polarized waves, the transmission for TE polarized waves remains below −14.6 dB (at 12.17 GHz) to −41.89 dB (at 14.15 GHz). This means that the structure only permits TM polarized wave transmission and it may be suitable for applications in which the mode of operation is single polarized. At the resonance frequency of 7.61 GHz, the strong electric field is concentrated at the top ends of both vertical arms of the RSRR and the top end of the T-type resonator which is also open. These open ends of the RSRR and the T-type resonator produce strong odd modes at the top end of a unit cell. Moreover, mutual interaction between the periodic elements in lateral direction is not seen while interactions between the unit cells are strong in vertical direction.

In order to eliminate the polarization and incident angle dependency, an isotropic FSS configuration has been developed, which is a periodic QE unit cell structure. The transmission behavior for this FSS is shown in Fig. 4.3.1(b). The structure still has two resonances but shifted because of the change in the geometry of a single element. The stopband resonances for both TE and TM polarized waves are at (7.23, 13.83) GHz. It

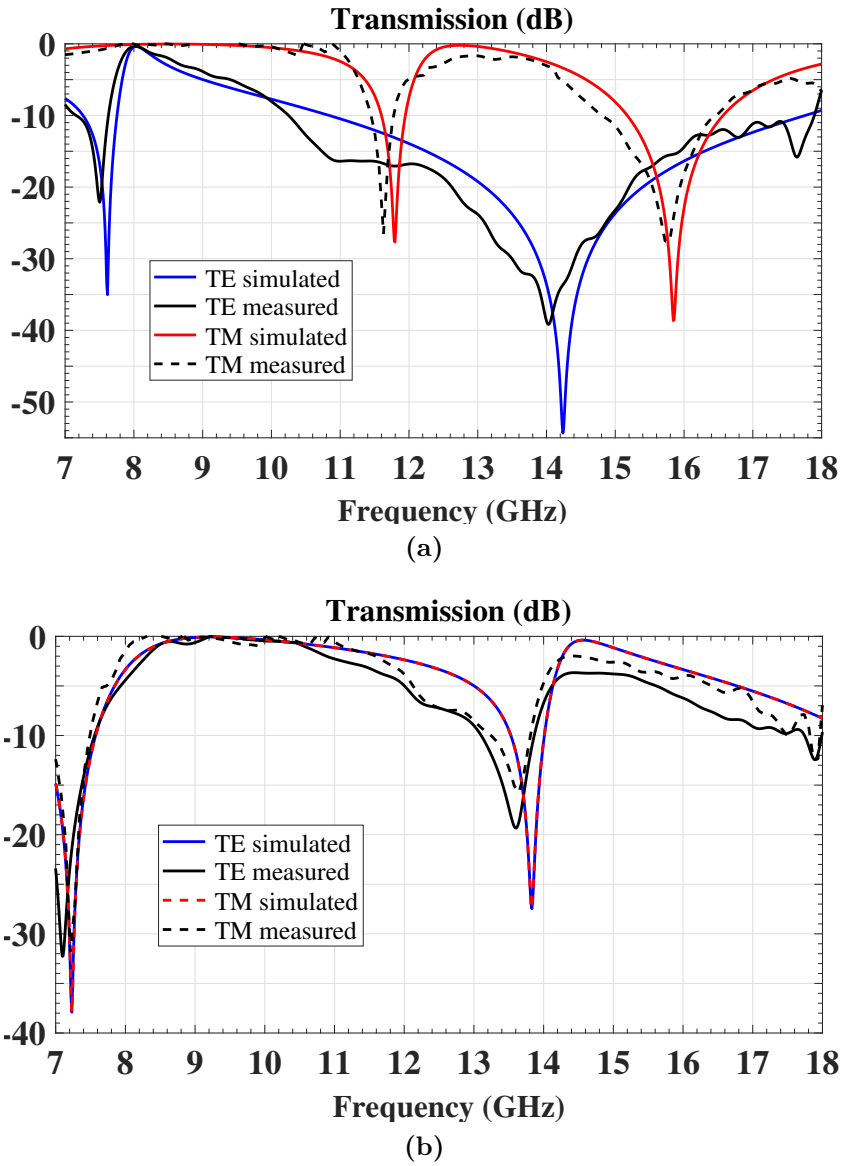

Figure 4.3.1: Transmission coefficient at normal incidence for (a) periodic SE unit cell structure (b) periodic QE unit cell structure, with the dimensions as given in Fig. 4.1.1.

is observed that the transmitted wave experiences less than $-3\,\mathrm{dB}$ attenuation for the entire X-band. The rotational symmetry of the FSS does not differentiate between the polarization of the wave at normal incidence anymore.

4.3.2 Transmission under oblique incidence

The transmission coefficients for the SE unit cell and the QE unit cell at oblique incidence are presented in Fig. 4.3.2 and Fig. 4.3.3, respectively. In Fig. 4.3.2(a), the first resonance at 7.61 GHz and the pass-band around 8 GHz show strong stability with respect to changes in the incident angle till 60°. It is noted that increasing the incident angle

narrows down the pass-band. The reason for such a behavior is the change in the wave impedance as explained in [AJB10]. In Fig. 4.3.2(b), increasing the angle of incidence for TM polarization shifts the resonances to lower frequencies. When the transmission behavior of the periodic QE unit cell structure is observed under different incident angles of a TE polarized wave, it is seen that an additional resonance occurs at 8.96 GHz as shown in Fig. 4.3.3(a). The resonances at (7.23, 13.83) GHz are stable for both polarizations and different incident angles. Fig. 4.3.3(b) displays the TM polarized wave characteristics and it is seen that the structure is fully isotropic (independent of polarization and incident angle). The performance of the QE unit cell structure at large incident angles shows that the first resonance remains stable for both polarizations until 75°. The second resonance

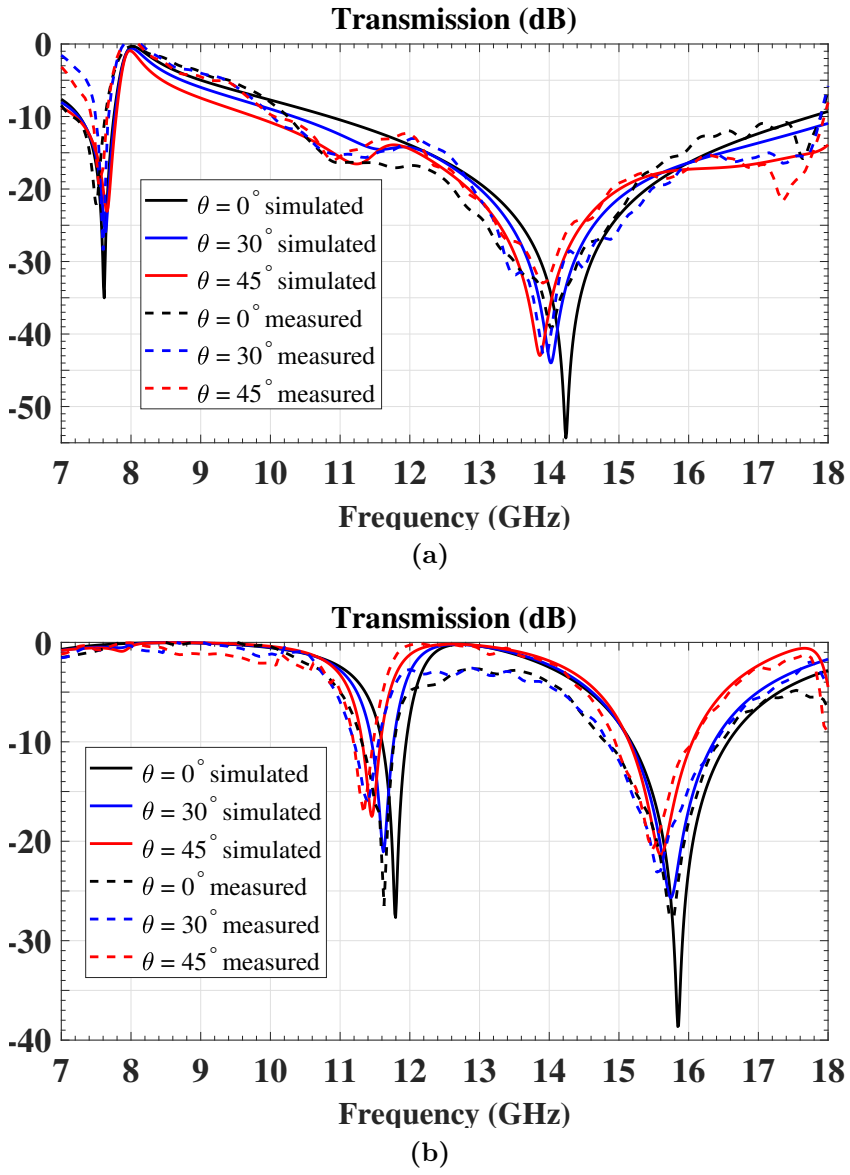

Figure 4.3.2: Transmission coefficient at oblique incidence for periodic SE unit cell structure (a) TE polarization (b) TM polarization.

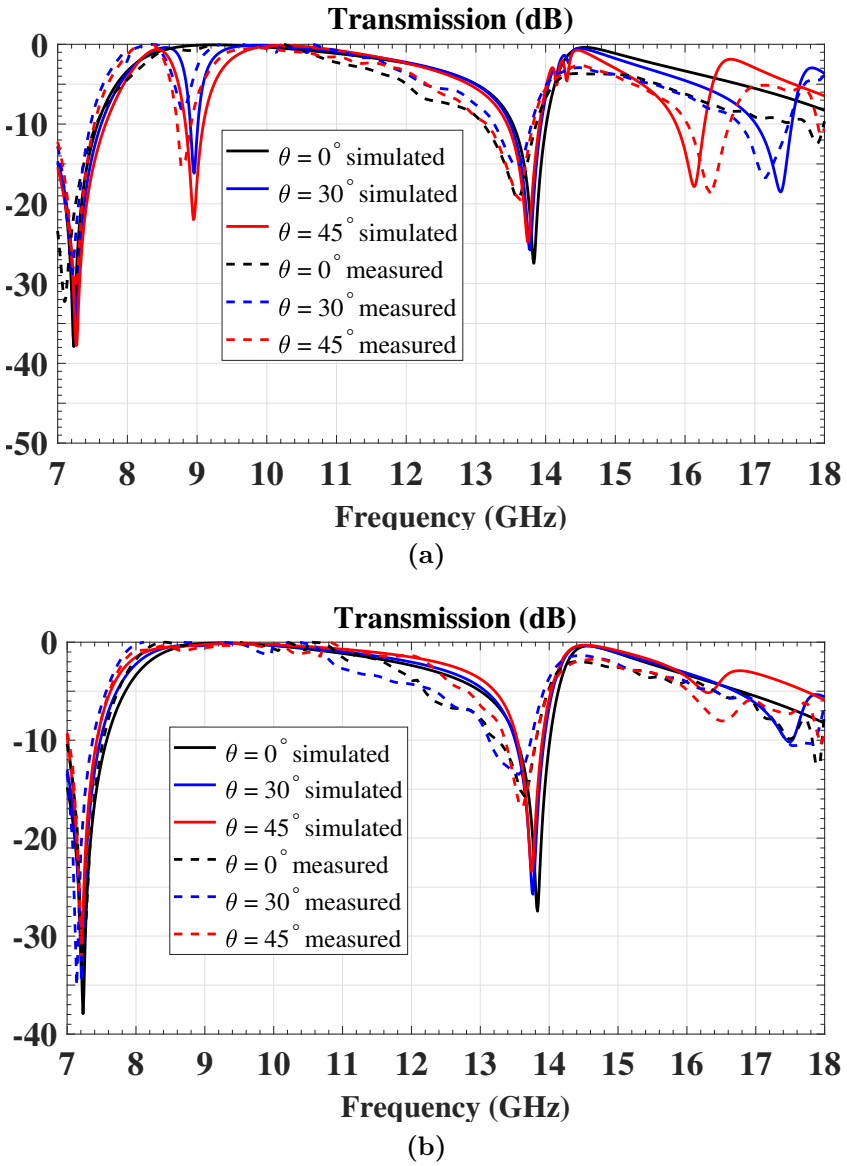

Figure 4.3.3: Transmission coefficient at oblique incidence for periodic QE unit cell structure (a) TE polarization (b) TM polarization.

exhibits a reduction in its magnitude and a slight shift. Measurements for larger angles were not included because of inaccurate results due to the the relatively small effective sheet size.

4.3.3 Insertion loss

Fig. 4.3.4 shows the simulated insertion losses for the normal incidence case for both FSSs. Insertion loss is the ratio of the transmission power when the device under test (DUT), which is the FSS, is not inserted in the system to the transmission power when

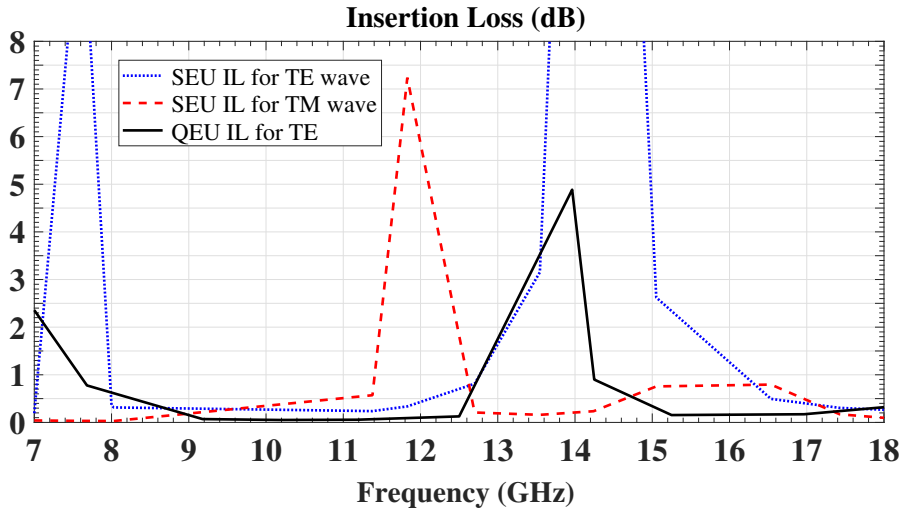

Figure 4.3.4: Insertion loss for periodic SE unit cell structure when incident wave is TE polarized (blue dotted line) and TM polarized (red dashed line) and insertion loss for periodic QE unit cell structure when incident wave is TE polarized.

the DUT is inserted. Insertion loss is computed by ten times log of the ratio of the output power ($P_\circ$) to the input power (P_{in}), $IL = 10 \times \log(\frac{P_\circ}{P_{in}})$. It accounts the losses occurring due to dielectric material (substrate), the copper and due to reflection. It is observed that when a TE polarized wave is incident on the SE unit cell structure, the passband at 8 GHz has very low loss (0.3 dB) and when a TM polarized wave is incident the first passband has less then 0.5 dB IL from 7 GHz till 11 GHz. The QE unit cell structure, which is independent of wave polarization, has 0.1 dB IL in the range (9 - 12.5) GHz and (15.2 - 17) GHz.

4.4 Effect of dimensions on the characteristics

To further investigate the structures and get insight into the transmission behavior, the dimensions of the resonators are changed. The changes in the structural parameters do not have an effect on the symmetry of the structure. The resonance frequencies can be controlled by changing very few parameters.

4.4.1 Tunability of single element unit cell frequency selective surface

The transmission behavior of the periodic SE unit cell structure, when the geometric parameters are varied, is shown in Fig. 4.4.1.In Fig. 4.4.1(a), the gap g is varied from 0.2 mm to 1.5 mm and it is seen that both the resonance frequencies shift to higher values. In other words, the change in g directly affects the coupling between the two types of the resonators in the bottom region of the SE unit cell where the electric field is stronger for both resonators at there resonance frequency. For g =0.2 mm, the first and second resonance occur at 7.61 GHz and 14.24 GHz, respectively, which are shifted to 8.97 GHz and 15.43 GHz, when g=1.5 mm. The tunable bandwidth for the first and second resonance are 1.36 GHz and 1.19 GHz, respectively, for an increase of 1.3 mm in g. Therefore, with the single parameter variation the SE unit cell structure can be tuned in both X-band and Ku-band.

Fig. 4.4.1(b) presents the effect of parameter d_2 on the transmission behavior of the structure. As d_2 decreases from 7.2 mm to 2.2 mm, the resonance frequencies shift to higher values. At $d_2 = 0$, only a single resonance frequency occurs in the entire X and Ku-band at around 10 GHz (not shown here). The first resonance also experiences a decrease in magnitude in addition to the shift. The transmission band becomes wider with a more constant gradient on either side of the band. The second resonance shifts more rapidly with the decrease in d_2. It is because the T-type resonator has a strong contribution in the second resonance.

Fig. 4.4.1(c) shows the effect of parameter d_3 on the transmission behavior of the SE unit cell structure. In addition to the shift in both the resonance frequencies to lower values, the first resonance frequency undergoes an increase in magnitude as well, when d_3 is increased from 0 mm to 2.0 mm. It is also observed that the transmission deteriorates as d_3 decreases from 2.0 mm.

4.4.2 Tunability of quad element unit cell frequency selective surface

The original QE unit cell structure shown in Fig. 4.1.1(b) had resonance frequencies at (7.23, 13.83) GHz. The change in the parameter g and d_5 does not have any effect on the first resonance frequency as seen in Fig. 4.4.2(a) and Fig. 4.4.2(b). When g is varied from 0.2 mm to 1.5 mm the second resonance frequency changes from 13.83 GHz to 16.2 GHz and its magnitude is further decreased. It is observed that the second resonance frequency changes from 13.83 GHz to 16.25 GHz when d_5 is varied from 3.8 mm to 0.8 mm. The tunable bandwidth, when g and d_5 are changed in the specified ranges are 2.37 GHz and 2.42 GHz, respectively, for the second resonance. Moreover, the effect on both the resonance frequencies is seen when d_6 is varied from 0 mm to 1.0 mm. It is seen that,

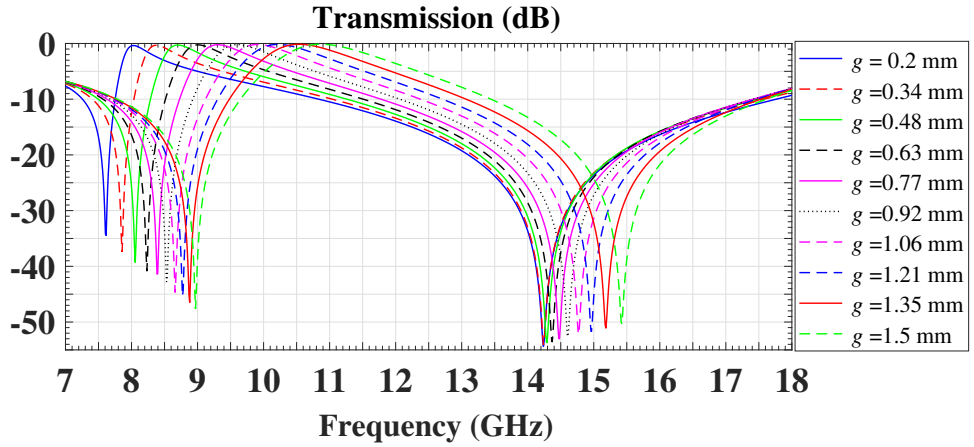

(a)

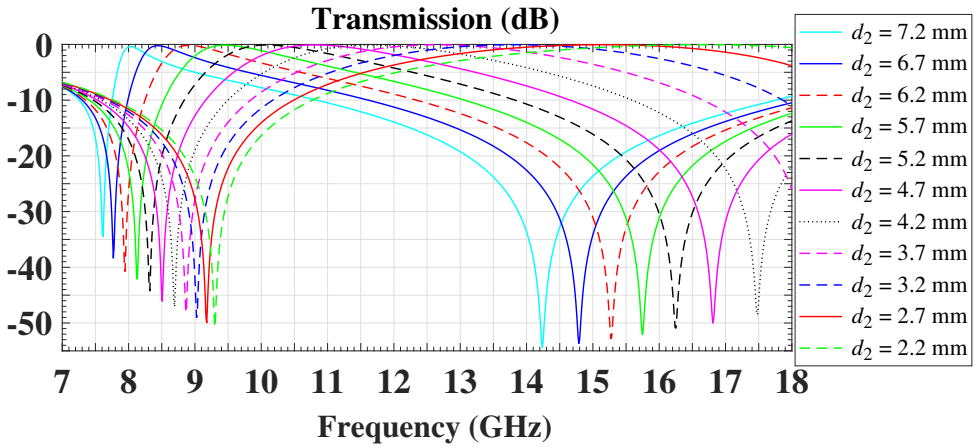

(b)

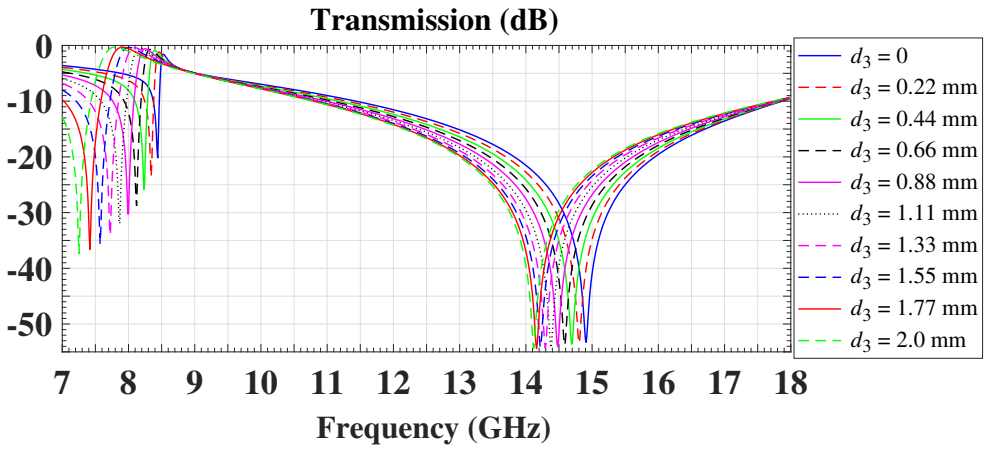

(c)

Figure 4.4.1: Effect of parameters on the transmission behavior of FSS composed of periodic QE unit cell structure for TE polarized incident wave (a) when only g is varied (b) when only d_2 is varied and (c) when only d_3 is varied.

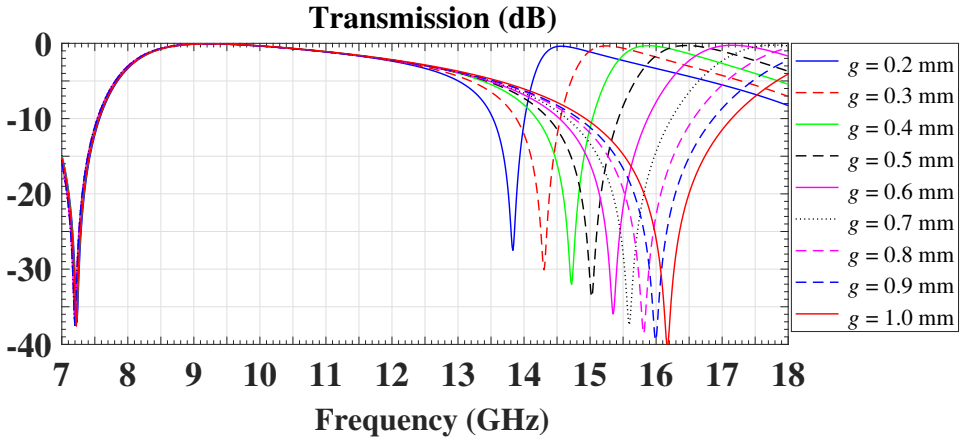

(a)

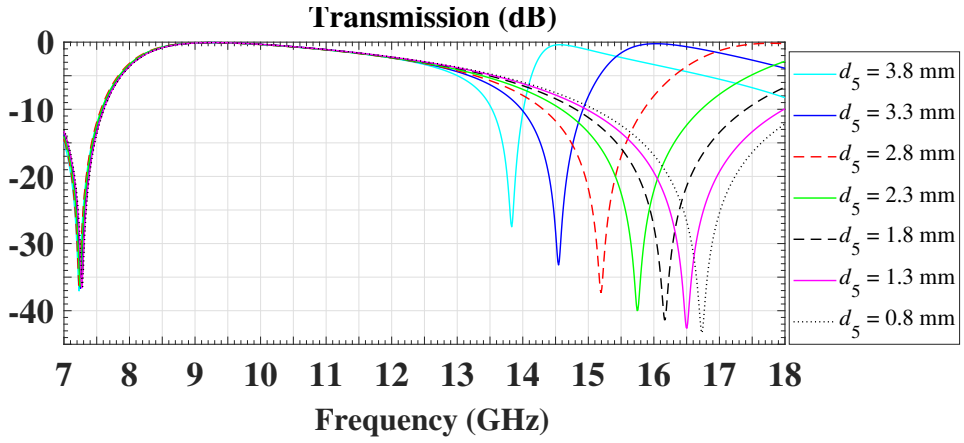

(b)

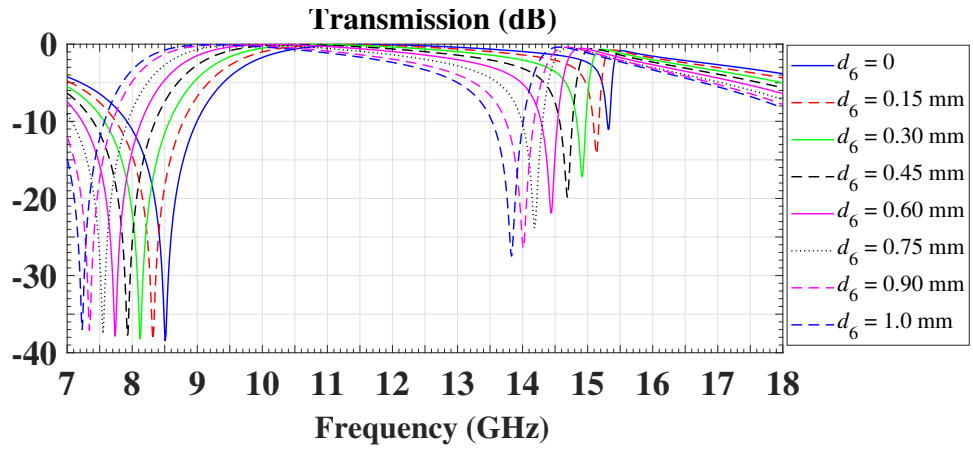

(c)

Figure 4.4.2: Effect of parameters on the transmission behavior of FSS composed of periodic QE unit cell structure for TE polarized incident wave (a) when only g is varied (b) when only d_5 is varied and (c) when only d_6 is varied.

while increasing d_6, the resonance frequencies shift to higher values. The first resonance frequency shifts from 7.23 GHz to 8.5 GHz and the second resonance shifts from 13.83 GHz to 15.3 GHz (the magnitude also increases). The configuration, therefore allows good control over the resonance because of the resonators and exploits the coupling effects that occur between the resonators and the periodic unit cells.

It is also observed that the edge roll-off for the QE unit cell structure can be manipulated with these parameters. For example, in Fig. 4.4.2(c), the lower edge of the second resonance gets steeper with increase in d_6. The steepness can be evaluated by the decay in the transmission magnitude on either side of the resonance frequency to -3 dB, it is denoted by Δ. When $d_6 = 1$ mm the magnitude on the lower edge of the second resonance drops from -27 dB at 13.83 GHz to -3 dB at 12.45 GHz ($\Delta = 1.48$ GHz) while for $d_6 = 0.15$ mm it drops from -14.6 dB at 15.15 GHz to -3 dB at 14.78 GHz ($\Delta = 0.37$ GHz).

4.5 Applications of frequency selective surface

4.5.1 Waveguide Filter

When a waveguide is loaded with the resonators, it exhibits a filtering characteristics. Waveguide filters loaded with simple planar FSSs provide miniaturization, are light weight and low cost solutions. Due to the usefulness of metamaterial loaded waveguide filters in electromagnetic systems, new designs and applications are still proposed [EAA15, HRBR14, CAMP11]. Metamaterial based resonators have been used to operate the waveguides below cut-off frequencies as reported in [HRBR14]. Unlike the conventional waveguides which only support evanescent modes below cut-off, metamaterial resonator loaded waveguides may support negative index propagation due to strong transverse magneto-electric coupling between the fields. The resonator loaded waveguides have also been used for characterizing materials and detecting anomalies in the structures. The dielectric permittivity of different substrates was measured using a resonant FSS placed in a WR90 waveguide [CAMP11]. Due to the importance of such waveguide filters, the planar FSSs developed in previous sections have also been adapted for such applications.

Fig. 4.2.1(b) shows the measurement setup for both configurations of the filter. The complete setup was modeled in CST MWS with open and add space boundary condition in all directions. The modified unit cell geometric parameters for the fabricated structures are $a = b = 5.0$ mm, $d_1 = d_4 = 4.5$ mm, $d_2 = d_5 = 3.6$ mm, $d_3 = d_6 = 1.0$ mm, $g = 0.3$ mm, and $w_1 = w_2 = 0.3$ mm. A WR90 waveguide was used to perform measurements in the frequency range (7 - 12.4) GHz. The X-band hollow waveguide simulated and measured transmission S_{21} and reflection S_{11} for the developed structures are presented in Fig. 4.5.1.

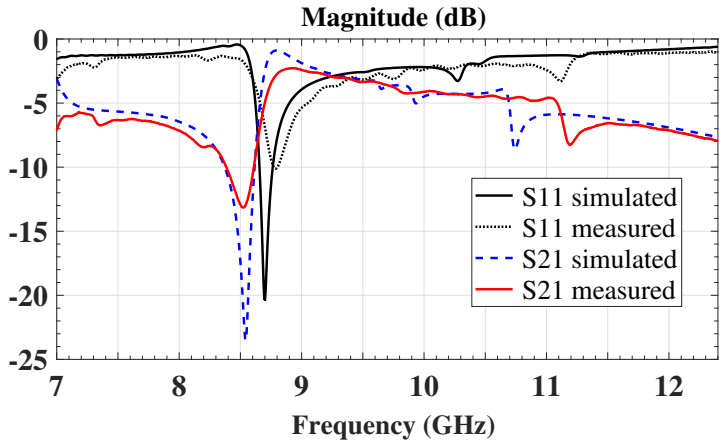

(a)

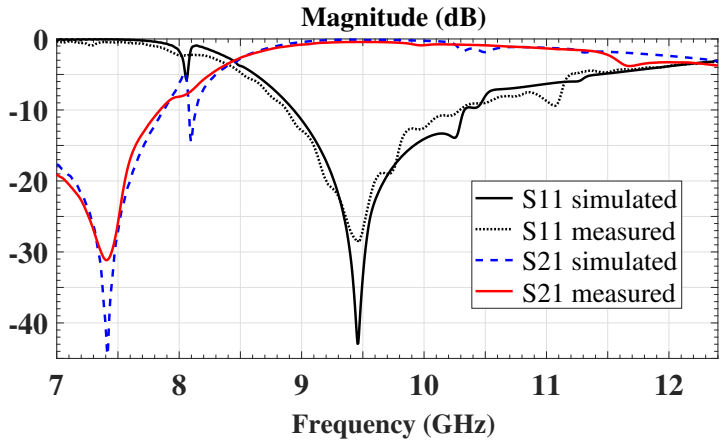

(b)

Figure 4.5.1: Transmission and reflection in waveguide for (a) SE unit cell structure (b) QE unit cell structure.

The through-reflect-line (TRL) technique based on the work presented in [EH79] was used to calibrate the two port network. TRL uses a line with the corresponding characteristic impedance. This replaces the match. FSS unit cells were placed in the center junction. The infinite/periodic unit cell condition was achieved through the metallic walls of the waveguide. The number of resonances with the waveguide boundary condition are the same as with the unit cell boundary condition. The shift in the resonance frequency is evident from the change in the geometric parameters, which has direct effect on the impedance of the resonator. The stopband and a pass-band for the waveguide SE unit cell filter exist at 8.5 GHz and 8.7 GHz, respectively, as shown in Fig. 4.5.1(a). Similarly, the waveguide QE unit cell filter resonates at 9.5 GHz and has a reflection zero at 7.42 GHz, as shown in Fig. 4.5.1(b). The measurement and the simulation results show good agreement.

4.5.2 Unity Absorber

FSS technology based absorbers have advantages over ferrite tiles, carbon nanotubes and pyramidal absorbers because of non-fragility and non-bulkiness [BCL+11, NS71, Mun05]. However, due to their resonant behavior, FSS absorbers have usually limited bandwidth. The specified resonance frequency of narrowband absorbers is also referred to as a tuned frequency. The absorption is achieved by reducing the reflection and transmission as low as possible (ideally $|S_{11}| = |S_{21}| \rightarrow 0$) in the expression for absorption, $A(\omega) = 1 - |S_{11}(\omega)|^2 - |S_{21}(\omega)|^2$. In order to achieve high absorption at a particular resonance frequency, the surface impedance of the structure must match the impedance of the incident medium at that frequency. The complex impedance is a function of frequency and wave propagation constant. Since the incident medium is free space and it has a real impedance, the goal is to have this impedance at the first resonance frequency. This is achieved by manipulating the effective constitutive parameters such that the reflection from the structure is minimized and the wave is fully absorbed. Now, to prevent the wave from being transmitted through the structure, a metal film is used at the backside. Therefore, the periodic SE unit cell structure is modified by placing an additional copper layer at the lower surface of the substrate. It has a thickness of 0.0175 mm and its conductivity is 5.8×10^7 S/m. The absorber design is illustrated in Fig. 4.5.2. Finally, $|S_{11}(\omega)|$ and $|S_{21}(\omega)|$ tend to zero in the absorption expression, $A(\omega) = 1 - \cancelto{0}{|S_{11}(\omega)|^2} - \cancelto{0}{|S_{21}(\omega)|^2}$. The expression for absorption is then simplified to $A(\omega) = 1$. In this thesis only one of the FSSs design configurations has been used to demonstrate the absorption behavior of the structure and due to the simplicity of the measurement, an X-band hollow waveguide has been used for realization. The SE unit cell design is optimized for the intended operating frequency of the absorber. The modified unit cell geometric parameters for the proposed absorber are $a = b = 8.0$ mm,

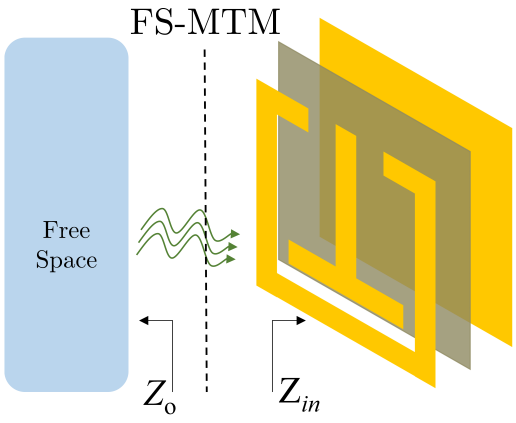

(a)

Figure 4.5.2: Schematic diagram of a planar absorber. For impedance matching at the absorption frequency $Z_\circ = Z_{in}$.

$d_1 = d_4 = 7.0\,\text{mm}$, $d_2 = 5.74\,\text{mm}$, $d_3 = 1.5\,\text{mm}$, $g = 0.26\,\text{mm}$, and $w_1 = 0.5\,\text{mm}$. The two absorption frequencies are 7.82 GHz and 9.65 GHz. Good absorption is achieved at resonance frequencies, where the impedance of the structure becomes $376.7\,\Omega$. It is noted that the resonance frequencies of the absorber are different from those of the FSS, due to the metal backing. Since stopbands are not important for the absorber design, all geometry parameters of the MTM structure can be utilized in order to locate the absorption bands at the desired frequencies. Fig. 4.5.3(a) shows the normalized real and imaginary component of the input impedance. At 7.82 GHz, the complex input impedance $Z_{in} = (1.03 + \text{j}0.03)\,\Omega$. The red dots locate the corresponding values of the real and

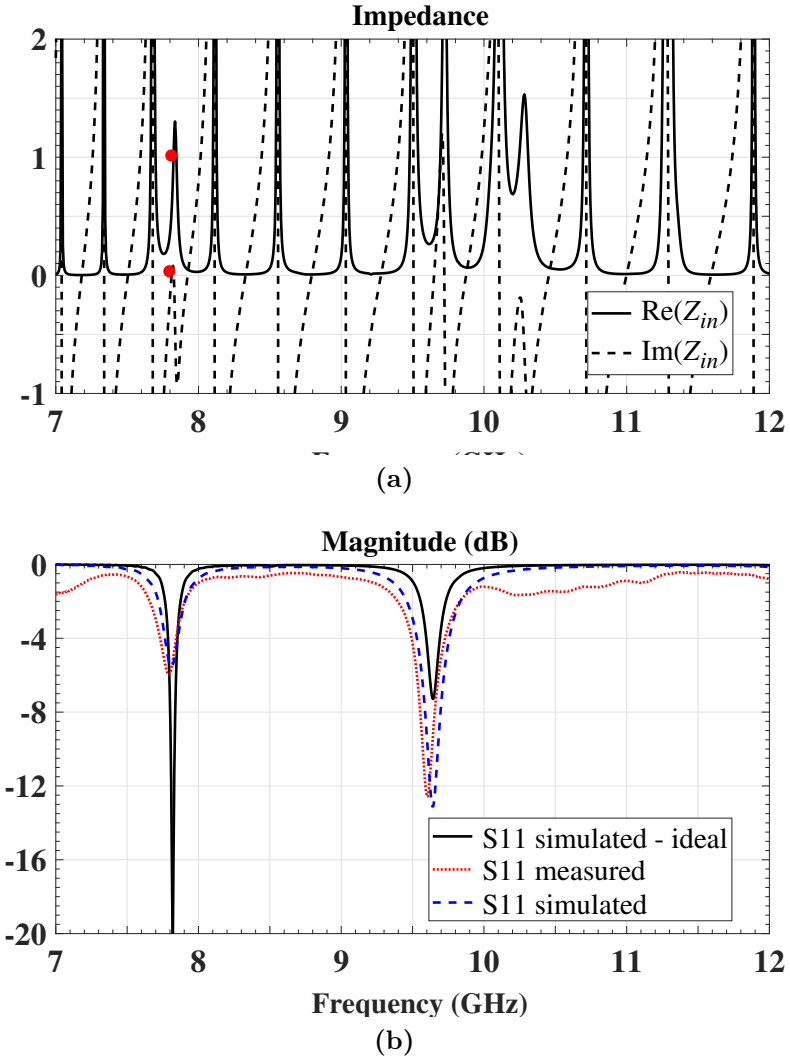

Figure 4.5.3: (a) Periodic SE unit cell structure normalized impedance dependent on frequency. Red dots indicate the impedance matching at the resonance frequency. (b) The simulated (ideal) curve has been obtained for the data sheet material parameters of the substrate with 0.508 mm thickness, but shows deviations to the measured results. The second simulated curve obtained with increased losses agrees well with the measurement results.

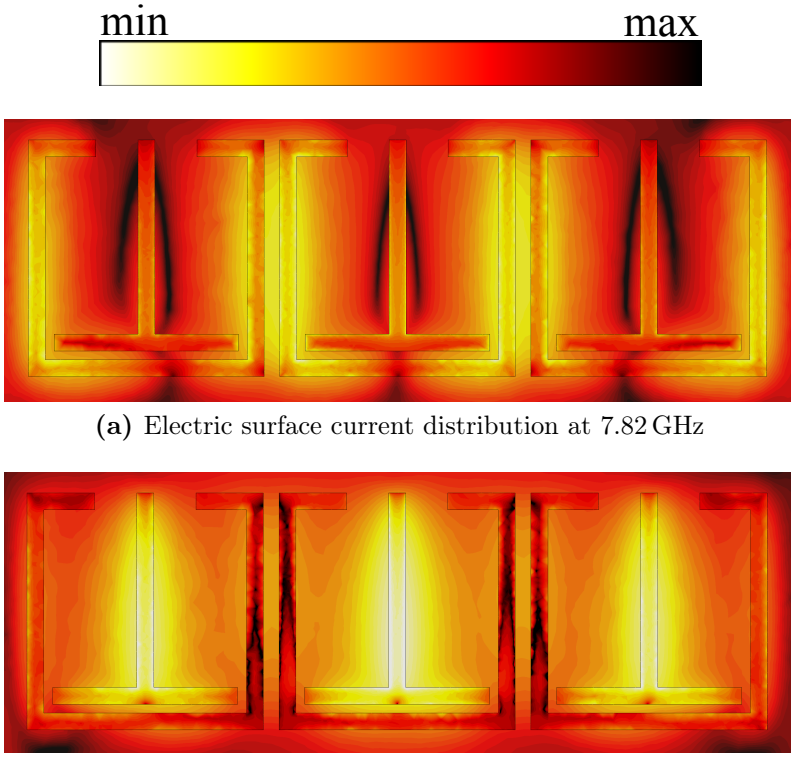

(a) Electric surface current distribution at 7.82 GHz

(b) Electric surface current distribution at 9.65 GHz

Figure 4.5.4: Electric surface current distribution at absorption frequencies for the absorber sample presented in Fig. 4.2.1(b)(iii).

imaginary input impedance components at 7.82 GHz in Fig. 4.5.3(a). It is evident from the input impedance that the structure has a very small reactance value and it is purely resistive at the first resonance frequency.

The reflection coefficient of the structure is shown in Fig. 4.5.3(b) for the absorber presented in Fig. 4.2.1(b). The bandwidth for resonance due to the RSRR and the T-type resonator at -3 dB are 81 MHz and 130.15 MHz, respectively. Hence, the first resonance is more susceptible to the material loss as indicated by the blue dashed line.

The complete waveguide measurement setup was simulated to investigate the difference between the simulation and measurement results. The narrowband resonances, which have high Q-factor are affected by changes in the loss parameter of the dielectric substrate. Therefore, the deviation from the simulated results are associated with the changes in the material characteristics, tangent delta specifically. The effect of change in the material characteristics is modelled in the simulation (Rogers RO4350B with loss tangent 0.02 and relative permittivity $\varepsilon_r = 3.48$). This justifies the deviation of the measurements from the simulated results (indicated by blue dashed line in Fig. 4.5.3(b)). The effect of the loss tangent on both the resonances is found to be different due to different ratios of total energy stored to the loss at the given frequency. Fig. 4.5.4 presents the absolute

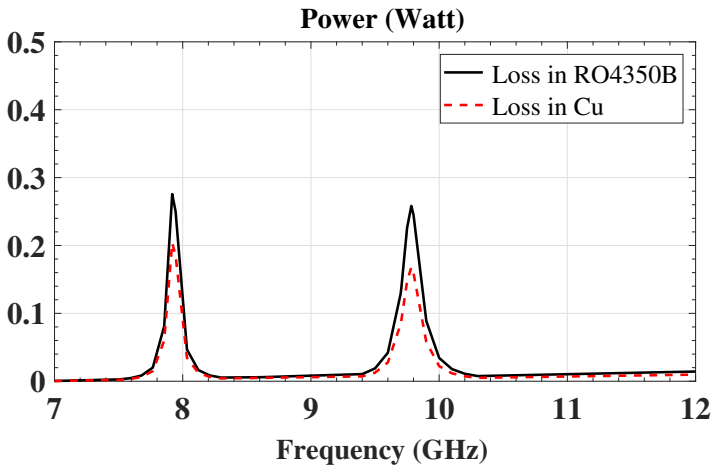

Figure 4.5.5: Power loss per material.

electric surface current distribution of the SE unit cell based absorber at the resonance frequencies. It can be observed that the first absorption peak at 7.82 GHz is contributed by the RSRR and the second absorption peak at 9.65 occurs due to the T-type resonator. The current distribution is concentrated in the vertical arms of both the resonators at the respective resonance frequency. Narrowband absorbers have applications in bio-medicine and for sensors [LZZ15].

Absorber tunability

Using two different types of resonators allows to tune the resonance frequencies and manipulate the mutual interaction between the resonators. The fields generated by the resonators couple with the $\boldsymbol{E}$ and $\boldsymbol{H}$ component of the incident wave and produce strong electromagnetic fields which are attenuated in the dielectric substrate and the metal. The power loss per material is shown in Fig. 4.5.5. It can be seen that most power is lost in the dielectric substrate. It also shows that the loss tangent is a critical factor in the design.

The parameters which control the absorption band are dielectric loss, mutual interactions between the resonators, and geometric parameters of each resonator. The first resonance at 7.82 GHz can be easily positioned by a single parameter l, as shown in Fig. 4.5.6(a). It is observed, when l is increased from 0.6 mm to 2.0 mm, the first resonance shifts to lower frequency from 8.56 GHz to 7.6 GHz, respectively (approximate tunable bandwidth of 1 GHz for less than -3 dB magnitude). For these particular values of the parameter l, the structure is well matched with the incident medium. The matching for both resonances greatly depends on the mutual coupling between the two different resonators. The mutual coupling effect is mainly observed in the gap, at the bottom of the unit cell. The gap can be adjusted for the optimum magnitude of the resonances. To show the effect of the change in the magnitude, the parameter g has been increased from 0.26 mm to 0.6 mm in Fig. 4.5.6(b). Also, it is seen that the resonance due to the

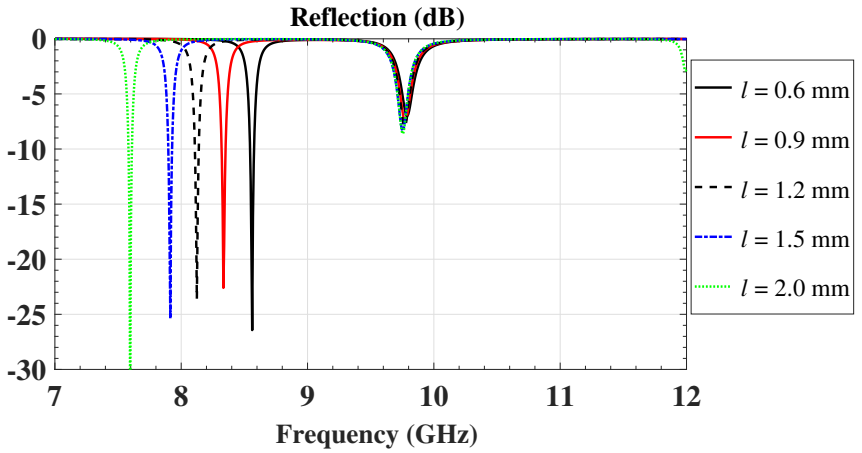

(a)

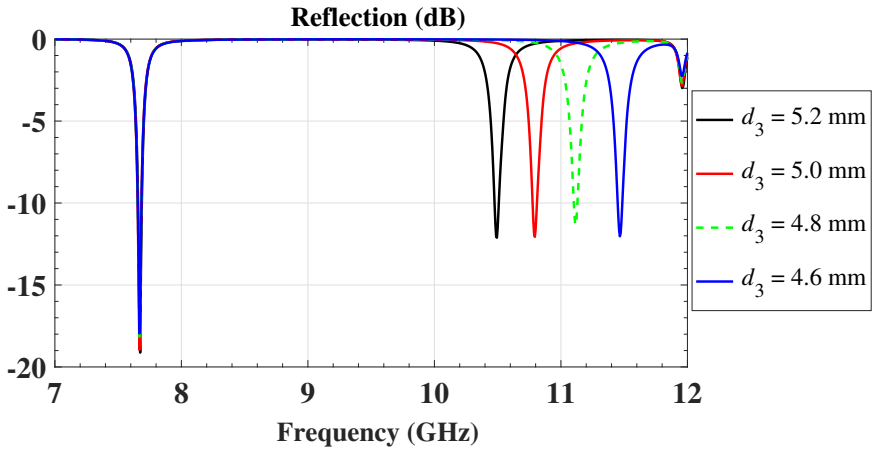

(b)

Figure 4.5.6: Magnitude of the reflection as a function of frequency when parameter (a) l is changed (b) d_3 is changed and the gap between the T-type resonator and the RSRR at the bottom is 0.6 mm.

T-type resonator can be easily tuned by changing parameter d_3. Decreasing d_3 shifts the resonance frequency to higher values.

The effect of variation in the gap at the bottom of the unit cell on the absorption frequencies can be seen in Fig. 4.5.7. g_v affects the magnitudes of both the resonance frequencies and causes frequency shift to the second resonance frequency only, whereas g_l only causes a frequency shift and does not have significant effect on the magnitudes. Changing g means changing the capacitive coupling between the conductors (resonant elements).

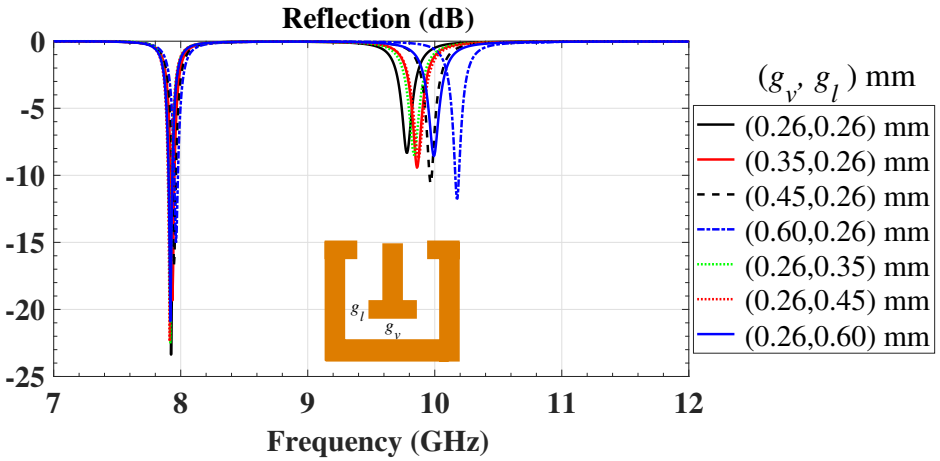

(a)

Figure 4.5.7: Magnitude of the reflection as a function of frequency when parameter g is changed. g_v and g_l represent the verticle gap and the lateral gap at the bottom of the unit cell between the RSRR and T-type resonators.

4.6 Performance Comparison

In Table 5.6.1, a comparison is made with models that have been recently presented in literature. f_u, f_l denote the upper resonance frequency and lower resonance frequency, respectively, of the structures. The dimensions of the unit cells such as length, width, and thickness are represented by l, w and t. The proposed FSS is thin and has a wider band of operation and increased frequency ratio.

Table 4.6.1: Performance comparison of different FSSs

Ref.	**Band**	**Frequency** (GHz) **TE | TM**	**Frequency ratio**($\frac{f_u}{f_l}$)	**Unit cell** ($l \times w \times t$) mm	**Layers**	**Frequency band** (GHz)	**Permittivity** (ε_r)	**Incident angle stability**	**Polarization stability**
[SK15]	pass	3.1	-	$10.4 \times 10.4 \times 0.35$	1	1.5-4.0	4.3	• For TE wave, passband narrows down, stopband widens • For TM wave, passband widens after 30°, stopband narrows down • Resonance frequency unchanged	• stable at normal incidence • inc. angle effects B_w differently for TE and TM
	stop	2.54,3.54	1.39						
[OS17]	pass	-	-	$8 \times 7 \times 1.524$	single layer stacked	3-30	3.0	• For single polarzation, resonance is independent of incident angle	Polarization dependent
	stop	10.5 | -							
[GS17]	pass	5	-	$8.4 \times 8.2 \times 0.8$	1	0-6.5	4.4	• For TE wave, resonance frequency does not change but the passband between resonance goes to under -10dB. Resonance gradient decreases • For TM wave, resonaces are more stable, gets narrower with increase in incident angle and magnitude decreases	Polarization independent
	stop	2.35,3.05	1.29						
SE unit cell FSS	pass	8 | 8,12.7	-,1.58	$10 \times 10 \times 0.27$	1	7-18	3.48	• For TE and TM wave, slight shift in the resonance frequency observed • Passbands are independent of incident angle for both polarization	Polarization dependent
	stop	7.6,14.24 | 11.8,15.85	1.87,1.34						
QE unit cell FSS	pass	9.0,14.5	1.61	$5 \times 5 \times 0.27$	1	7-18	3.48	• For both polarization, resonances are independent of incident angle • Passband shows good incident angle stability	Polarization independent
	stop	7.23,13.83	1.91						

4.7 Summary

A frequency selective surface composed of two different types of metamaterial resonators was discussed for X- and Ku-band. Its equivalent circuit model was presented, which depicts the topology of a dual band-stop microwave filter. The metamaterial unit cell design was modified to construct an isotropic FSS, independent of incident angle and angle of polarization. The presented design offers miniaturization, polarization independent behavior, good incident angular stability, suppressed harmonics, and less than 0.5 dB insertion loss. The simulated and measured results are in agreement. Applications of the designs were demonstrated as hollow waveguide filters and perfect absorbers. The effect of geometric parameters on the performance of the frequency selective surface were also discussed. It was observed that the designs provide freedom to control the resonances with only few parameters.

CHAPTER 5

Miniaturized Polarization Selective Surface

Single layer FSS designs have been explored as waveguide filter and microwave absorption applications in Chapter 4. In this chapter, the structure is re-designed by introducing geometric asymmetries. The multiple resonators based design is used to exploit the mutual coupling of the structure to achieve a strong cross-polarized microwave transmission and a highly-selective polarization conversion. The design is investigated with respect to the following features: 1) The mutual interaction between the two distinct resonators in a unit cell and other resonators in the array configuration provides freedom to control the resonance frequency and the ellipticity with very few parameters. 2) In dual band behavior, when a linearly polarized wave is incident on the metasheet a strong cross-polarized transmitted wave is obtained in one band and a circularly polarized transmitted wave is created in the other band with high polarization conversion efficiency. The contents of this chapter have been widely taken from our work published in [KE19a].

In Section 5.1, the basic principles and analytical expressions associated with the design are briefly revised with some additional insight. Also, the geometry and parameters of the polarizer design are presented. The simulation and measurement procedures, and challenges are discussed in Section 5.2. The characteristics of the polarizer in transmit-mode when a linearly polarized wave is impinging on its surface, and parameters that determine the performance of a polarizer are discussed in Section 5.3. It also presents the analysis of the electric fields and electric surface current distribution in detail followed by

the effects of the mutual coupling on the ellipticity and the substrate loss on the transmission coefficient in Section 5.4 and Section 5.5, respectively. In the end a comparison is presented with other polarizer designs in Section 5.6.

5.1 Design methodology

5.1.1 Principles and performance parameters

Metamaterial (MTM) based polarization selective surfaces (PSSs) are composed of subwavelength resonating elements to form a unit cell. The unit cells are arranged periodically to form a metasheet. The mutual coupling among the resonating elements in the metasheet, if controlled, allow to achieve the desired electromagnetic characteristics. The proposed design uses an anisotropic structure and the constitutive relations are given by [LSTV94]

$$\boldsymbol{D} = \varepsilon_\circ \varepsilon_r \boldsymbol{E} - \frac{j\kappa}{c}\boldsymbol{H}, \tag{5.1.1}$$

$$\boldsymbol{B} = \mu_\circ \mu_r \boldsymbol{H} + \frac{j\kappa}{c}\boldsymbol{E}, \tag{5.1.2}$$

where κ describes the strength of cross-coupling between magnetic and electric field and is known as *chirality*. The speed of light in free-space is denoted by c. When a linearly polarized wave is incident on such a structure then the circularly polarized transmitted waves are given as

$$\boldsymbol{E}^{\pm}(z) = \frac{1}{2}E_\circ(\hat{x} \mp j\hat{y})e^{-jkz}, \tag{5.1.3}$$

where $\boldsymbol{E}^+$ and $\boldsymbol{E}^-$ represent the right hand circularly polarized (RHCP) wave and the left hand circularly polarized (LHCP) wave, repectively. In the above expression, the direction of propagation is in $+z$-direction and the index of refraction for such a wave is given by $n_\pm = n \pm \kappa$. Consider a y-polarized incident wave (E_y^i) which propagates through this structure. The transmitted wave will have two orthogonal linear components, T_{yy} and T_{xy} (where the first subscript and the second subscript indicate the polarization of the transmitted wave and the incident wave, respectively). The transmission coefficients for circularly polarized waves can be obtained from linear transmission coefficients $T^\pm = 1/\sqrt{2}\,(T_{yy} \pm jT_{xy})$. The performance of the polarization converter can be evaluated by the ellipticity η (it measures the circular dichroism and characterizes the polarization state of the transmitted wave), the polarization extinction ratio PER (it measures the difference between the magnitude of the RHCP and the LHCP waves) [CWCG16], the

polarization conversion ratio PCR (it measures the polarization conversion of an LP incident wave to the transmitted cross- and co-component),

$$\eta = \arctan\left(\frac{|T^+| - |T^-|}{|T^+| + |T^-|}\right) = 0.5 \arcsin\left(\frac{|T^+|^2 - |T^-|^2}{|T^+|^2 + |T^-|^2}\right), \tag{5.1.4}$$

$$\text{PER} = 20 \log_{10}(|T_{+x(y)}|/|T_{-x(y)}|), \tag{5.1.5}$$

$$\text{PCR}_{yy} = \frac{|T_{yy}|^2}{|T_{yy}|^2 + |T_{xy}|^2}, \tag{5.1.6}$$

$$\text{PCR}_{xy} = \frac{|T_{xy}|^2}{|T_{yy}|^2 + |T_{xy}|^2}. \tag{5.1.7}$$

The wave is circularly polarized when $\eta = \pm 45^\circ$, linearly polarized when $\eta = 0^\circ$, and for all other values of η the wave is elliptically polarized. Positive values of η indicate the right-hand sense of rotation of the transmitted wave and negative values of η indicate the left-hand sense of rotation. Large values of PER means high polarization conversion efficiency.

High polarization conversion efficiency is achieved when either $|T^+|$ or $|T^-|$ is zero. This means that the magnitude of the transmitted wave components $|T_{yy}|$ ($|T_{xx}|$) and $|T_{xy}|$ ($|T_{yx}|$) must be equal and their phase difference should be -90° or 90° for a RHCP or a LHCP wave, respectively.

5.1.2 Polarizer Design

The unit cell of the developed design consists of two distinct metamaterial resonators, a rectangular split ring resonator (RSRR) and a T-type resonator. First, the unit cell is rotated by 90° clockwise to create a C4 symmetric 2×2 supercell. Each unit cell of the super cell in the bottom layer is rotated by 90° with respect to the corresponding unit cell in the top layer. The structure now forms a chiral geometry and it is three dimensional nonsysmmetric. It is pertinent to mention here that the chirality only affects the polarization state of the propagating wave according to eq. (2.5.33). Chiral geometries obey fixed relations for certain symmetries. For example, the LP transmission coefficients for the C4 sysmmetric structures are $T_{xx}^{f(b)} = T_{yy}^{f(b)}$ and $T_{yx}^{f(b)} = -T_{xy}^{f(b)}$ (where the superscript f represents a wave propagating in $-z$-direction and the superscript b represents a wave propagating in z-direction) when the incident wave is linearly polarized. Second, the right diagonal resonating elements in the supercell are scaled 0.5 times the left diagonal resonating elements (all the parameters are scaled except w, which is the same for all the elements) as shown in Fig. 5.1.1(a). The structure is designed as C4 nonsymmetric in order to increase the cross-polarization conversion. As a result, the LP

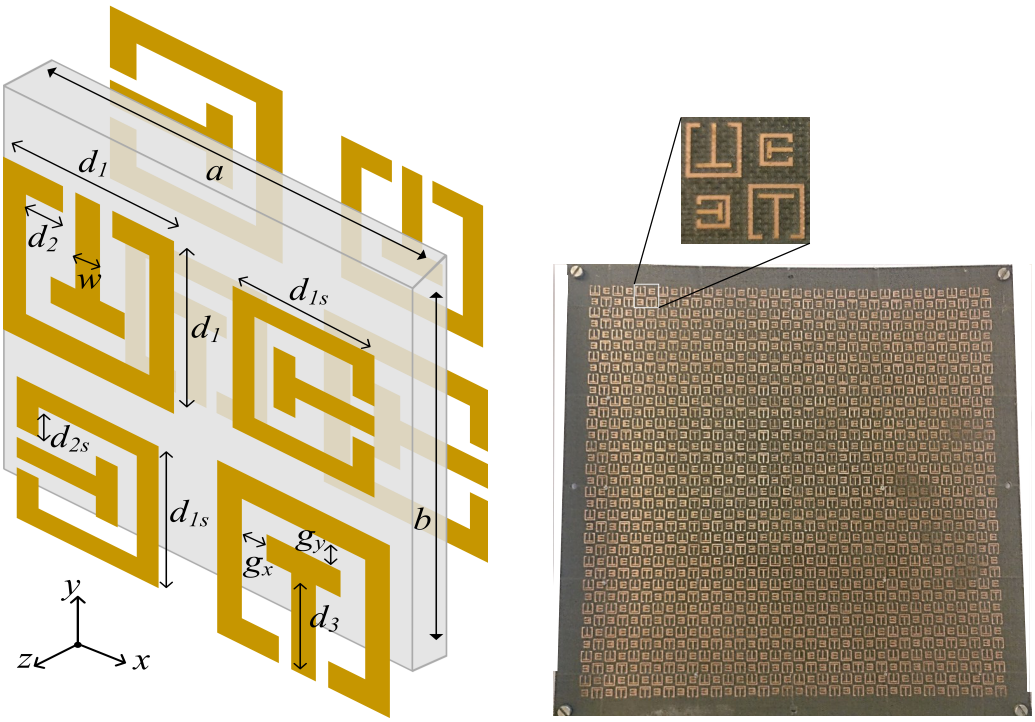

(a) (b)

Figure 5.1.1: Polarization selective surface (a) proposed supercell where $a = b = 10\,\text{mm}$, $d_1 = 4.5\,\text{mm}$, $d_2 = 0.75\,\text{mm}$, $d_3 = 3.3\,\text{mm}$, $d_{1s} = 0.5 \times d_1 = 2.7\,\text{mm}$, $d_{2s} = 0.5 \times d_2 = 0.375\,\text{mm}$, $w = 0.4\,\text{mm}$, and $g_x = g_y = 0.4\,\text{mm}$ (b) fabricated sheet.

transmission coefficients for the C4 nonsysmmetric structures become $T_{xx}^{f(b)} = T_{yy}^{f(b)}$ and $T_{yx}^{f(b)} \neq T_{xy}^{f(b)} = T_{xy}^{b(f)}$. Since each layer responds differently to orthogonal components of the incident electric field, the desired phase difference can be achieved. The interlayer coupling is affected by the thickness of the dielectric substrate. If the thickness is zero, the missing symmetry in z-direction will vanish resulting in no chirality and when the thickness is too large coupling will be too weak.

5.2 Fabrication and measurement setup

The unit cell array of the PSS was fabricated in-house using a ProtoLaser S, which uses a laser to structure the copper layers. The structuring of the copper layers on both sides of the thin substrate is a challenging task because of high temperature the substrate is deformed or damaged and it becomes structurally instable. Therefore, Rogers DiClad 880 with a thicker dielectric substrate was used to manufacture the design. The substrate has a relative permittivity $\varepsilon_r = 2.2$, a loss tangent of 0.0009 (from datasheet) and a thickness

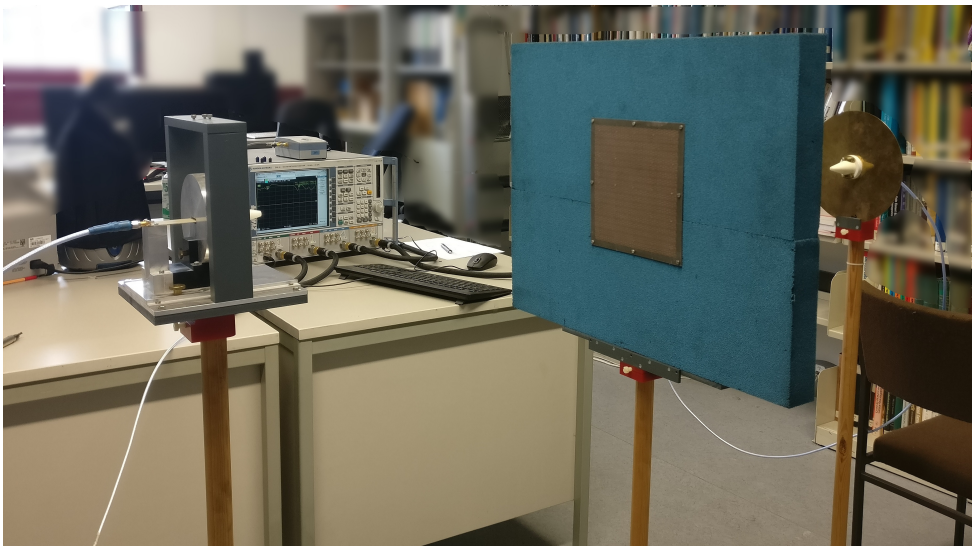

Figure 5.2.1: Polarization selective surface free-space measurement setup.

of 1.524 mm. It is made from woven fibreglass. Fig. 5.1.1(b) shows the fabricated sample. The fabricated sheet consists of 18×18 supercells. The average size of the unit cell is $\lambda_g/4$ and of the supercell it is $\lambda_g/2$ (λ_g corresponds to the resonance frequency 14.79 GHz).

The planar PSS has been designed in CST Microwave Studio with periodic boundary conditions in (x, y)-direction and Floquet ports in z-direction [CSTom]. A linearly polarized plane wave is incident on the structure and the orthogonal linear vector components of the transmitted wave are computed on the other side of the structure to study the propagation behavior.

For the purpose of measurements, the free-space setup shown in Fig. 5.2.1 was used. It can be seen that the metasheet is placed in an absorber frame in order to reduce the reflected waves back to the antennas. The transmission measurements were performed using two linearly polarized dipole excited ultrawideband dielectric rod antennas with a reflector [BE07] that are connected to the Rohde & Schwarz ZVA24 vector network analyzer using coaxial cables. The polarization state of the antenna is changed by physically rotating the antenna orientation on the transmission side of the metasheet. First, the transmission (S_{21}) measurement is performed without the metasheet through the hollow absorber. This measurement is recorded and taken as a reference for the successive measurement with the metasheet placed in the absorber frame. Furthermore, time gating is applied to further filter out the undesirable responses such as multiple reflections. However, it is known that the sharp changes in frequency domain result in a broadband time-domain response. Therefore, in the process of filtering reflections one may filter out useful information and lowering of the amplitude may be observed in systems where the frequency domain response is a narrowband. It means that the time gate window must be carefully chosen.

5.3 Characteristics of the polarization selective surface

5.3.1 Linear to circular polarization transmission

The magnitude of the orthogonal components of the transmission coefficient for $E_y^i(-z)$ at normal incidence as a function of frequency are shown in Fig. 5.3.1(a). The first and second null of the co-component of the transmission coefficient magnitude ($|T_{yy}|$), represented by the black through line, occur at 7.6 GHz and 9.15 GHz, respectively. These resonances are the combined effect (resonance and mutual interactions) of the left diagonal elements on both layers. The resonance at 14.6 GHz is predominantly due to

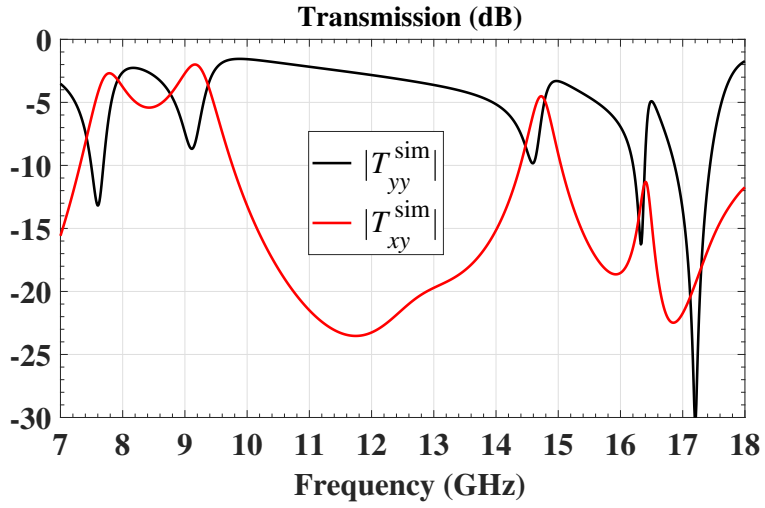

(a)

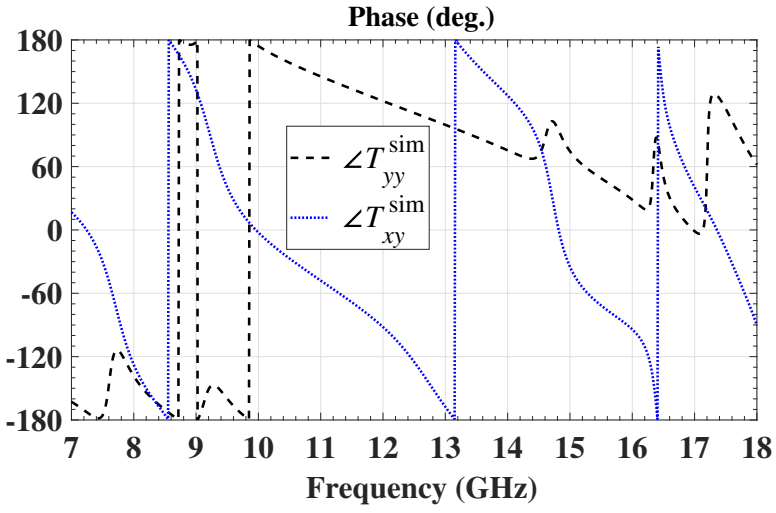

(b)

Figure 5.3.1: (a) Magnitude and (b) phase of cross- and co- components of the transmission coefficient.

the combined effect of the right diagonal elements on both layers. Consequently, a strong cross-component (red through line) of the transmission coefficient ($|T_{xy}|$) is observed at these frequencies. It is further seen that the magnitudes of both components are identical at 14.79 GHz. The difference between the phases of orthogonal components determines the polarization type of the transmitted wave. The phase of the transmission coefficient for each component is shown in Fig. 5.3.1(b). The phase of co-component and cross-component at 14.79 GHz is 97.78° and 8.39°, respectively, yielding a phase difference of $\Delta\phi = \angle T_{xy} - \angle T_{yy} = -89.39°$. Thus, a circularly polarized wave is created on the transmission side of the PSS at 14.79 GHz and a strong cross-component with a magnitude as high as −2 dB at 9.15 GHz.

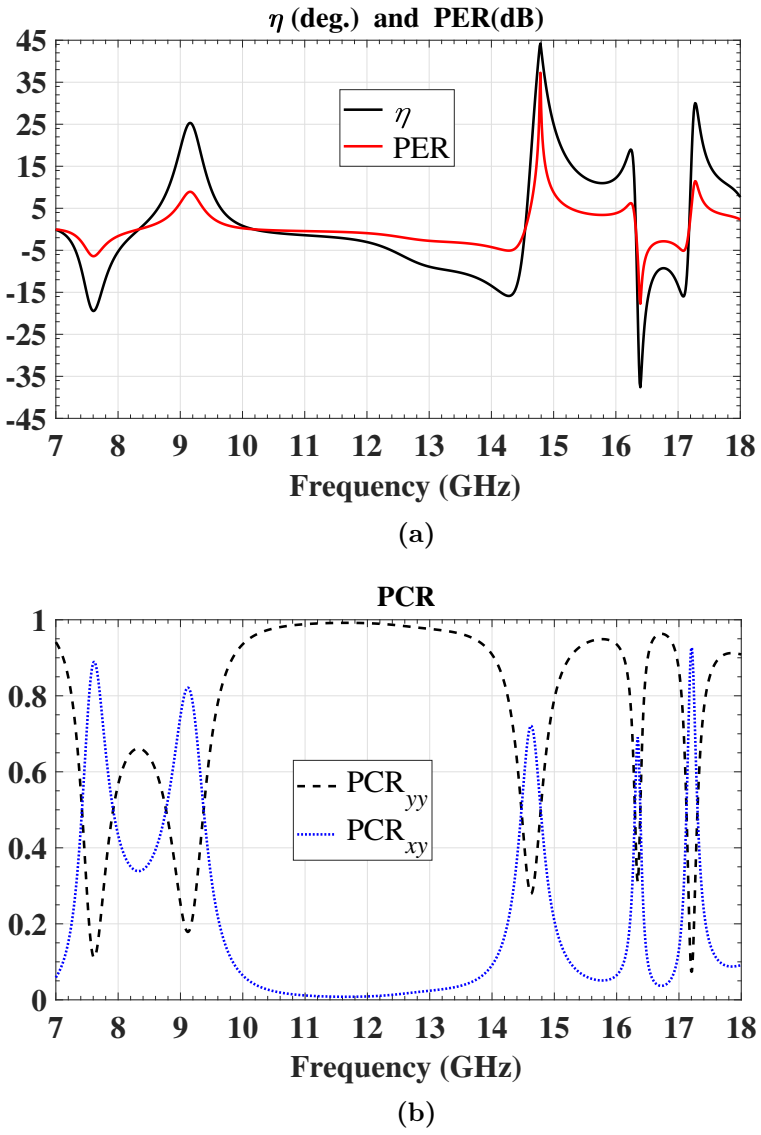

Figure 5.3.2: Simulated performance indicators for PSS. (a) Ellipticity and polarization extinction ratio. (b) Polarization conversion ratio of cross- and co-components of the transmission coefficient.

5.3.2 Performance indicators

In Fig. 5.3.2, the performance parameters defined in eqs. (5.1.4) - (5.1.7) are plotted. It can be seen in Fig. 5.3.2(a) that the peak value of the ellipticity η is 44.3° at 14.79 GHz, which means that the transmitted wave is circularly polarized at this frequency. Furthermore, the value of η at 9.15 GHz is 25.2°, which represents the elliptical polarization. Other peak values of η correspond to transmission magnitudes lower than −10 dB, hence they are not considered. An additional functionality of the proposed PSS is demonstrated by the PER and PCR. The PER shows that the magnitude of the RHCP wave is greater than the LHCP wave at 9.15 GHz and 14.79 GHz by a margin of 8.83 dB and 37.30 dB, respectively. This implies that the transmitted wave is RHCP (with respect to the $-z$-direction) at 14.79 GHz. The magnitude of the orthogonal components that constitute the RHCP wave show the PSS conversion efficiency. It can be observed that the structure polarization conversion ratio PCR is 0.5 for $|T_{yy}|$ and $|T_{xy}|$ at 14.79 GHz. Fig. 5.3.2(b) also shows that the transmitted wave has a $y-$polarized dominant component between 10 GHz to 13 GHz.

5.3.3 Analysis of field and current distributions

The polarization conversion behavior of the proposed structure can be understood by analyzing the field and the surface current distributions. At resonances, high cross-polarization transmission or polarization conversion are the consequence of longitudinal dipole-dipole coupling and transverse (interlayer) coupling. The superposition of the modes produced due to magnetic dipoles and electric dipoles can be expressed by eigenmodes of the resonator. Fig. 5.3.3 illustrates the surface current plot over the $z-$component of the electric field at different resonance frequencies. At 14.79 GHz, in the top layer, a longitudinal electric dipole mode is observed in each of the two RSRR elements on the left diagonal with weak coupling within the supercell and strong coupling with the elements in the neighbouring supercells. A magnetic dipole mode is observed in the right diagonal elements due to the small size of the elements and alignment of the gaps along the incident electric field vector ($y-$axis). The loop current and charge distribution (strong E_z on the T-type resonator) can been seen in Fig. 5.3.3(a). In addition, coupling due to parallel and antiparallel currents within the unit cell can be interpreted accordingly. The bottom layer for this frequency is shown in Fig. 5.3.3(b). The currents for the left diagonal elements are reversed. In the case of the right diagonal elements, the currents in the outer loop remain the same on the top layer and on the bottom layer, which indicates parallel magnetic dipole coupling. The direction of the currents on the bottom layer distinguishes the rotation direction and determines the RHCP or the LHCP type of the transmitted wave. The parallel currents on both layers at 14.79 GHz indicate that the transmitted wave is RHCP. At 16.4 GHz, the currents on the top layer are almost the same as for 14.79 GHz,

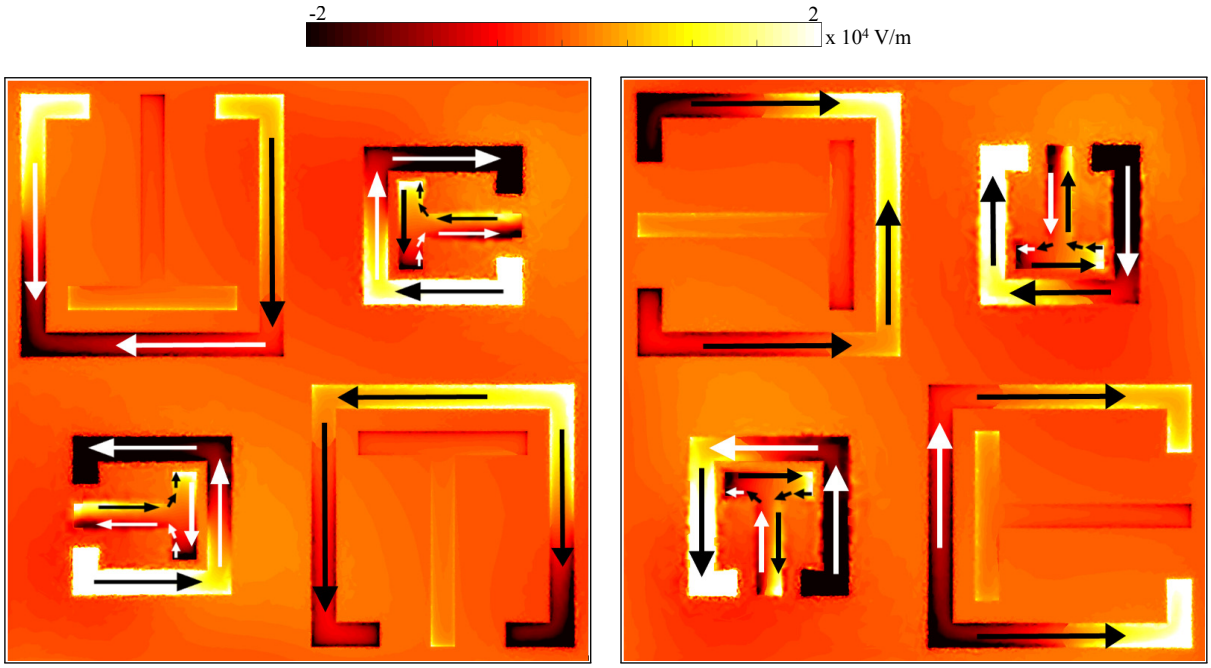

(a) Top layer (f = 14.79 GHz) **(b)** Bottom layer (f = 14.79 GHz)

Figure 5.3.3: Symbolic electric surface current distribution (black or white arrows) over electric field component E_z (color scale), which is related to surface charge, at different frequencies.

especially on the right diagonal elements, as shown in Fig. 5.3.4(a). Fig. 5.3.4(b) shows that the currents are antiparallel (opposite in direction) on the right diagonal elements of the bottom layer with respect to the top layer, resulting in a LHCP wave. The lateral coupling in the gaps between an RSRR and a T-type resonator within the unit cell affects the resonance frequency (the parameters (g_x, d_2), as shown in Fig. 5.1.1(a), can be used to change the gap size). At 9.15 GHz, strong cross-polarization conversion is observed. Field distributions inside the structure are twisted as a result of the antiparallel current flow as shown in Fig. 5.3.4(c) and Fig. 5.3.4(d).

5.3.4 Transmitted electric field orientation

The polarization states of the transmitted wave for a $y-$polarized incident wave are illustrated in Fig. 5.3.5. In general the transmitted waves have elliptical polarization except at the resonance frequency, where the transmitted wave is circularly polarized. When the major axis of the ellipse rotates with respect to the polarization of the incident wave, the angle of rotation is called polarization azimuth angle and it is defined as

$$\theta = \frac{[arg(T^+) - arg(T^-)]}{2}. \tag{5.3.1}$$

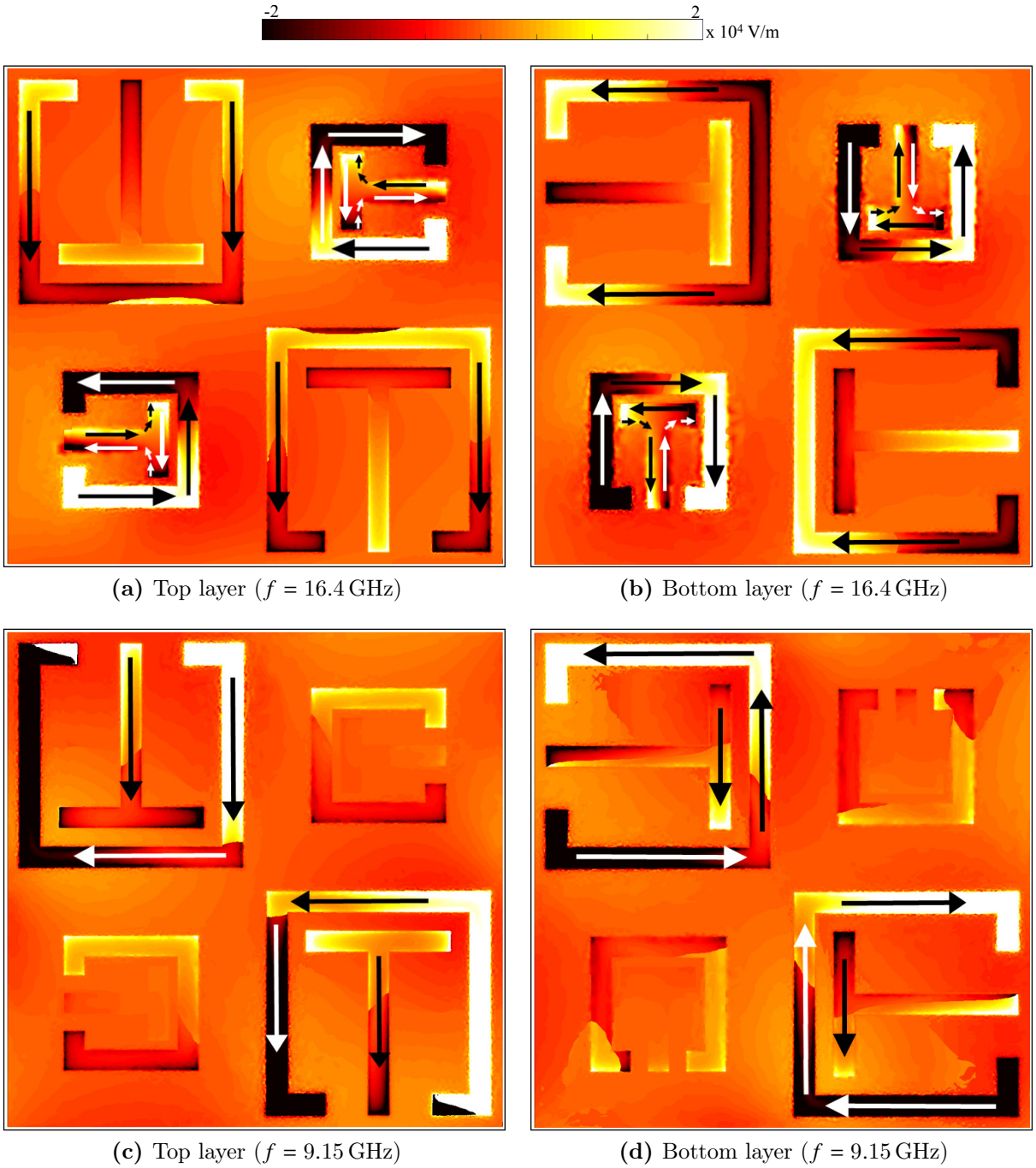

(a) Top layer (f = 16.4 GHz)

(b) Bottom layer (f = 16.4 GHz)

(c) Top layer (f = 9.15 GHz)

(d) Bottom layer (f = 9.15 GHz)

Figure 5.3.4: Symbolic electric surface current distribution (black or white arrows) over electric field component E_z (color scale), which is related to surface charge, at different frequencies.

Due to a strong cross polarized component, the transmitted wave is elliptical at low frequencies as shown in Fig. 5.3.5(a) and 5.3.5(b). The weak cross polarized component between 10 GHz and 13 GHz results in a very thin ellipse as depicted in Fig. 5.3.5(c). Additionally, small rotation is observed in this region. Strong resonances and mutual

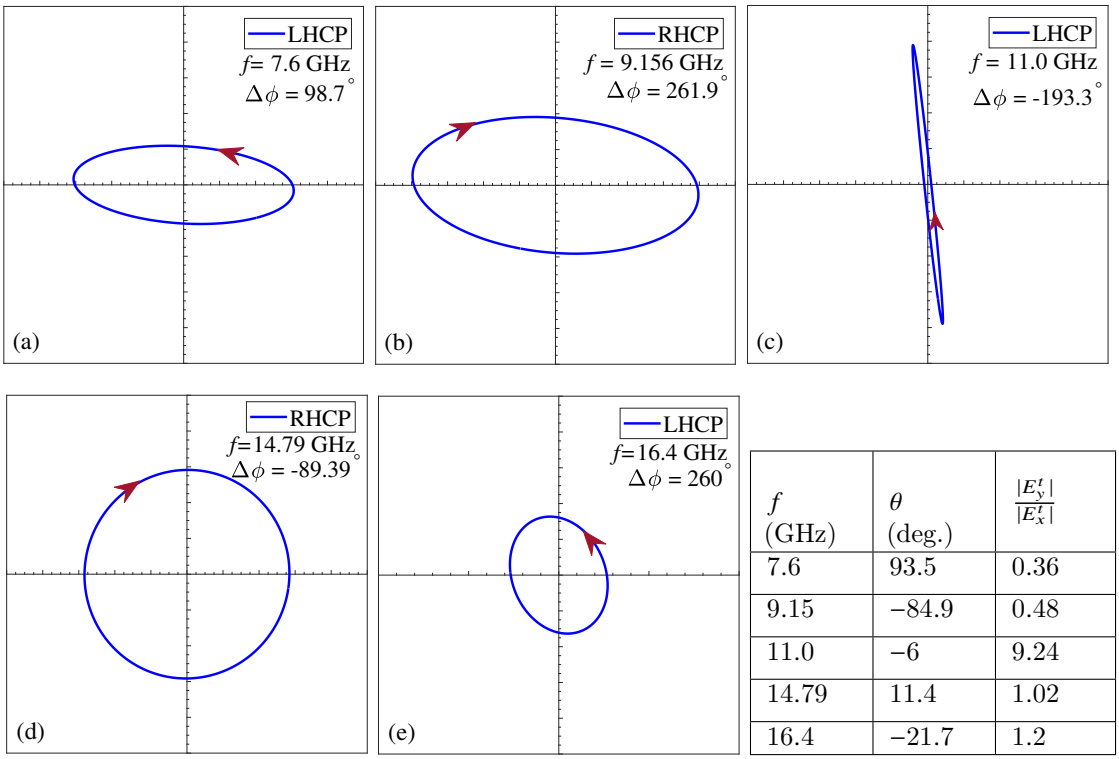

f (GHz)	θ (deg.)	$\frac{\lvert E_y^t \rvert}{\lvert E_x^t \rvert}$
7.6	93.5	0.36
9.15	−84.9	0.48
11.0	−6	9.24
14.79	11.4	1.02
16.4	−21.7	1.2

Figure 5.3.5: Electric field trace of the transmission coefficient when the incident wave is LP. The arrow indicates the direction of rotation in time. The major axis makes (a) 93.5° (b) −84.9° (c) −6° (d) 11.4° (e) −21.7° with respect to the y-axis. Positive and negative sign of θ represent the clockwise and the counter-clockwise sense of polarization azimuth angle rotation, respectively.

interactions at 14.79 GHz and 16.4 GHz in both layers cause the $n\pi/2$ phase difference and equal magnitudes, hence the RHCP and the LHCP waves are created as shown in Fig. 5.3.5(d) and 5.3.5(e). The table in Fig. 5.3.5 shows the polarization azimuth angle in degrees and the ratio between the amplitudes of the orthogonal components of the transmitted wave for the corresponding frequencies.

5.4 Effects of mutual coupling

It is clear that in resonant structures the incident electromagnetic wave causes strong electric fields in the gaps and strong magnetic fields around the electric currents in metallic strips. This interaction between metasheet and electromagnetic wave along with the mutual coupling between the resonators within the unit cell is responsible for the overall behavior of the FSS. Therefore, the two controlling factors are the geometry

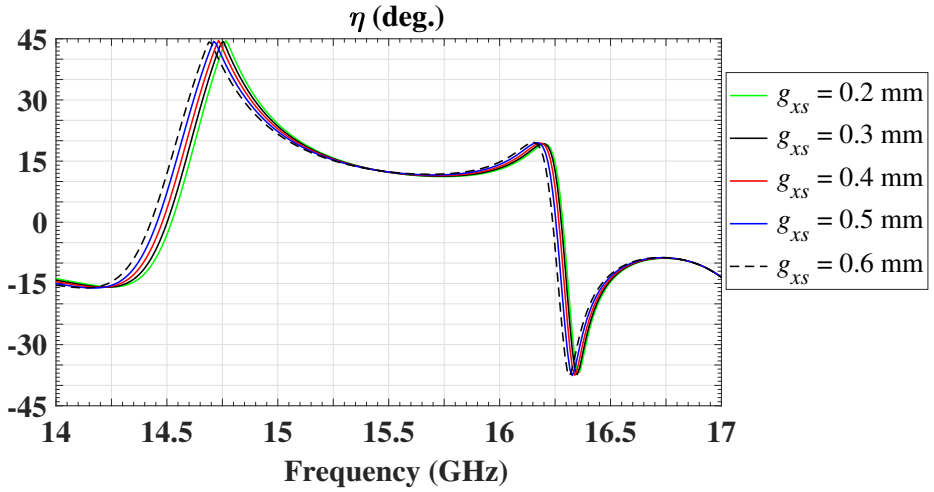

(a)

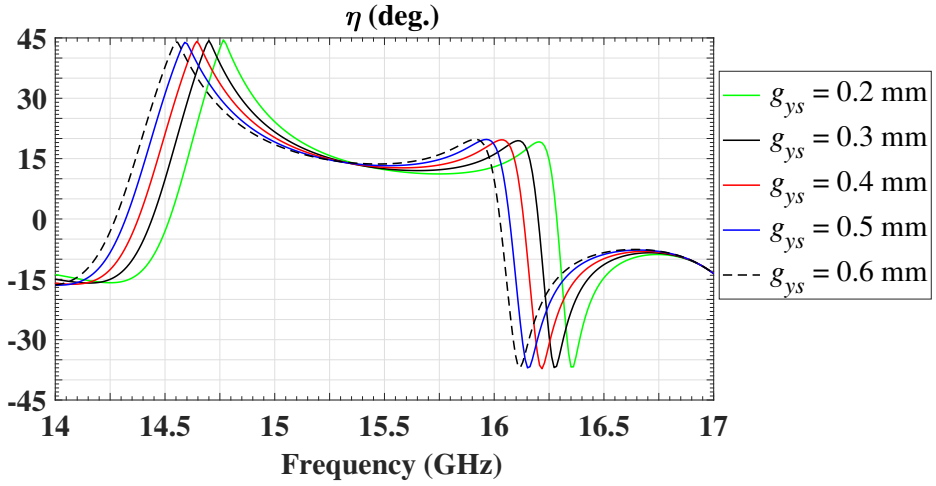

(b)

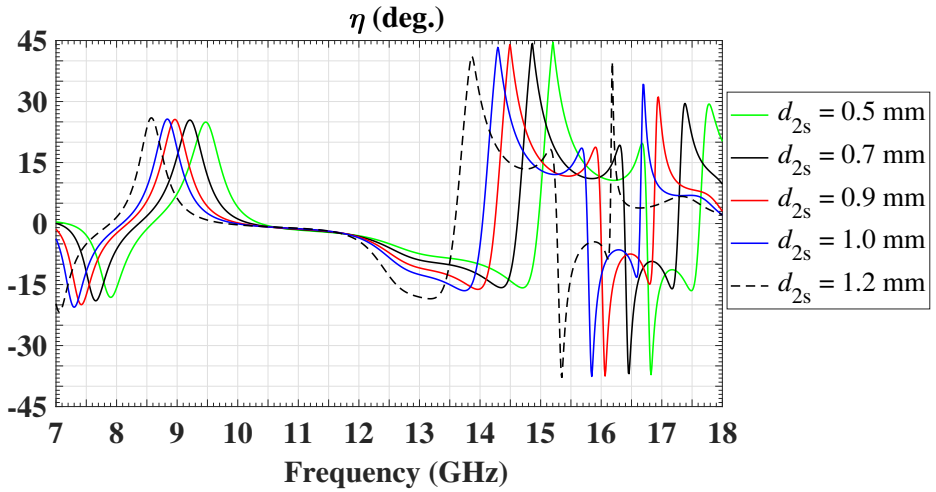

(c)

Figure 5.4.1: Effect of parameters on the transmission behavior and the resonance frequencies. Ellipticity as a function of frequency when only (a) g_{xs} is varied, (b) g_{ys} is varied, and (c) d_2 is varied in millimeters.

of the elements in a unit cell and the spacing between the elements. A multi-resonators based approach is used to create small capacitive gaps within a unit cell, which can provide tunability by changing the coupling between the elements. In particular, a T-type resonator was chosen because it is center connected, behaves like an electric dipole for parallel electric field incidence, and it does not affect the inter-element spacing in an array formed by the RSRRs. At its edges/corners, the T-type structure establishes three regions of strong coupling (g_x, g_y, and the gap at the top of the unit cell) with the RSRR, which allows to control the resonance frequency with very few parameters. This is demonstrated in Fig. 5.4.1. In Fig. 5.4.1(a), g_{xs} represents the lateral gaps between the RSRR and the T-type resonator at the bottom of the unit cells for the elements located on the right diagonal in a supercell. As seen from the electric surface current distribution, the right diagonal elements predominantly contribute to the second resonance and produce an RHCP wave. When g_{xs} is changed from 0.2 mm to 0.6 mm, the resonance frequency shifts to lower frequencies. The tunable bandwidth is 88 MHz for only 0.5 mm change and the ellipticity remains at above 44°. The lower resonance frequency remains unchanged and is hence not shown. Similarly, g_{ys} represents the vertical gap between the RSRR and the T-type resonator for the right diagonal elements. In Fig. 5.4.1(b), it can be seen that when g_{ys} changes from 0.2 mm to 0.6 mm the resonance frequency shifts to lower values. The tunable bandwidth in this range is 230 MHz where the ellipticity is above 44°. Fig. 5.4.1(c) shows the effect on both resonance frequencies when d_{2s} is changed. Increasing d_{2s}, shifts the resonance frequency to lower values and does not affect the magnitude of the ellipticity significantly. The tunable bandwidth is 1.35 GHz when d_{2s} changes from 0.5 mm to 1.2 mm. In resonant structures, the effective permittivity and permeability change very sharply around the resonance frequency. This means that a small change in the frequency results in a significant change in permittivity and permeability (this concept is often exploited in sensors).

5.5 Effect of substrate loss

The simulated PSS was realized for an experimental demonstration. The results are shown in Fig. 5.4.2. The resonance frequencies from the simulation and the measurement are in good agreement but a decline in magnitude was observed in measurements particularly for the co-polarized component. Also, it is observed that the material loss effects the resonances differently at low frequencies than at high frequencies. This magnitude reduction is caused by the losses of the substrate. It is known that the performance of the polarization converter is greatly affected by slight changes in the dielectric losses [FGBV17]. Therefore, a comparison is shown for better understanding of the behavior.

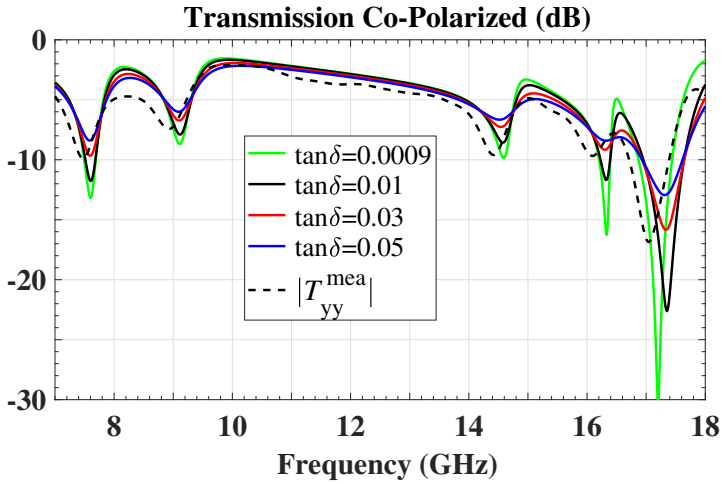

(a)

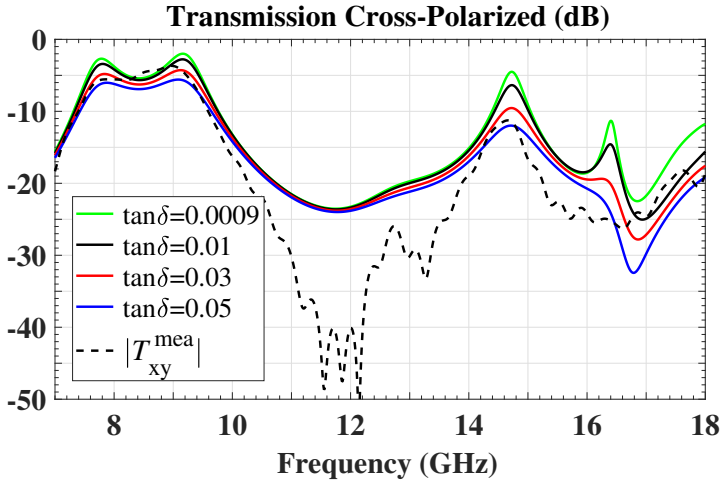

(b)

Figure 5.4.2: Transmitted orthogonal components obtained with measurement setup shown in Fig. 5.2.1.

5.6 Performance comparison

In Table 5.6.1, a comparison with some previously presented designs is made based on the key performance parameters. The design of the present work shows improvements in ellipticity and PER, but has a larger thickness compared to some of the references mentioned. However, the thickness can be further reduced by using a suitable substrate. In [ZQM+18], the thickness of the unit cell is the same as in the presented design but the period of the unit cell is 13 mm while the period of the presented unit cell is 5 mm and the supercell is 10 mm.

* for the values of $t_{+y} = -3.5$ dB and $t_{-y} = -12.0$ dB taken from Fig. 3(b)
*1 at 7.0 GHz, *2 taken from Fig. 5(a), *3 taken from Fig. 7(a)

Table 5.6.1: Performance comparison of different polarization converters

Ref.	Thickness (λ_0)	PER (dB)	η (deg.)	No. of layers
[CWCG16]	0.027	26.1	42.17°	3
[AB16]	0.18	N/A	N/A	6
[CJS+16]	0.036	N/A	~ 36.0°	2
[Wu14]	0.024	< 10	~ 24.4°*	2
[CNCG14]	0.034	21.1	~ 41.0°	2
[ZQM+18]	0.035*1	~ 37.0*2 & ~ 24.0*3	N/A	2
[ZCZ+18]	0.053	N/A	N/A	3
[WXZ+19]	0.176	< 12	N/A	3D
present work	0.035*1 & λ_g = 0.077	37.3	44.4°	2

5.7 Summary

The design and analysis of an asymmetric polarization selective surface design based on metamaterial resonators of different kind was presented. Strong cross polarization rotation and conversion has been observed, which is as high as -2 dB and -4.5 dB at 9.15 GHz and 14.79 GHz, respectively. The surface current distribution and surface charges were used to illustrate the twisting and coupling effects. This further helps in distinguishing the RHCP and the LHCP waves. The results were validated experimentally. The design offers miniaturization, excellent polarization conversion efficiency and resonance control.

CHAPTER 6

Metmaterial Based Energy Harvesters

The investigation, design, and realization of advanced energy harvester solutions with high efficiencies and low power handling capabilities is discussed in this chapter. A particular focus of the work is on dual-band functionalities, which support the realization of smart sensor node concepts within widely distributed sensor networks. The energy harvester solution is based on meta-screens consisting of very specific tightly-coupled rectangular split-ring resonators (RSRRs) and T-type resonators, which have already been discussed in previous chapters as frequency selective surface and polarization selective surface. The contents of this chapter have been widely taken from our work published in [KE17b], [KE18] and [KE19b].

Section 6.1 introduces the essential energy resources that have been in the past used. It provides background on wireless sensor networks and wireless power transmission and how they can be combined to address power management issues of wireless sensor network nodes, followed by some literature and similar studies in Section 6.2. Section 6.3 presents the building blocks of the microwave energy harvester and discusses the challenges in designing an efficient harvester. The design and performance analysis of a dual-band microwave energy harvester and a single-band microwave energy harvester are presented in Section 6.4 and Section 6.5, respectively.

6.1 Introduction

6.1.1 Need for alternative sources of energy

The three major sources of energy, on which humans have been relying, are fossil fuels, nuclear energy and solar energy. Fossil fuels, which include coal, natural gas, oil etc. have been sufficiently utilized over a long period of time. The fossil fuel reserves are finite and sole dependence on the production of energy from fossil fuels can lead to shortage of resources for future generations. The progress in technology provided an alternative source of energy in the form of nuclear energy, which has reduced the dependence on energy from fossil fuels for the time being. In December 1951, the first demonstration of using nuclear energy to light four bulbs was successfully presented in Idaho, USA [GR11]. In 1954, the first nuclear power plant was installed in Russia which generated electricity for commercial use [Sem83]. However, the power generation from nuclear energy has many challenges and limitations such as the elimination of the radioactive waste, the adverse effects on the environment due to the mining and extraction process of radioactive materials [Pea12], the scarcity of radioactive materials as well as the control of the cost per unit of the power produced by nuclear energy. Therefore, the challenges and limitations in producing power from fossil fuels and nuclear energy paves the path to explore and utilize other means of power generation such as solar energy and wind energy, which are the most valuable, clean, sustainable and abundant sources of energy.

6.1.2 Wireless sensor networks

The combination of sensing and wireless communication technologies provides foundations for wireless sensor networks (WSNs). In wireless sensor networks, many sensor nodes are spatially distributed in large areas to gather information, such as temperature and humidity, and send it to a sink node (for example, a base station) for processing. The sensor nodes, also called WSN nodes, may be positioned arbitrarily at locations that are inaccessible. In such situations, the sensor nodes must be highly efficient, consume low power and work for long periods of time. The WSNs have paved path for smart technologies, for instance environmental monitoring, fire detection, object tracking, vehicular adhoc networks, wearable gadgets and body area networks [GLCMB$^+$18, KSK13, FFB$^+$19, SGD$^+$15]. In traditional WSNs, power storage devices are used as substitute for power supply cords, but due to short lifetime and weight, power storage devices are not an optimal solution [ZPGC19]. Nevertheless, if used, cost of replacement or recharging may be very high. In other cases, such as body implants this may be very inconvenient as well. In designing a WSN, power consumption and power management are often the major constraints. A typical WSN node consists of a sensor and/or actuator, a computing

unit (MCU/ASIC/FPGA), a memory unit, a wireless communication transceiver, and a power management unit [Pop13]. The typical power consumption of sensors has already entered the microwatt range due to ultra-low power consumption chip technology [ZLL18]. For the computing units, different mechanisms are used to reduce the computational requirements such as integrating all the modules into a single chip and moving from 16 bit to 32 bit architecture [PMM13, KJA+14]. Communication transceivers can be power hungry if the communication distances are too large between the WSN nodes, but ultra-low power transceivers have been developed recently, which significantly reduce the power requirements [PPSM17]. Some of the techniques that can be used to optimize the power requirements of WSNs [PMM13] are wake-up radio receivers, smart power units, or dynamic power management. Together with these techniques using energy harvesting can greatly increase the robustness and durability of the system by extending battery life and meeting power requirements.

Wake-up radio receiver design addresses the energy depletion due to a radio module (RF module) in the WSN node. A significant amount of power can be wasted in the radio modules by idle listening, when the nodes are waiting for commands from the base station. This problem can be eliminated by using a wake-up receiver in the nodes, which enables the nodes to respond only when requested by the base station. The wake-up receiver may use the node transceiver or a separate transceiver. A wake-up receiver also deals with the problem of overhearing, when a specific node is required to operate and a signal is sent to it, but all the nodes become fully active to perform the task. The base station further uses addressing mechanisms with the request signal to avoid overhearing at the expense of some extra power, which is required by the node to decode the signal.

Smart power unit design provides solutions for improved power management by relying on alternate energy sources together with rechargeable storage devices. Using energy harvesters together with storage units increases the lifespan of the nodes. Harvesting energy from a single source is not a good option to rely upon for continuous and uninterrupted operation of the nodes because of the unpredictable nature of the environment. Therefore, energy is harvested from multiple sources, for example, piezoelectric, solar, wind, etc., and such systems are called hybrid systems.

Dynamic power management deals with non-uniform usage of the hardware components in WSN nodes. Depending on the task to be performed, hardware components, which are not needed are identified and their power is cut-off. The process of power transition is achieved by clock gating or power gating. In clock gating dynamic frequency and voltage scaling is used which is beyond the scope of discussion here. In power gating a switch is used to selectively turn off/on hardware components.

In view of the power optimization techniques, wireless power transmission is a cost effective, compact, diverse and sustainable energy acquisition mechanism, which provides

an attractive alternative to using a large number of electric storage devices.

6.1.3 Wireless power transmission

To fulfill the power requirements of these technologies wireless power transmission provides a feasible solution. The technique for energization without wires, where the source and the load are located at a distance from each other and there is no physical connection between them, is referred to as wireless power transmission (WPT).

If successful and powerful enough, WPT may also find applications in the energy distribution business with larger power needs, at least in certain specific scenarios. Solar radiation along with wind have become reliable sources of energy during the past years and there are well-established technologies to convert solar energy and wind energy into electrical energy. However, often these energy sources are not directly available at those places where the energy is needed for consumption. Therefore, the transmission of produced electrical energy is a challenge of increasing importance. Especially, the transmission of energy to mountainous terrains, disaster areas, electric vehicles, and portable gadgets can be scenarios of interest for WPT.

WPT will be an important part of next generation communication systems with energy neutral design (END). In END, energy from the environment, i.e., light, motion, heat, etc. is converted into electrical power and the process is called energy harvesting. Similarly, unused electromagnetic energy in the environment from surrounding wireless networks and other radio transmitting equipment, as well as dedicated power sources can be used as the source of energy to power WSNs automatically and adaptively.

A WPT system can be broadly classified into three types: near-field WPT, far-field directive WPT and far-field non-directive WPT [YRWR17, JNG+17, CC17]. An illustration is shown in Fig. 6.1.1(a). Near-field WPT is a non-radiating technique and it includes resonant coupling and non-resonant coupling displayed in Fig. 6.1.1(d) and Fig. 6.1.1(b). In resonant coupling, electrical energy oscillates between the electric field of the capacitor and the magnetic field of the inductor when the inductive and the capacitive reactances are of equal magnitude. Resonant coupling lies in a mid-range category. Non-resonant coupling, sometimes referred to as one-to-one inductive coupling, works with very short range, only. The change of the electric current passing through a coil (primary inductor) induces a voltage in a second coil (secondary inductor) placed nearby. Far-field directive WPT is a radiating technique and it includes Laser and microwave point-to-point connections as shown in Fig. 6.1.1(e). Far-field non-directive WPT is also a radiating technique and it includes RF rectennas, which use ambient electromagnetic waves to harvest energy. It can be used over long distances as shown in Fig. 6.1.1(c). Near-field WPT has already been commercialized in portable wireless accessories such as smart

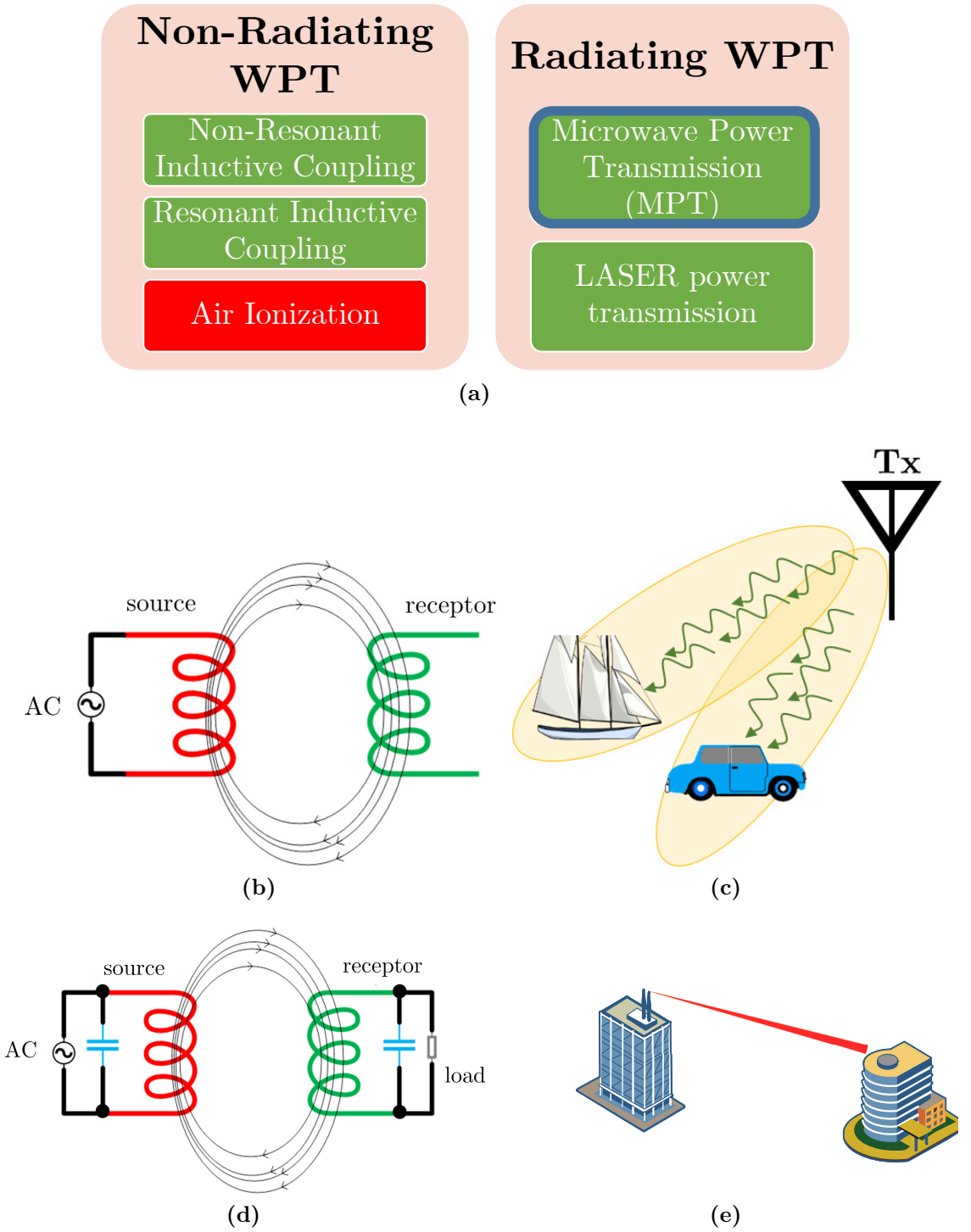

Figure 6.1.1: General classification of wireless power transmission based on distances: (a) WPT categorized as near-field (non-radiating) and far-field (radiating). (b) Non-radiating inductive coupling WPT. (c) Radiative non-directive WPT using MPT. (d) Resonant inductive coupling. (e) Radiative point-to-point WPT using a LASER.

phones, watches, and vehicles. This technology, due to its short range and the need of a docking station, as well as possible misalignment [CB13], limits its usefulness in daily

use accessories. The solution to these limitations is the far-field non-directive technology. It is consequently highly desirable to study the challenges in the implementation of the technology and propose solutions and designs for various applications.

In WPT systems, the receiving stations, where microwave energy receptors are located, are an essential part to achieve the desirable high end-to-end efficiency. A rectenna is used for this purpose, which is composed of an RF antenna connected to a low-pass filter and a rectifier. The idea of wireless power transmission dates back to the work demonstrated by Tesla [Che11]. In 1961, Brown, while working for Raytheon developed the first rectenna for efficient microwave reception and rectification [Bro61]. It was then, after the successful demonstration of microwave WPT, that Glaser proposed the application of Space Solar Power Satellites (SSPSs) [Gla68]. In this SSPS model, the electromagnetic energy radiated from the sun in the form of sunlight towards the earth is captured by photovoltaic cells in space. The captured energy is then transmitted to the earth in the form of microwave power beams. At the ground station, a large array of rectennas are used to receive the microwave energy and convert it to electrical energy. It is very unlikely that such a system will ever be feasible, but it inspired many people to develop different designs. Some of the proposed rectenna designs for microwave power transmission can be found in [MYC92, MTS11, SM98]. In the past decade, numerous designs and techniques have been proposed to reduce the size of the antenna, to achieve miniaturization; achieve greater power reception by optimizing the placement of the elements of the rectenna array; reduce harmonics and undesirable effects, which deteriorate the system performance due to the nonlinear behavior of the rectifier [EAR17, FRRM12, THC07]. The advances in semiconductor technology have also allowed to increase the rectification efficiency by using Schottky diodes, which have low forward bias voltage drop and fast switching behavior.

6.1.4 Wireless power transmission receiver architecture

The two general models for designing a WPT rectenna in a far-field WPT scenario are illustrated in Fig. 6.1.2. Fig. 6.1.2(a) shows the block diagram of the rectenna when an antenna is used as a primary wave collector. A conventional antenna receives the microwave power from the air. The pre-rectification filter performs two tasks: matching the complex impedance of the rectifier with the impedance of the antenna, and prevent secondary emission of the harmonics generated during the rectifying process. The microwave energy is then converted to DC power by a rectifier and a DC pass filter. Finally, DC power is delivered to the load. Fig. 6.1.2(b) presents a metamaterial rectifying surface as a primary wave collector. The conventional antenna has been replaced by a subwavelength metamaterial with an embedded diode and a DC pass filter. This design is simple, compact and can be easily integrated in layers. These designs are purely passive and require no

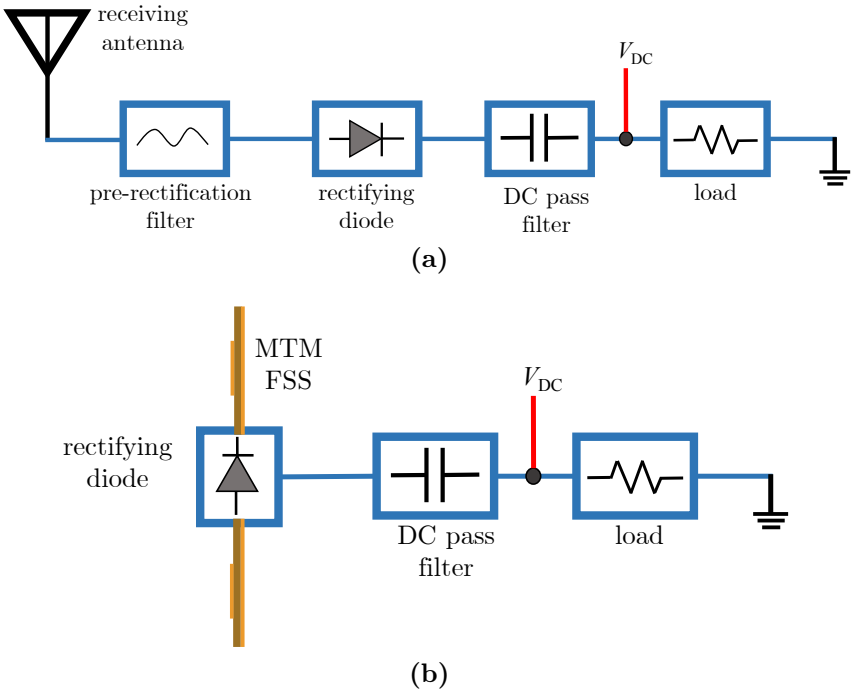

Figure 6.1.2: A generic block diagram for microwave power reception using (a) a conventional antenna and (b) a metamaterial surface as wave collector.

extra power.

Most conventional antennas, which have large radar cross section (RCS), suffer from unavoidable back scattering. This will directly affect the rectenna gain and cause scattering at the aperture, which will reduce the RF-AC conversion (the percentage of energy absorbed into the aperture with respect to the total incident energy on the antenna) and affect the overall system efficiency. In addition, incident angle dependence and impedance mismatch due to mutual coupling are some of the other critical factors. The received maximum power can be derived where additional atmospheric attenuation must be considered. The choice of the frequency for WPT systems could be around 3 GHz and larger since the atmospheric effects at these frequencies are minimal and electromagnetic waves can efficiently propagate.

6.1.5 Wireless sensor networks and wireless power transmission

WSN and WPT can be deployed together in agricultural lands to overcome challenges, such as water shortage, climate change and labor shortage [WCS+07]. In addition, due to urbanization, personalized care to farm and livestock is often overlooked. Therefore, WSNs can be used to monitor, identify and report problems related to soil erosion, water level, salinity, temperature, [SGD+15] etc. The nodes are placed at different locations

throughout the landscape, they may be buried or hanging. Using WPT and WSN together will allow to increase the number of nodes in large landscapes, and preemptive measures can, e.g., be taken against disease outbreaks and environmental changes.

6.2 State-of-the-art

Not long ago metamaterial particles have emerged as an alternative for microwave energy harvesting. Spilt ring resonators (SRRs) were used by Ramahi et al. for the first time to investigate their electromagnetic energy harvesting behavior [RAAB12]. It was shown that by inserting a resistive load in the SRR gap, it behaves like an energy collector. Later, an SRR was connected to a rectifier in form of a Greinacher circuit [HKC13]. It had a maximum efficiency of 36.8% at a frequency of 900 MHz. In [WYD+14], a new metamaterial design was proposed for space solar power satellite (SSPS) applications with higher absorption rate and suppressed harmonics. The design was composed of an I-type resonator which was bisected and connected to a bridge rectifier for full-wave rectification. The achieved rectifying efficiency was 28.81% at low incident power levels. Recently, T-matched dipole antennas were used for energy harvesting applications with full wave rectification [EAR17]. With 74%, they showed significant improvement in the RF-DC conversion efficiency.

Many of the power harvesting systems have focus on the design of the RF receive module and techniques to increase the microwave reception [THC07, AAA+17]. In [CC17], the design of a rectifier circuit and techniques to increase the conversion efficiency and reduce losses were shown. In [HKC13, DCZ16], matching a rectifier circuit to an RF receiver at a particular frequency is discussed, where both of the modules are optimized independently and integrated afterwards. One of the key technical challenges in designing a high end-to-end efficient power harvesting system is the integration of a rectifier element into the metamaterial (the RF receiver) such that the rectifier is optimized for the actual (realized) input power from the RF source (metamaterial receiver).

Although many rectenna designs have been proposed till date, most of the designs use a single band to harvest energy [MVVA11, SZG13, HKC13] and very few designs operate in multi-band modes such as [AAA+17, SGHZ13, NKJ+13]. In multi-band designs, usually multiple rectifiers are connected to wide-band antennas using separate matching networks for each band of operation. The focus has been mostly on optimizing the complex matching circuit for the rectifier to improve the efficiency. In addition, the rectifier can suffer from an early breakdown problem due to a fluctuation of the power levels of different ambient spectral bands. Moreover, the rectifier may operate outside the optimum range and thus result in low RF-DC efficiency [LZG15]. A rectenna with a switch can be used, but the design also requires to deal with a complicated detector [MVVA11]. Another

approach would be to use a high-electron-mobility transistor (HEMT) to avoid early breakdown and a dual-band matching circuit [LZG15]. Designing a matching circuit for non-harmonic frequencies can be a complicated task. Furthermore, all these solutions require additional circuits that will increase the power requirements of the nodes in WSNs. On the other hand a metamaterial based multi-resonant, multi-band design process can be used instead of a wideband antenna to minimize circuit losses, improve RF-DC efficiency and achieve a multi-band response [ES5].

Despite many efforts [DCZ16, WYD+14, FRP12], efficient microwave absorption and recovery as well as multi-band operation are still a very exciting research motivation. In particular, the recovery of microwaves at realistic (low) incident power levels is considered to be a challenge. In this thesis, metamaterial based designs are used to address the challenges discussed above and provide an improved, efficient and innovative design for power harvesting systems with dual-band operation and single band operation.

6.3 Microwave energy harvester

An efficient energy harvesting system requires an efficient power conversion module to transfer maximum power to the load along with a highly efficient radio-frequency (RF) receiver to collect all the incident electromagnetic waves. In literature, many rectifier designs have been proposed, some of them have been studied for microwave energy harvesting systems. In most of the systems, the rectifier is connected to the RF source and matched at a particular frequency of operation. The level of input power to the rectifier must also be considered to achieve maximum power conversion by the rectifier [CC17]. High input power can cause early breakdown while very low input power may limit the rectifier operation. The important parameters that determine the power conversion efficiency of a diode in a rectifier are the series resistance, which introduces Ohmic losses and reduces the circuit efficiency, the forward bias voltage, which limits the input power required to operate the diode, the breakdown voltage that limits the power handling capability of a rectifier circuit, and the zero-bias junction capacitance that influences how harmonic currents oscillate through the diode. The material characteristics of the rectifying element have strong influence on these parameters. For high power conversion efficiency of the rectifier and high end-to-end system efficiency, the diode needs to have low series resistance, low forward bias voltage, high breakdown voltage, and low junction capacitance. Unfortunately, high breakdown voltage and low forward bias voltage cannot be achieved simultaneously for a single diode due to technological limitations. Design principles and considerations for each module, i.e., RF module and rectifier are explained in the following.

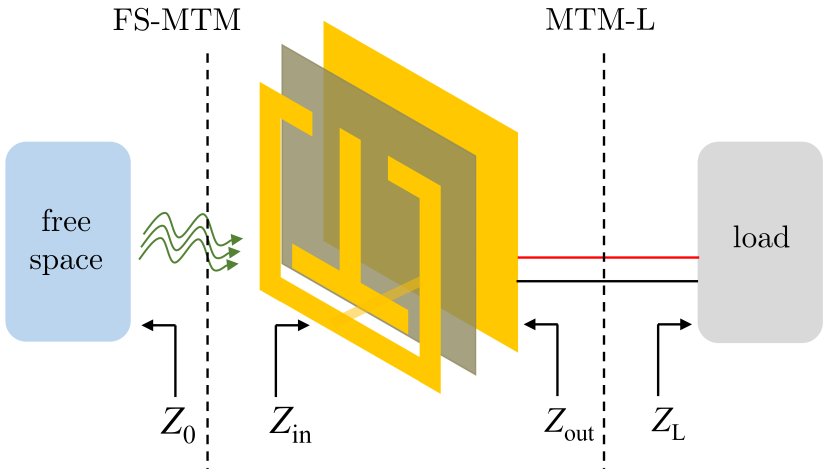

(a)

Figure 6.3.1: A typical metamaterial (MTM) based energy harvesting rectifying surface connected to a load, which can have resistive impedance as well as complex impedance.

6.3.1 Microwave receiver (RF module)

As discussed previously, the wave collector can be realized by antennas and metascreen unit cell designs, as well as in a hybrid design that uses both classical antennas and a metascreen. In this thesis a metamaterial based unit cell design approach is used to demonstrate the energy harvester operation and performance. The use of antenna elements in the rectenna design for wireless power transmission has been previously studied and publications can be found in [HKST15, THC07, SSC+14]. However, the focus of these studies was on different applications. In some cases, the goal was to increase the conversion efficiency using different types of rectifier designs or to improve the matching [MCT+09, Ito15]. A comprehensive study and investigation on energy harvester designs is necessary to pave path for the realization of an efficient and cost effective model for WSNs. For instance, the power level in WSNs is low due to safety levels and small modules. This means that the available power at the rectenna will be limited by the power incident on a single antenna (per unit square). Therefore, converting microwave power to usable power will require the implementation of rectenna arrays. However, in applications such as body implants large arrays may not be possible to realize, which means a high unit cell efficiency is required at low power levels. Designing an array will introduce coupling effects from the neighboring unit cells, which may need to be dealt with care.

Fig. 6.3.1 shows the schematic diagram of the energy harvester, to realize the wave collector that is based on the design of a metamaterial unit cell, which, when arranged periodically, behaves as frequency selective surface. Frequency selective surfaces are usually composed of metallic resonating elements which are periodically arranged to

pass, block or absorb electromagnetic waves at a certain band of frequencies with high transmission coefficient, reflection coefficient or absorption rate, respectively (discussed in detail in previous chapters). When a frequency selective surface is backed by a metal layer (sheet), it blocks the wave from being transmitted to the other side of the surface. As a consequence, a part of the incident wave is absorbed and the rest is scattered back to the incident medium. The frequency at which the absorption occurs depends on the overall system inductance and capacitance. The Q-factor of the structure gives information on how quickly the energy would be stored in the resonator and how fast it would decay. It can be controlled by the geometric parameters of the unit cell design, the material characteristics, and mutual interactions between the resonators. Such frequency selective surfaces are called electromagnetic absorbers (discussed in Section 4.5.2) and they are the fundamental building block for the kind of energy harvesters discussed in this thesis. Unlike metamaterial absorbers, where the induced energy is dissipated in the structure, when the incident wave is absorbed, the energy inside the structure needs to be conserved. Therefore, the metal film in the bottom layer behaves like a ground and a via is created on the resonator as shown in Fig. 6.3.1. The via provides the path for the current to flow through the resistor or get converted to DC using a rectifying circuit. The difference between an electromagnetic energy harvester and an electromagnetic energy absorber is that the former requires maximum electromagnetic energy absorption and also maximum power transfer to the load.

The challenges in designing a receiver system to meet high end-to-end efficiency firstly require that the receiver absorbs all the incident microwave energy even at low incident power density levels. This implies that the impedances at the first interface FS-MTM in Fig. 6.3.1 must be equal ($Z_\circ = Z_{\text{in}}$). The load can have a resistive or a complex impedance. In either case, it should be power matched. The maximum transfer of the absorbed energy to the load occurs at the MTM-L interface, the output impedance of the surface must be equal to the complex conjugate impedance of the load ($Z_{\text{out}} = Z_{\text{L}}^*$).

6.3.2 Rectifier

The second design requirement is a rectifier circuit, which has a low voltage drop and high AC – DC conversion efficiency. The rectification can be achieved by using Schottky diodes or field effect transistors (FETs). The rectifiers for energy harvesting systems are usually constructed using a single diode connected in series or shunt (also known as half wave rectifier), or diodes connected in bridge configuration (also known as full wave rectifier) [HKST15]. The choice of the type of rectifier depends on the application. Other considerations may include effects of impedance matching, AC – DC conversion efficiency and overall rectenna efficiency. Using a rectenna array will allow to collect more power and help to increase the overall system efficiency. Fig. 6.3.2(a) and Fig. 6.3.2(b) show

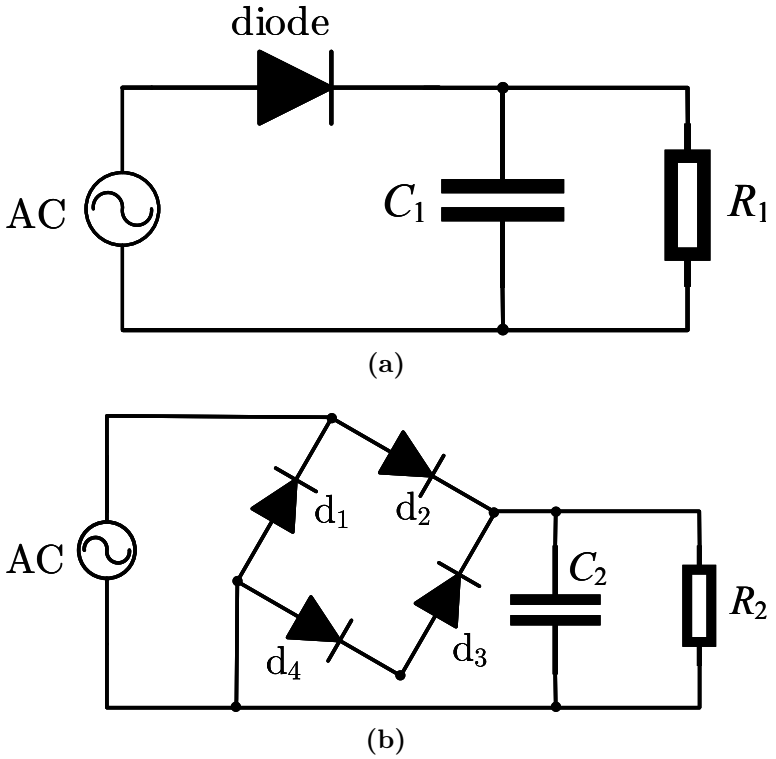

Figure 6.3.2: (a) Typical half-wave rectifier circuit. (b) Typical full-wave rectifier circuit.

simple rectifier circuit designs that have been used in literature. Theoretically, half-wave rectifiers have the advantage that they offer low losses. Therefore, half-wave rectifiers can be used for low input power levels while full-wave rectifiers can be used for high power levels. For each rectifier design the output impedance of the metamaterial surface will have to be optimized accordingly. This depends on the geometric parameters and the coupling between the resonating elements. The output impedance of the metamaterial surface changes with frequency. Therefore, the harmonics produced by the diode will see a severe impedance mismatch with the metamaterial surface. The harmonics will oscillate between the capacitor and the metamaterial surface until fully rectified by the diode. The rectifier power conversion efficiency (RPC_e) can be defined as

$$RPC_{\mathrm{e}} = \frac{P_{\mathrm{DC}}}{P_{\mathrm{in}}}, \tag{6.3.1}$$

the powers on the right hand side of eq. (6.3.1) are expressed as

$$P_{\mathrm{in}} = \frac{(V_{\mathrm{in}}^{\mathrm{rms}})^2}{R_{\mathrm{L}}}, \tag{6.3.2}$$

$$P_{\mathrm{DC}} = \frac{V_{\mathrm{out}}^2}{R_L}. \tag{6.3.3}$$

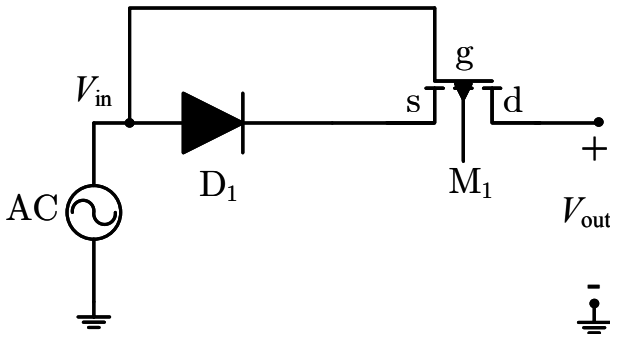

Figure 6.3.3: Layout of rectifier for extending power range. s, g, and d represent source, gate and drain of the HEMT M_1, respectively.

where R_L is a load resistance, P_{DC} and P_{in} are output (rectified) power and incident power, respectively.

Since the rectifier impedance is a function of frequency, delivering the absorbed energy to a rectifier will require a careful consideration of complex impedance matching between the metamaterial unit cell and the rectifier. A rectifier consists of a non-linear conversion element and reactive elements, which leads to a complex and even signal amplitude dependent impedance. Therefore, the rectifier usually performs well in a small band of frequencies at a particular input power level. While the output impedance of the metamaterial should match the input impedance of the rectifier circuit, the output impedance of the metamaterial should not match with the input impedance of the rectifier at harmonic frequencies. It is desired that the forward bias voltage is low for energy harvesting application due to the low input power, but the breakdown voltage should be high since multi-band operation can cause high input powers. In general, both properties cannot be achieved simultaneously. In order to extend the power range (low forward bias voltage and high reverse breakdown voltage), a rectifying topology has been proposed by [LZG15] as shown in Fig. 6.3.3. The diode D_1 is connected with the HEMT M_1 in series configuration. When the rectifier is operating in forward biased state ($V_{in} > V_{out}$), the gate to source voltage (V_{gs}) of M_1 will be greater than zero and M_1 will be in on mode, but together they will perform like a normal diode. When the rectifier is reverse biased ($V_{in} < V_{out}$), M_1 will be in on mode as long as the reverse bias is small ($V_{gs} >$ threshold voltage) and the rectifier will operate normally. When the reverse bias increases such that the gate to source voltage of M_1 becomes very small ($V_{gs} <$ threshold voltage), M_1 will be switched off. At this point, the voltage on D_1 remains constant within the breakdown range and a large part of the voltage will apply to the source and the drain of M_1 until the reverse bias voltage reaches the breakdown voltage of M_1, which is the maximum gate to drain voltage (V_{dg}). Therefore, the overall breakdown voltage of the equivalent rectifier is increased to V_{dg} of M_1 [LZG15].

6.3.3 Key performance indicators

The electromagnetic energy harvesting system performance can be evaluated by its absorption efficiency (A_e), its harvesting efficiency (H_e), and its conversion efficiency (C_e), given as

$$A_e = \frac{P_a}{P_r}, \tag{6.3.4}$$

$$H_e = \frac{P_l}{P_r}, \tag{6.3.5}$$

$$C_e = \frac{P_l}{P_a}, \tag{6.3.6}$$

where P_a is the amount of incident power absorbed by the metamaterial surface, P_r is the amount of power incident per square unit, and P_l is the power delivered to the load ($P_l = P_{DC} = V_{DC}^2/R$).

6.4 Dual-band harvester

As earlier discussed in this thesis, two distinct types of resonating elements, a T-type resonator and a rectangular split ring resonator (RSRR), are combined together on

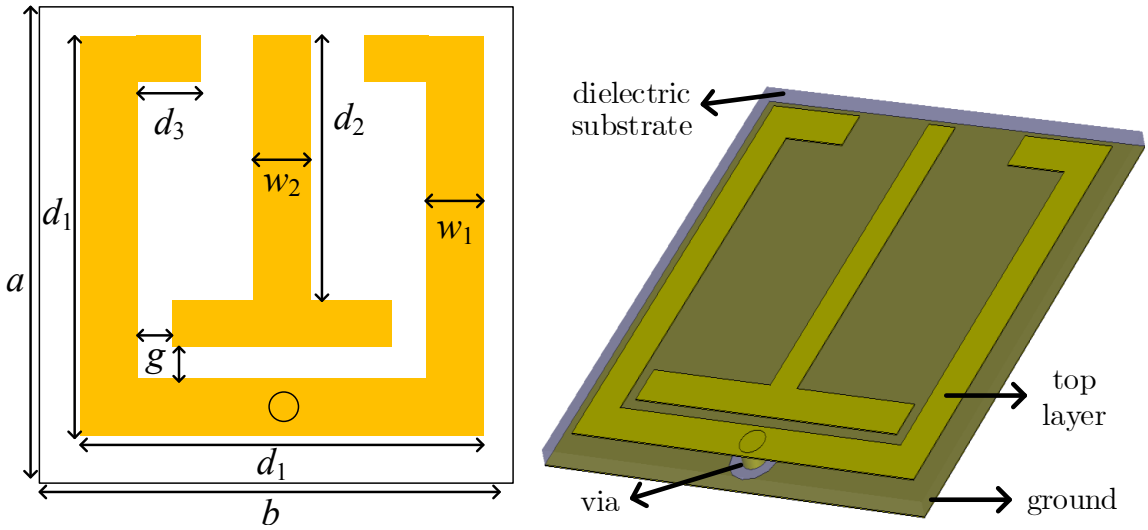

(a) Top view **(b)** Perspective view

Figure 6.4.1: First configuration of metamaterial unit cell where $a = 10\,\text{mm}$, $b = 10\,\text{mm}$, $d_1 = 9\,\text{mm}$, $d_2 = 7.24\,\text{mm}$, $d_3 = 1.5\,\text{mm}$, $w_1 = 0.8\,\text{mm}$ $w_2 = 0.7\,\text{mm}$, $g = 0.26\,\text{mm}$, via= $0.6\,\text{mm}\,\emptyset$.

a dielectric substrate RO4350 as shown in Fig. 6.4.1. The unit cell structure and its dimensions are presented in Fig. 6.4.1(a). The dielectric layer is backed by a copper film, which acts as ground. The top layer is also printed with copper having a thickness of 0.0175 mm and the metal ground plate has the same thickness. The dielectric substrates have a thickness of 0.254 mm with a relative permittivity equal to 3.48 and a loss tangent of 0.0037. The via of diameter 0.6 mm is used to connect the load to a ground metal plate as shown in Fig. 6.4.1(b). The structure has been simulated in CST Microwave Studio using the frequency domain solver.

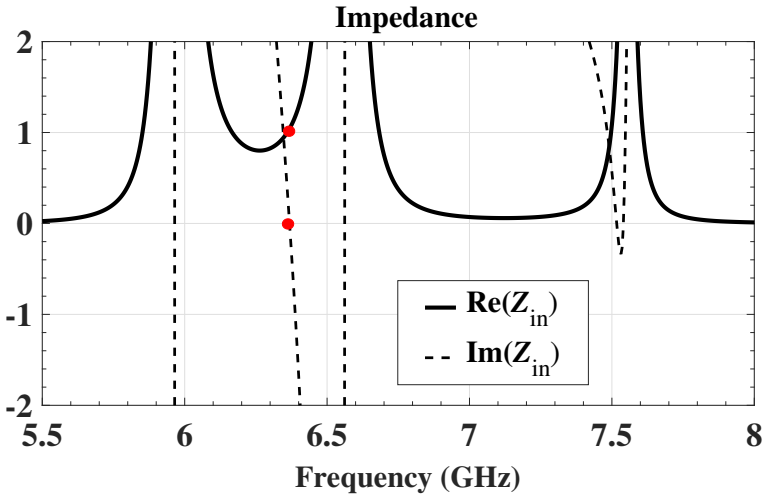

(a)

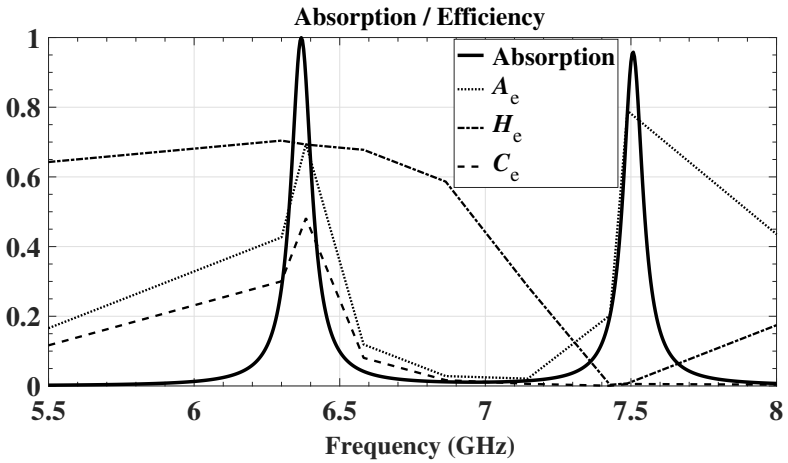

(b)

Figure 6.4.2: (a) The impedance of the meta-absorber. The dots indicate the values for real and imaginary component of Z_{in} at resonance. (b) Absorption and power efficiency of the metamaterial structure as a function of frequency where A_{e}, C_{e}, and H_{e} are absorption efficiency, conversion efficiency, and harvesting efficiency, respectively.

As an initial investigation, a simplified structure is designed with a single via on the RSRR and no substrate underneath the metal ground to mount the load. A $y-$polarized electromagnetic plane wave propagating in negative $z-$direction is normally incident on the metamaterial structure shown in Fig. 6.4.1 with unit cell boundary conditions in $x-$ and $y-$direction. It is observed that the structure has two S_{21} resonance peaks at 6.37 GHz and 7.5 GHz. Investigating the surface current distribution of the structure it is seen that anti-circulating currents are generated in the right and left loop of the structure at the resonance frequency. The current density is strong in the RSRR at 6.37 GHz and merging where the via is located and it is strong in the T-resonator at 7.5 GHz. The absorption is achieved by reducing the reflection and transmission as low as possible (for perfect absorption $|S_{11}| = |S_{21}| \longrightarrow 0$). Transmission is minimized by backing the structure with a metal film and to minimize the reflection matching is used. The expression for absorption, $A(\omega) = 1 - |S_{11}(\omega)|^2 - |S_{21}(\omega)|^2$, is then simplified to $A(\omega) = 1 - |S_{11}(\omega)|^2$. The effective constitutive parameters are optimized to be $\varepsilon_r = 66.6 + j180.38$ and $\mu_r = 69.11 + j196.6$, which result in a complex impedance $Z_{in} = (1.04 + j0.008)\ \Omega$ at 6.37 GHz as seen in Fig. 6.4.2(a). The small imaginary component implies good matching with the free space impedance. The gap g plays a critical role in controlling the impedance because of the strong electric field density at the bottom of the structure.

In Fig. 6.4.2(b) it is seen that at the matching frequencies perfect absorption is achieved. Increasing the load resistance increases the absorption significantly, but reduces the power delivered to the load. Therefore, the harvesting efficiency reaches the maximum

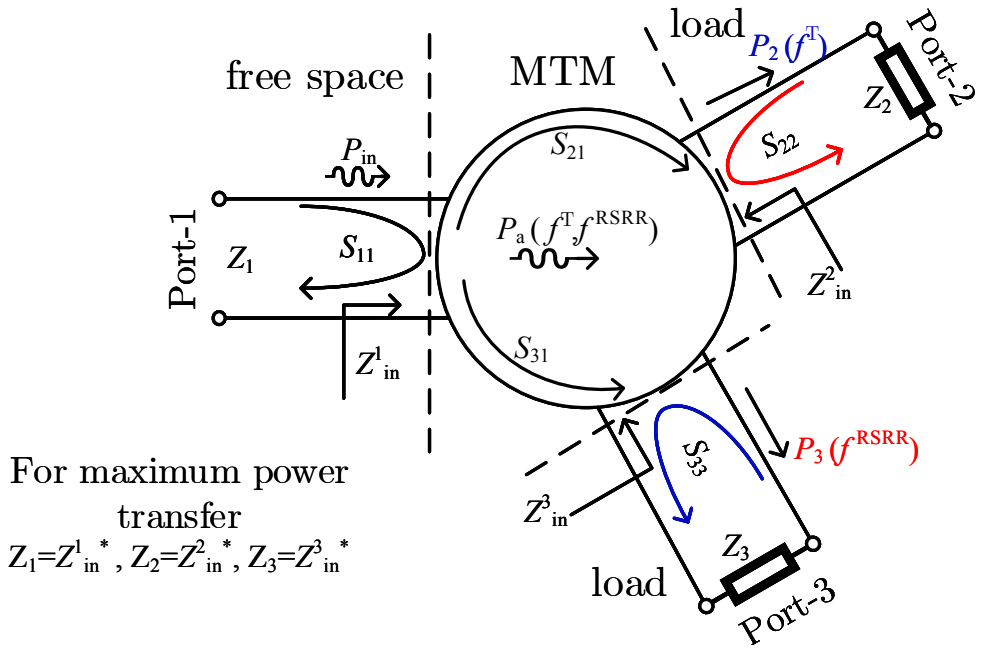

Figure 6.4.3: Equivalent three-port network layout for dual-band energy harvester design. Z_1 represents the free space impedance. $|S_{23}|$ and $|S_{32}|$ are below -25 dB and hence not shown.

value when a resistive load of 750 Ω is connected between via and ground. Fig. 6.4.2(b) also illustrates the power efficiency of the structure where, $A_e = \frac{P_a}{P_s} = 69.5\%$, $C_e = \frac{P_l}{P_a} = 69.29\%$, $H_e = \frac{P_l}{P_s} = 48.16\%$ at 6.37 GHz resonance frequency. Increasing the load resistances increases A_e, but H_e starts to decrease, if the load resistance exceeds a certain value. Therefore, the optimum value of resistance is chosen so that the maximum current can pass through the load at the resonance frequency. The structure can be used to harvest at 7.5 GHz by placing a via at the junction of the T-resonator.

After the initial analysis, the problem is extended for dual-band behaviour and the concept is summarized using a three port network layout as shown in Fig. 6.4.3 for the design. The unit cell design is modified so that it is more practical and less lossy. The modified design with geometric parameters is displayed in Fig. 6.4.4.

Consider an electromagnetic plane wave incident normally on the structure shown in Fig. 6.4.4. The incident wave is y-polarized and it is travelling in $-z$-direction. The wave is partly reflected and partly transmitted from the structure at the resonance frequencies. Since the structure has two resonating elements placed close together, the individual resonance frequencies of the RSRR and the T-type resonator will be affected by the mutual coupling between them. Additionally, a low loss dielectric substrate is used relative to the initial design (Fig. 6.4.1). The dielectric substrates have a thickness of 0.254 mm with a relative permittivity equal to 2.2 and a loss tangent of 0.0009. The goal is to minimize the reflection of the incident wave so that the absorption can be maximized at the resonance frequencies, to make sure the absorbed energy is not dissipated within the structure but rather efficiently diverted to the loads, and avoid a matching network.

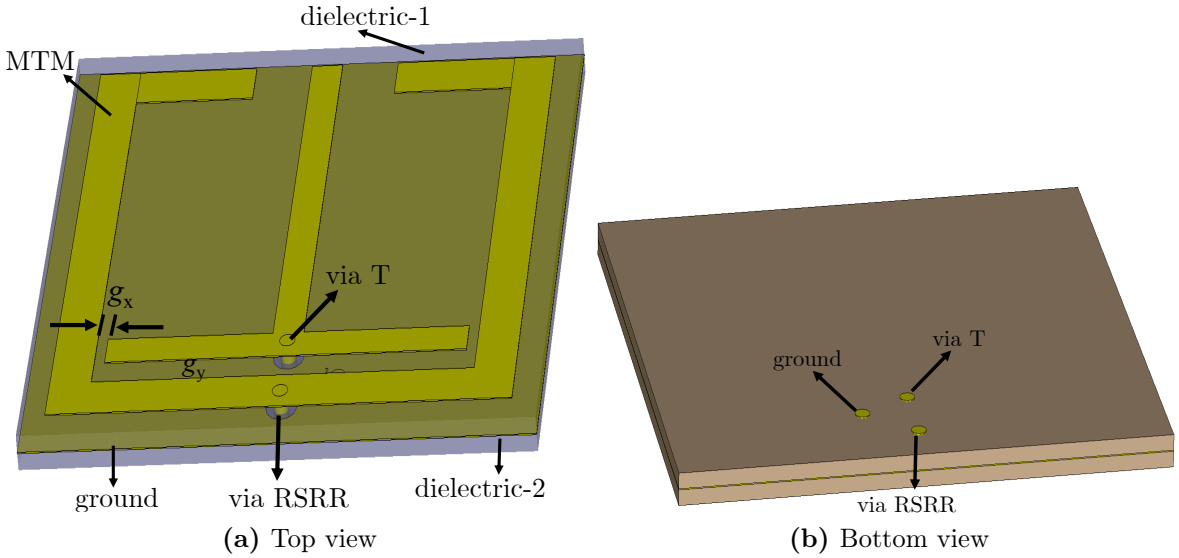

(a) Top view **(b)** Bottom view

Figure 6.4.4: Second configuration of metamaterial unit cell where $a =$ 10 mm, $b =$ 10 mm, $d_1 =$ 9 mm, $d_2 =$ 7.1 mm, $d_3 =$ 2.3 mm, $w_1 =$ 0.8 mm $w_2 =$ 0.6 mm, $g_y =$ 0.5 mm, $g_x =$ 0.2 mm, and both via = 0.3 mm Ø.

The challenge here is to match the impedance of the structure with the incident medium, which is free space and its value is $Z_1 = 376.7\ \Omega$, at both the resonance frequencies. An identical permittivity and permeability of the structure will result in achieving a matched condition. The concept of harvesting energy at two different frequencies with two different loads, respectively, is illustrated through a three-port network shown in Fig. 6.4.3 where different ports (2 and 3) are used for two different loads. Port 1 represents the incident medium, Port 2 and Port 3 represents the load connected to the T-resonator and the RSRR, respectively. The load impedances at Port 2 and Port 3 are resistive and their values are $Z_2 = 750\ \Omega$ and $Z_3 = 1040\ \Omega$. In order to achieve maximum power transfer to

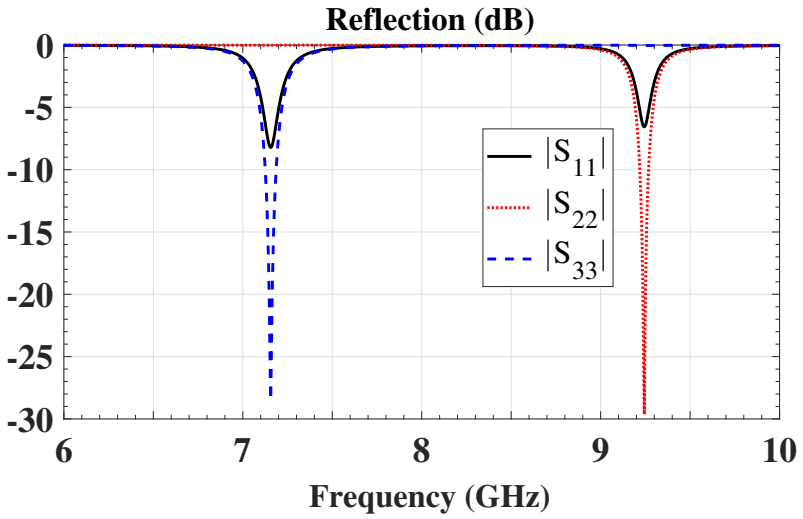

(a)

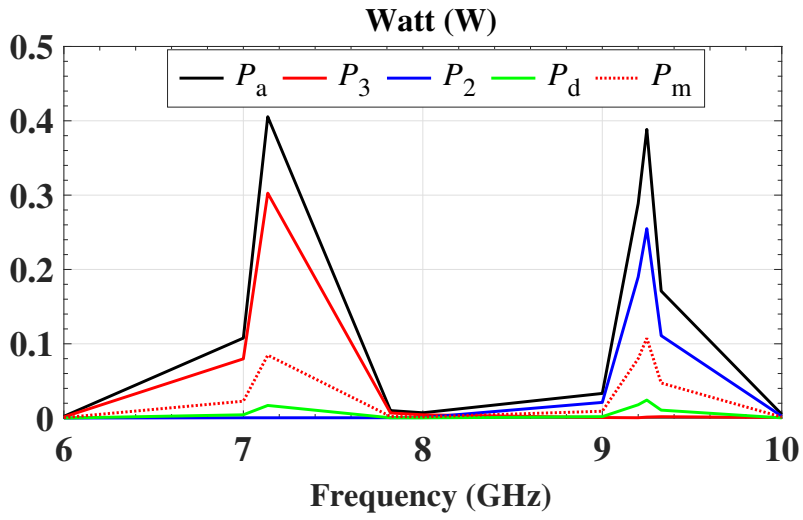

(b)

Figure 6.4.5: (a) Magnitude of the reflection coefficients at different ports as a function of frequency. (b) Power absorbed by materials and loads as a function of frequency.

the loads, the output impedances of the structure must be equal to the complex conjugate impedances of the loads; otherwise, matching networks will be required. In this thesis, only resistive loads are modeled for simplicity. Vias are used to connect the loads to the resonators. The resonance frequency due to the T-resonator is represented by f^{T} and the resonance frequency due to the RSRR is represented by f^{RSRR}. The power absorbed at both the frequencies is P_{a}. However, S_{21} is only maximum at f^{T} resulting in non-zero power $P_2(f^{\mathrm{T}})$ across Z_2, whereas S_{31} is only maximum at f^{RSRR} resulting in non-zero power $P_3(f^{\mathrm{RSRR}})$ accross Z_3. The impedance Z_2 (Z_3) acts as open/unmatched load at f^{RSRR} (f^{T}). Fig. 6.4.5(a) shows the reflection coefficient for all the ports. The resonance frequencies for the RSRR and the T-type resonator are 7.16 GHz and 9.25 GHz, respectively. It can be seen that $|S_{11}|$ has two reflection zeros implying that the structure is matched at two resonance frequencies. On the other hand the S_{22} and S_{33} have each single reflection zero at their respective matching frequencies. Fig. 6.4.5(b) shows the power absorbed, the power delivered to the loads, and the power dissipated in the dielectric (P_{d}) and the metal (P_{m}). It is observed that the efficiency is improved because of low loss due to the dielectric substrate (it should be noted that in the case of metamaterial absorbers, since the goal is to dissipate energy within the structure, a lossy dielectric substrate is chosen as already discussed in Chapter 4, while for the case of the energy harvester material losses need to be minimized to get high end-to-end efficiency). Table 6.4.1 shows a comparison of the efficiencies at the resonance frequencies. The efficiencies can be further improved by considering actual complex impedances at the loads.

Table 6.4.1: Power efficiencies

Resonance frequency	A_{e}	H_{e}	C_{e}
7.16 GHz	81%	60.5%	74.7%
9.25 GHz	77.6%	51%	65.6%

The dual-band of operation based energy harvester design is an efficient solution that can be used in wireless sensor networks:

- In wake-up receivers, one of the bands can be used to avoid idle listening and turn on the transceiver only when required. The second band can provide enough power to the node that is required to perform signal processing for addressing mechanism.
- For dynamic power management, the energy harvester can be used as a switch or as a power source for the switches to turn hardware components off/on.

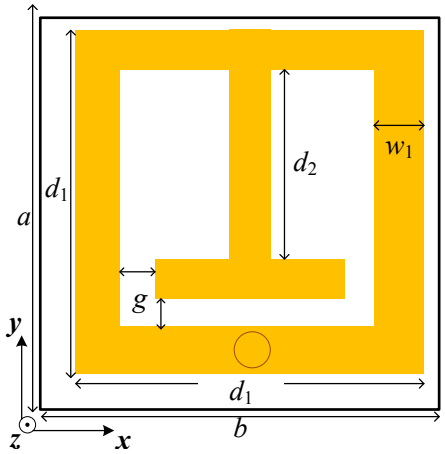

Figure 6.5.1: (a) Metamaterial energy harvester unit cell for single-band of operation where a = 10 mm, b = 10 mm, d_1 = 9 mm, d_2 = 6.34 mm, w_1 = 0.8 mm, g = 0.26 mm, via= 0.6 Ø.

6.5 Single-band harvester

The power management and optimization of the sensor nodes in wireless sensor networks, as discussed, can also be done using a smart power unit. This means to rely on multiple power sources. In this regard, dual-band operation may not be an ideal solution due to relatively low efficiencies. Therefore, a single-band design approach is adopted to achieve higher efficiencies, which presents a more attractive solution for a particular application.

In the single-band design, both the resonators are physically joined such that a single absorption band is produced. The losses due to metal and dielectric are reduced in a single absorption band design. The structure now has a T-type resonator inside a square loop printed on a dielectric substrate Rogers RO3003 and backed by a copper ground. The dielectric substrate has permittivity ε = 3.0, loss tangent 0.001 and thickness 0.254 mm. A single via is located at the bottom of the structure, which channels the power to the resistive load as shown in Fig. 6.5.1.

Since the structure is sensitive to an electric field vector along the $y-$axis, a plane wave with such an electric field vector is incident on the proposed unit cell structure with 0.5 W power per unit cell. The structure resonates at 6.75 GHz and its surface current and field distributions are shown in Fig. 6.5.2. Most of the energy is absorbed by the structure. The electric fields are stronger at the bottom and the top of the structure while parallel surface currents are induced in the vertical arms of the resonator which merge at the optimal location of the via. Anti-parallel currents are generated in the gap between the T-type resonator and the square loop at the bottom of the structure. For an electric field vector along the $x-$axis, the structure resonates at 5.85 GHz and all of the

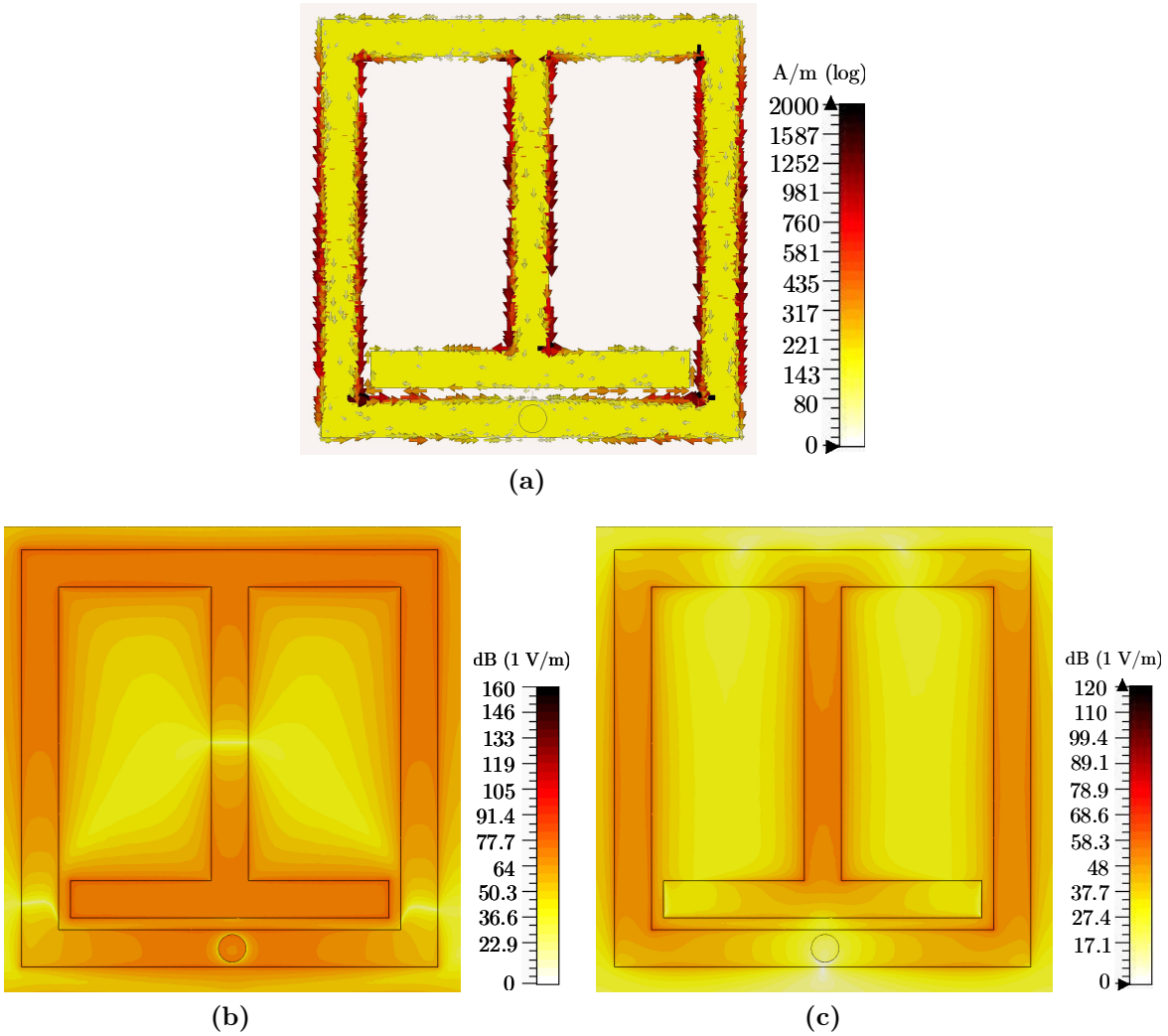

Figure 6.5.2: At the resonance frequency 6.75 GHz (a) electric surface current distribution, (b) electric field distribution, and (c) magnetic field distribution.

energy is lost with in the structure.

The effective constitutive parameters are optimized at the resonance frequency. Fig. 6.5.3 shows the permittivity and the permeability as a function of frequency for the energy harvester design illustrated in Fig. 6.5.1. It has been discussed previously that the resonant structures have dynamic range of material parameters around the resonance frequency (discussed in Section 2.2.5). It can now also be seen in Fig. 6.5.3 that the permittivity and the permeability change a lot near the resonance frequency. The green dots indicate the corresponding values at the resonance frequency. At the resonance frequency, $\varepsilon_r = 38.80 + j80.46$ and $\mu_r = 84.45 + j235.9$, which result in a complex input impedance looking into the structure from the incident medium to be $Z_{\text{in}} = (1.76 + j0.1)\,\Omega$ as shown in Fig. 6.5.4. In simulations, the load is only modelled with a resistive element of $490\,\Omega$. At the resonance frequency the output impedance looking into the structure from the load is $Z_{\text{out}} = (1 + j0.02)\,\Omega$ as shown in Fig. 6.5.4. Furthermore, since impedance is a

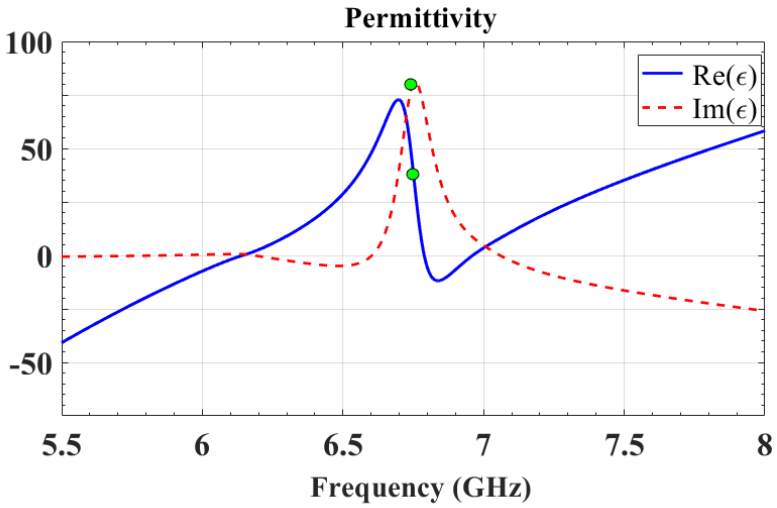

(a)

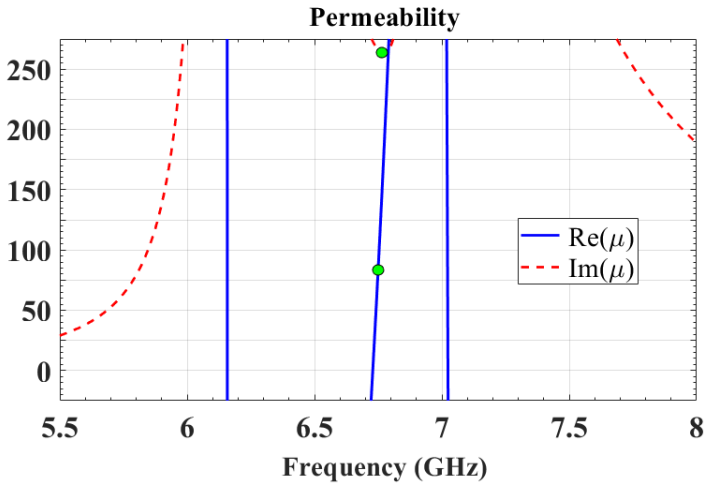

(b)

Figure 6.5.3: (a) Effective permittivity. (b) Effective permeability.

function of frequency, it is observed that at harmonic frequencies Z_{out} is different than at the resonance frequency, which is a desired characteristic. Such mismatching prevents the reradiation of the harmonics produced by a non-linear element of the rectifying circuit. The impedances of the structure imply good matching at the input and output ports.

The matching of the single-band energy harvester can also be illustrated using S-parameters as shown in Fig. 6.5.5. Port 1 is used when the incident wave is excited from free space and port 2 is across the load. $|S_{11}|$, $|S_{22}|$ and $|S_{21}|$ represents the reflection coefficient at the input interface (FS-MTM), and reflection coefficient at the output interface (MTM-L), and transmission coefficient from port 1 to port 2, respectively. The distribution of the absorbed power (P_{a}) in the structure and the load is illustrated in Fig. 6.5.6. It is seen that 78.3% of the total absorbed power is delivered to the load (P_{l}) which equals to 0.361 W. The losses due to dielectric (P_{d}) and metal (P_{m}) are 0.02 W and 0.07 W, respectively, at 6.75 GHz.

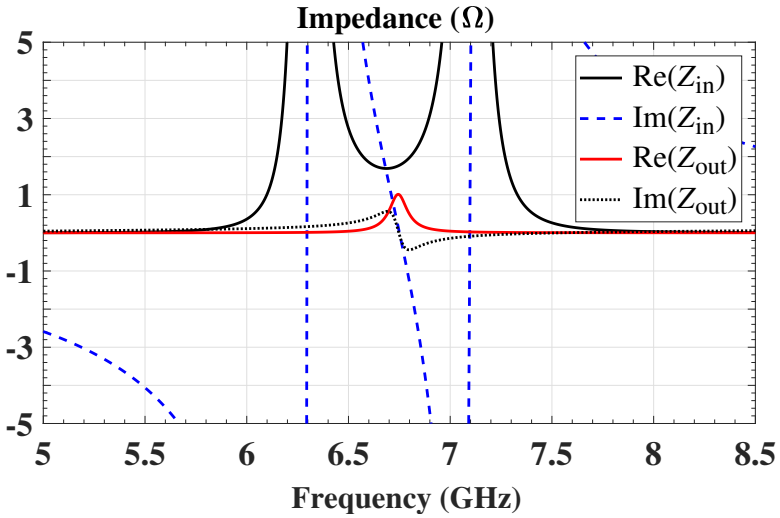

Figure 6.5.4: Normalize input impedance when incident medium is free space and normalize output impedance when the load connected is 490 Ω.

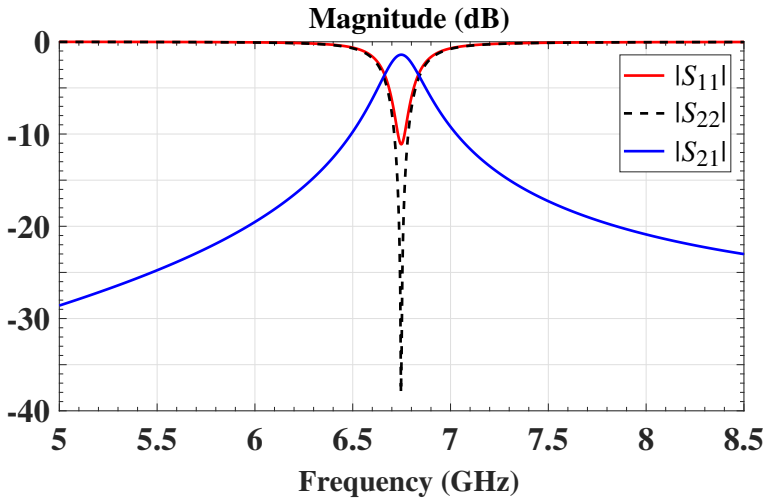

Figure 6.5.5: Reflection and transmission coefficients of single-band energy harvester.

Other important aspects in the analysis of the wave collector are the oblique incidence angle stability and the harvesting efficiency. Fig. 6.5.7 and Fig. 6.5.8 shows the behavior of the harvester design at oblique incidence angles. The resonance frequency remains stable with no shift in the frequency. When the incidence angle is increased, the absorbed power along with the dissipated power gradually decrease until 45° and from there onwards a significant loss due to reflection is observed. However, the conversion efficiency (C_e) remains almost the same for all presented incident angles. At 60° incidence angle, the power delivered to the load is almost 0.2 W. Table 6.5.1 depicts the change in the absorption and dissipation of the power along with the efficiencies for different incident angles.

The single-band energy harvester design and its performance shows the prospect

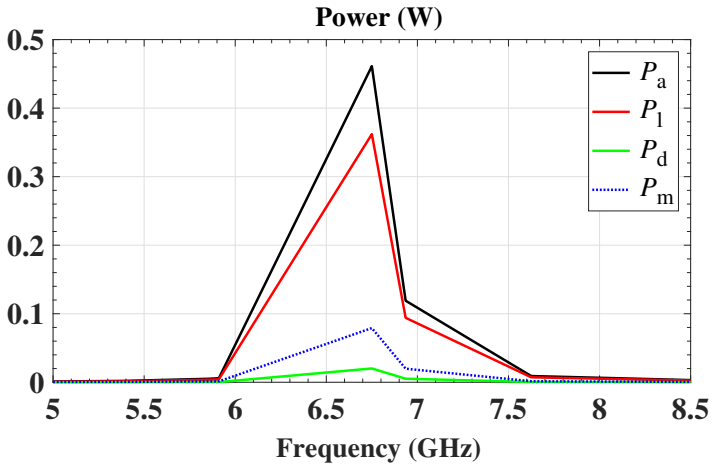

Figure 6.5.6: Power distribution of the captured energy in the proposed unit cell. P_a, P_l, P_d, P_m are the power absorbed by the structure, power dissipated in the resistive load, power losses in dielectric and power losses in metal, respectively.

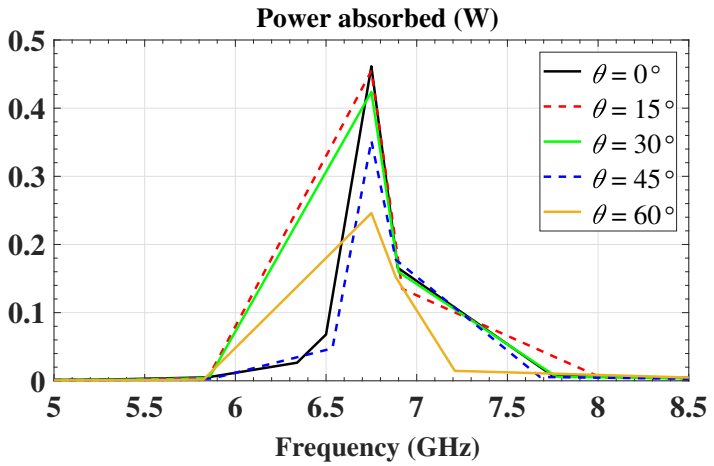

Figure 6.5.7: Power absorbed by the metamaterial structure as a function of incident angle.

Table 6.5.1: Power and efficiencies for oblique incidence angles

	$\theta = 0°$	$\theta = 15°$	$\theta = 30°$	$\theta = 45°$	$\theta = 60°$
P_a in W	0.461	0.455	0.424	0.352	0.246
P_l in W	0.361	0.356	0.332	0.276	0.193
A_e	92.2%	91.0%	84.8%	70.4%	49.2%
C_e	78.3%	78.2%	78.301%	78.4%	78.5%
H_e	72.2%	71.2%	66.4%	55.2%	38.6%

that the harvester can be utilized as an alternative source of energy for WSN nodes, more specifically, in a smart power unit multiple sources of energy are used to power up the nodes or devices. In situations where the nodes are buried or implanted, a microwave energy harvester can be a feasible and reliable alternative compared to most common energy sources, for example, solar or wind energy.

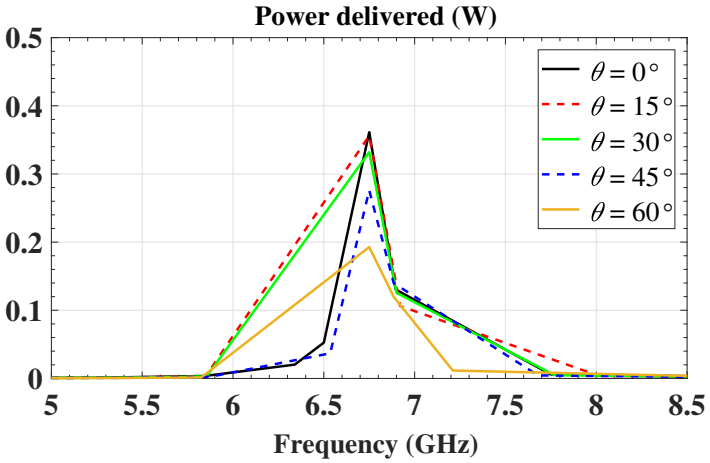

Figure 6.5.8: Power delivered to the load as a function of incident angle.

6.6 Summary

Metamaterial based energy harvesters have been discussed to improve the power management for wireless sensor network nodes. A dual-band harvester layout and its application in a wake-up receiver and the dynamic power management unit were discussed. A single-band harvester was found to have high efficiencies, which makes it a good choice as a source of energy for inaccessible nodes.

CHAPTER 7

Summary and Conclusion

A mult-resonator based metamaterial unit cell was introduced in this thesis. A rectangular split-ring resonator and a T-type resonator were tightly coupled in a single unit cell to investigate strong mutual coupling between the resonators. The mutual coupling between the resonators was exploited to achieve unique, distinct and extra-ordinary behavior. Multiple resonators allowed to achieve multiband characteristics and helped to introduce regions of strong mutual coupling for further miniaturization and tunability. After the determination of the transmission characteristics of the structure as a frequency selective surface, the concept was further enhanced and applied to design filters for hollow waveguides, microwave absorbers, polarization converters and energy harvesters. Factors that give control over the characteristics of the structure were identified and it was observed that the resonance frequencies can be controlled with very few parameters.

To simulate periodic meta-sheets as frequency selective surface or polarization convertor, Floquet ports in CST Microwave Studio were used with the frequency domain solver and periodic boundary conditions. For the hollow waveguide filters and microwave absorbers, a WR90 hollow waveguide was modelled hence, waveguide ports were used within the frequency domain solver.

Measurements were performed for the frequency selective surface and the polarization converter in free-space with a bistatic transmission measurement setup. The meta-sheets were surrounded by absorbers and time gating was applied to filter out parasitic propagation paths. Waveguide filter and microwave absorber measurements were performed with a WR90 hollow waveguide. The calibration was done using the through-reflect-line approach.

The simulated and measured results showed a very good agreement. The study

paves path to investigate multiband tunable structures, which are compact and have independent resonance frequencies. In this regard, a concept of a microwave energy harvester for wireless sensor networks was presented. The results are very convincing and show great potential for its utilization in devices that are buried or located at inaccessible places.

APPENDIX A

Appendix

A.1 Permittivities and permeabilities in bi-isotropic medium

In bi-isotropic medium two counter rotating wavefields exist simultaneous, i.e., (E^+,H^+) and (E^-,H^-). These fields see the medium as an equivalent isotropic medium with respective parameters (μ^+, ε^+) and (μ^-, ε^-). These parameters are define in [LSTV94] on page 27 as

$$\mu^+ = \mu(\cos\theta + \kappa_r)e^{-j\theta}, \tag{A.1.1}$$
$$\mu^- = \mu(\cos\theta - \kappa_r)e^{j\theta}, \tag{A.1.2}$$
$$\varepsilon^+ = \varepsilon(\cos\theta + \kappa_r)e^{j\theta}, \tag{A.1.3}$$
$$\varepsilon^- = \varepsilon(\cos\theta - \kappa_r)e^{-j\theta}, \tag{A.1.4}$$

where $\kappa_r = \kappa/\sqrt{\mu_r\varepsilon_r}$

A.2 Euler identities

The complex exponential function can be related to trigonometric functions using Euler's formula

$$e^{jx} = \cos x + j\sin x, \tag{A.2.1}$$

where e is the base of the natural logarithm. Adding and subtracting Euler's formula gives

$$\cos(x) = \mathrm{Re}(e^{jx}) = \frac{e^{jx} + e^{-jx}}{2}, \tag{A.2.2}$$

$$\sin(x) = \mathrm{Im}(e^{jx}) = \frac{e^{jx} - e^{-jx}}{2j}. \tag{A.2.3}$$

List of Publications of the Author

1. S. Khan and T. F. Eibert, "A dual-band metasheet for asymmetric microwave transmission with polarization conversion," IEEE Access, vol. 7, pp. 98045-98052, Jul. 2019.

2. S. Khan and T. F. Eibert, "A multifunctional metamaterial-based dual-band isotropic frequency-selective surface," IEEE Transactions on Antennas and Propagation, vol. 66, no. 8, pp. 4042-4051, Aug. 2018.

3. S. Khan and T. F. Eibert, "Dual-band wireless power transmission using coupled metamaterial resonators for wireless sensor networks," 10th International Conference on Metamaterials, Photonic Crystals and Plasmonics (META), Lisbon, Portugal, 2019, pp. 1627-1628.

4. S. Khan and T. F. Eibert, "An investigation of the mutual coupling and tuning of a miniaturized metamaterial absorber," 13th European Conference on Antennas and Propagation (EuCAP), Krakow, Poland, 2019, pp. 1-4.

5. S. Khan and T. F. Eibert, "A highly efficient miniaturized microwave collector for wireless power transmission," International Applied Computational Electromagnetics Society Symposium (ACES), Denver, CO, 2018, pp. 1-2.

6. S. Khan and T. F. Eibert, "A miniaturized frequency selective surface sub-reflector for X and Ku-bands," 11th German Microwave Conference (GeMiC), Freiburg, 2018, pp. 184-186.

7. S. Khan and T. F. Eibert, "A multi-resonant meta-absorber as an electromagnetic energy harvester," IEEE International Symposium on Antennas and Propagation & USNC/URSI National Radio Science Meeting, San Diego, CA, 2017, pp. 1091-1092.

8. S. Khan and T. F. Eibert, "Complementary metaresonators based X-band hollow waveguide filter and crack detection sensor," 11th European Conference on Antennas and Propagation (EuCAP), Paris, 2017, pp. 2346-2348.

Bibliography

[AAA+17] M. Aboualalaa, A. B. Abdel-Rahman, A. Allam, H. Elsadek, and R. K. Pokharel. Design of a dual-band microstrip antenna with enhanced gain for energy harvesting applications. *IEEE Antennas and Wireless Propagation Letters*, 16:1622–1626, Jan. 2017.

[AB16] S. M. A. M. H. Abadi and N. Behdad. Wideband linear-to-circular polarization converters based on miniaturized-element frequency selective surfaces. *IEEE Transactions on Antennas and Propagation*, 64(2):525–534, Feb. 2016.

[AGF+16] M. Akbari, S. Gupta, M. Farahani, A. R. Sebak, and T. A. Denidni. Gain enhancement of circularly polarized dielectric resonator antenna based on FSS superstrate for mmw applications. *IEEE Transactions on Antennas and Propagation*, 64(12):5542–5546, Dec. 2016.

[AHR15] A. Ali, B. Hu, and O. Ramahi. Intelligent detection of cracks in metallic surfaces using a waveguide sensor loaded with metamaterial elements. *Sensors*, 15(5):11402–11416, 2015.

[AJB10] M. A. Al-Joumayly and N. Behdad. Low-profile, highly-selective, dual-band frequency selective surfaces with closely spaced bands of operation. *IEEE Transactions on Antennas and Propagation*, 58(12):4042–4050, Dec. 2010.

[AJH14] I. F. Akyildiz, J. M. Jornet, and C. Han. Terahertz band: Next frontier for wireless communications. *Physical Communication*, 12:16 – 32, 2014.

[Bal12] C. A. Balanis. *Advanced Engineering Electromagnetics, 2nd Edition*. Wiley, 2012.

[BCL+11] I. H. Baek, S. Y. Choi, H. W. Lee, W. B. Cho, V. Petrov, A. Agnesi, V. Pasiskevicius, D.-Il Yeom, K. Kim, and F. Rotermund. Single-walled carbon nanotube saturable absorber assisted high-power mode-locking of a ti:sapphire laser. *Optics Express*, 19(8):7833–7838, Apr. 2011.

[BE07] M. D. Blech and T. F. Eibert. A dipole excited ultrawideband dielectric rod antenna with reflector. *IEEE Transactions on Antennas and Propagation*, 55(7):1948–1954, Jul. 2007.

[Beh08] N. Behdad. A second-order band-pass frequency selective surface using nonresonant subwavelength periodic structures. *Microwave and Optical Technology Letters*, 50(6):1639–1643, 2008.

[Bro61] W. C. Brown. A survey of the elements of power transmission by microwave beam. *IRE International Convention Record*, 9(3):93–106, 1961.

[BRS+12] J. H. Barton, R. C. Rumpf, R. W. Smith, C. L. Kozikowski, and P. A. Zellner. All-dielectric frequency selective surfaces with few number of periods. *Progress In Electromagnetics Research B*, 41(7):269–283, Jun. 2012.

[BS98] J. C. Bose and R. J. Strutt. On the rotation of plane of polarisation of electric wave by a twisted structure. *Proceedings of the Royal Society of London*, 63(389-400):146–152, 1898.

[CAMP11] F. Costa, C. Amabile, A. Monorchio, and E. Prati. Waveguide dielectric permittivity measurement technique based on resonant FSS filters. *IEEE Microwave and Wireless Components Letters*, 21(5):273–275, May 2011.

[CB13] G. A. Covic and J. T. Boys. Inductive power transfer. *Proceedings of the IEEE*, 101(6):1276–1289, Jun. 2013.

[CC17] Y. Chen and C. Chiu. Maximum achievable power conversion efficiency obtained through an optimized rectenna structure for RF energy harvesting. *IEEE Transactions on Antennas and Propagation*, 65(5):2305–2317, May 2017.

[CCJC10] Q. Cheng, T. J. Cui, W. X. Jiang, and B. G. Cai. An omnidirectional electromagnetic absorber made of metamaterials. *New Journal of Physics*, 12(6):063006, jun 2010.

[CCZ+13] L. Cong, W. Cao, X. Zhang, Z. Tian, J. Gu, R. Singh, J. Han, and W. Zhang. A perfect metamaterial polarization rotator. *Applied Physics Letters*, 103(17):171107, 2013.

[Che11] M. Cheney. *Tesla: Man Out of Time*. Touchstone, 2011.

[Che12] H. T. Chen. Interference theory of metamaterial perfect absorbers. *Optics Express*, 20(7):7165–7172, Mar. 2012.

[CI02] C. Caloz and T. Itoh. Application of the transmission line theory of left-handed (LH) materials to the realization of a microstrip "LH line". In *IEEE Antennas and Propagation Society International Symposium*, volume 2, pages 412–415 vol.2, Jun. 2002.

[CI05] C. Caloz and T. Itoh. *Electromagnetic Metamaterials: Transmission Line Theory and Microwave Applications*. John Wiley & Sons, Inc., 2005.

[CJS+16] M. L. N. Chen, L. J. Jiang, W. E. I. Sha, W. C. H. Choy, and T. Itoh. Polarization control by using anisotropic 3-D chiral structures. *IEEE Transactions on Antennas and Propagation*, 64(11):4687–4694, Nov. 2016.

[CLL+15] C. Chen, Z. Li, L. Liu, J. Xu, P. Ning, B. Xu, X. Chen, and C. Q. Gu. A circularly-polarized metasurfaced dipole antenna with wide axial-ratio beamwidth and RCS reduction functions. *Progress In Electromagnetics Research*, 154:79–85, Nov. 2015.

[CNCG14] Y. Cheng, Y. Nie, Z. Cheng, and R. Z. Gong. Dual-band circular polarizer and linear polarization transformer based on twisted split-ring structure asymmetric chiral metamaterial. *Progress In Electromagnetics Research*, 145:263–272, Mar. 2014.

[CSL10] T. J. Cui, D. R. Smith, and R. Liu. *Metamaterials: Theory, Design, and Applications*. Springer US, 2010.

[CSTom] CST. *CST Microwave Studio*. Computer Simulation Technology, 2016 https://www.cst.com.

[CWCG16] Y. Cheng, C. Wu, Z. Z. Cheng, and R. Z. Gong. Ultra-compact multi-band chiral metamaterial circular polarizer based on triple twisted split-ring resonator. *Progress In Electromagnetics Research*, 155:105–113, Feb. 2016.

[CZP+11] M. Chen, Y. Zhu, Y. Pan, H. Kou, H. Xu, and J. Guo. Gradient multilayer structural design of cnts/sio2 composites for improving microwave absorbing properties. *Materials and Design*, 32(5):3013 – 3016, 2011.

[DCZ16] Xin Duan, Xing Chen, and Lin Zhou. A metamaterial electromagnetic energy rectifying surface with high harvesting efficiency. *AIP Advances*, 6(12):125020, 2016.

[Del12] K. Delihacioglu. Frequency selective surfaces with multiple-strip group elements. *IEEE Antennas and Wireless Propagation Letters*, 11:1370–1373, 2012.

[DLPG07] C. Dietlein, A. Luukanen, Z. Popovi, and E. Grossman. A W-band polarization converter and isolator. *IEEE Transactions on Antennas and Propagation*, 55(6):1804–1809, Jun. 2007.

[DW06] B. W. Drinkwater and P. D. Wilcox. Ultrasonic arrays for non-destructive evaluation: A review. *NDT & E International*, 39(7):525 – 541, 2006.

[EAA15] N. A. Estep, A. N. Askarpour, and A. Alù. Experimental demonstration of negative-index propagation in a rectangular waveguide loaded with complementary split-ring resonators. *IEEE Antennas and Wireless Propagation Letters*, 14:119–122, Sep. 2015.

[EAR17] F. Erkmen, T. S. Almoneef, and O. M. Ramahi. Electromagnetic energy harvesting using full-wave rectification. *IEEE Transactions on Microwave Theory and Techniques*, 65(5):1843–1851, May 2017.

[EFCD10] M. Euler, V. Fusco, R. Cahill, and R. Dickie. Comparison of frequency-selective screen-based linear to circular split-ring polarisation convertors. *IET Microwaves, Antennas Propagation*, 4(11):1764–1772, Nov. 2010.

[EH79] G. F. Engen and C. A. Hoer. Thru-reflect-line: An improved technique for calibrating the dual six-port automatic network analyzer. *IEEE Transactions on Microwave Theory and Techniques*, 27(12):987–993, Dec. 1979.

[FFB+19] A. Froytlog, T. Foss, O. Bakker, G. Jevne, M. A. Haglund, F. Y. Li, J. Oller, and G. Y. Li. Ultra-low power wake-up radio for 5G IoT. *IEEE Communications Magazine*, 57(3):111–117, Mar. 2019.

[FGBV17] O. Fernández, Á. Gómez, J. Basterrechea, and A. Vegas. Reciprocal circular polarization handedness conversion using chiral metamaterials. *IEEE Antennas and Wireless Propagation Letters*, 16:2307–2310, Jun. 2017.

[FM83] P. Franchi and R. Mailloux. Theoretical and experimental study of metal grid angular filters for sidelobe suppression. *IEEE Transactions on Antennas and Propagation*, 31(3):445–450, May 1983.

[FMP+06] V. A. Fedotov, P. L. Mladyonov, S. L. Prosvirnin, A. V. Rogacheva, Y. Chen, and N. I. Zheludev. Asymmetric propagation of electromagnetic waves through a planar chiral structure. *Physical Review Letters*, 97:167401, Oct. 2006.

[FRP12] E. Falkenstein, M. Roberg, and Z. Popovic. Low-power wireless power delivery. *IEEE Transactions on Microwave Theory and Techniques*, 60(7):2277–2286, Jul. 2012.

[FRRM12] G. Franceschetti, P. Rocca, F. Robol, and A. Massa. Innovative rectenna design for space solar power systems. In *IEEE MTT-S International Microwave Workshop Series on Innovative Wireless Power Transmission: Technologies, Systems, and Applications*, pages 151–153, May 2012.

[FS09] A. Foroozesh and L. Shafai. Effects of artificial magnetic conductors in the design of low-profile high-gain planar antennas with high-permittivity dielectric superstrate. *IEEE Antennas and Wireless Propagation Letters*, 8:10–13, 2009.

[GKRW06] M. Gustafsson, A. Karlsson, A. P. P. Rebelo, and B. Widenberg. Design of frequency selective windows for improved indoor outdoor communication. *IEEE Transactions on Antennas and Propagation*, 54(6):1897–1900, Jun. 2006.

[Gla68] P. E. Glaser. Power from the sun: Its future. *Science*, 162(3856):857–861, 1968.

[GLCMB+18] S. Guéry, J.D. Lea-Cox, M.A. Martinez Bastida, B.E. Belayneh, and F. Ferrer-Alegre. Using sensor-based control to optimize soil moisture availability and minimize leaching in commercial strawberry production in spain. *ActaHortic*, 1197:171–178, 2018.

[GLS+19] Q. Guo, Z. Li, J. Su, J. Song, and L. Y. Yang. Active frequency selective surface with wide reconfigurable passband. *IEEE Access*, 7:38348–38355, Mar. 2019.

[GR11] S. M. Goldberg and R. Rosner. Nuclear reactors: Generation to generation. *American Academy of Arts and Sciences*, 2011.

[GS17] S. Ghosh and K. V. Srivastava. An angularly stable dual-band FSS with closely spaced resonances using miniaturized unit cell. *IEEE Microwave and Wireless Components Letters*, 27(3):218–220, Mar. 2017.

[GSZ13] S. Gu, B. Su, and X. Zhao. Planar isotropic broadband metamaterial absorber. *Journal of Applied Physics*, 114(16):163702, 2013.

[GYM+18] X. Gao, W. L. Yang, H. F. Ma, Q. Cheng, X. H. Yu, and T. J. Cui. A reconfigurable broadband polarization converter based on an active metasurface. *IEEE Transactions on Antennas and Propagation*, 66(11):6086–6095, Nov. 2018.

[HH17] M. Hosseini and S. V. Hum. A circuit-driven design methodology for a circular polarizer based on modified jerusalem cross grids. *IEEE Transactions on Antennas and Propagation*, 65(10):5322–5331, Oct. 2017.

[HHS+13] M. Han, M. He, H. J. Sun, K. Zhang, and G. Q. Zhao. A frequency selective surface radome using a coupled resonator filter. In *IEEE International Conference on Microwave Technology Computational Electromagnetics (ICMTCE)*, pages 52–54, Aug. 2013.

[HKC13] A. M. Hawkes, A. R. Katko, and S. A. Cummer. A microwave metamaterial with integrated power harvesting functionality. *Applied Physics Letters*, 103(16):163901, 2013.

[HKS15] T. Haq, M. F. Khan, and O. F. Siddiqui. Design and implementation of waveguide bandpass filter using complementary metaresonator. *Applied Physics A*, 122(1):1–5, 2015.

[HKST15] M. K. Hosain, A. Z. Kouzani, M. F. Samad, and S. J. Tye. A miniature energy harvesting rectenna for operating a head-mountable deep brain stimulation device. *IEEE Access*, 3:223–234, Mar. 2015.

[HOB+06] B. Helifa, A. Oulhadj, A. Benbelghit, I.K. Lefkaier, F. Boubenider, and D. Boutassouna. Detection and measurement of surface cracks in ferromagnetic materials using eddy current testing. *NDT & E International*, 39(5):384 – 390, 2006.

[HRBR14] B. Hu, Z. Ren, M. S. Boybay, and O. M. Ramahi. Waveguide probe loaded with split-ring resonators for crack detection in metallic surfaces. *IEEE Transactions on Microwave Theory and Techniques*, 62(4):871–878, Apr. 2014.

[Ito15] K. Itoh. RF bridge rectifier and its good possibility for wireless power transmission systems. In *IEEE International Symposium on Radio-Frequency Integration Technology (RFIT)*, pages 226–228, Aug. 2015.

[Iva84] V. I. Ivanov. Acoustic emission: some problems, tasks and solutions. *NDT International*, 17(6):323 – 328, 1984.

[JASS18] M. S. Jalali Moghadam, M. Akbari, F. Samadi, and A. Sebak. Wideband cross polarization rotation based on reflective anisotropic surfaces. *IEEE Access*, 6:15919–15925, Mar. 2018.

[JCR55] E. M. T. Jones, S. B. Cohn, and L. A. Robinson. Wide band radomes matched by reactive walls. In *Proceedings of the OSU-WADC radome symposium*, pages 52–67, Jun. 1955.

[JNG+17] A. M. Jawad, R. Nordin, S. K. Gharghan, H. M. Jawad, and M. Ismail. Opportunities and challenges for near-field wireless power transfer: A review. *Energies*, 10(7), Jan. 2017.

[KE17a] S. Khan and T. F. Eibert. Complementary metaresonators based X-band hollow waveguide filter and crack detection sensor. In *11th European Conference on Antennas and Propagation (EUCAP)*, pages 2346–2348, Mar. 2017.

[KE17b] S. Khan and T. F. Eibert. A multi-resonant meta-absorber as an electromagnetic energy harvester. In *IEEE International Symposium on Antennas and Propagation and USNC-URSI Radio Science Meeting*, pages 1091–1092, Jul. 2017.

[KE18] S. Khan and T. F. Eibert. A highly efficient miniaturized microwave collector for wireless power transmission. In *International Applied Computational Electromagnetics Society Symposium (ACES)*, pages 1–2, Mar. 2018.

[KE19a] S. Khan and T. F. Eibert. A dual-band metasheet for asymmetric microwave transmission with polarization conversion. *IEEE Access*, 7(1):98045–98052, Jul. 2019.

[KE19b] S. Khan and T. F. Eibert. Dual-bandwireless power transmission using coupled metamaterial resonators forwireless sensor networks. In *10th International Conference on Metamaterials, Photonic Crystals and Plasmonics (META)*, pages 1–4, Jul. 2019.

[KE19c] S. Khan and T. F. Eibert. An investigation of the mutual coupling and tuning of a miniaturized metamaterial absorber. In *13th European Conference on Antennas and Propagation (EuCAP)*, pages 1–4, Mar. 2019.

[KGR95] D. Kinowski, M. Guglielmi, and A. G. Roederer. Angular bandpass filters: an alternative viewpoint gives improved design flexibility. *IEEE Transactions on Antennas and Propagation*, 43(4):390–395, Apr. 1995.

[KI61] R. Kieburtz and A. Ishimaru. Scattering by a periodically apertured conducting screen. *IRE Transactions on Antennas and Propagation*, 9(6):506–514, Nov. 1961.

[KJA+14] F. Karray, W. M. Jmal, M. Abid, D. El Houssaini, A. M. Obeid, S. M. Qasim, and M. S. BenSaleh. Architecture of wireless sensor nodes for water monitoring applications: From microcontroller-based system to soc solutions. In *5th IMEKO TC19 Symposium*, pages 20–24, 2014.

[KKM05] P. Kildal, A. A. Kishk, and S. Maci. Special issue on artificial magnetic conductors, soft/hard surfaces, and other complex surfaces. *IEEE Transactions on Antennas and Propagation*, 53(1):2–7, Jan. 2005.

[KLL+13] L. B. Kong, Z. W. Li, L. Liu, R. Huang, M. Abshinova, Z. H. Yang, C. B. Tang, P. K. Tan, C. R. Deng, and S. Matitsine. Recent progress in some composite materials and structures for specific electromagnetic applications. *International Materials Reviews*, 58(4):203–259, 2013.

[KLL16] H. K. Kim, D. Lee, and S. Lim. Frequency-tunable metamaterial absorber using a varactor-loaded fishnet-like resonator. *Applied Optics*, 55(15):4113–4118, May 2016.

[Koc48] W. E. Kock. Metallic delay lenses. *The Bell System Technical Journal*, 27(1):58–82, Jan. 1948.

[KON11] T. Kleine-Ostmann and T. Nagatsuma. A review on terahertz communications research. *Journal of Infrared, Millimeter, and Terahertz Waves*, 32(2):143–171, 2011.

[KSK13] H. Kitayoshi, K. Sawaya, and H. Kuwano. Ultra low power wireless ecg sensor tag with wearable antenna. In *IEEE Sensors*, pages 1–4, Nov. 2013.

[KWM+05] D. J. Kern, D. H. Werner, A. Monorchio, L. Lanuzza, and M. J. Wilhelm. The design synthesis of multiband artificial magnetic conductors using high impedance frequency selective surfaces. *IEEE Transactions on Antennas and Propagation*, 53(1):8–17, Jan. 2005.

[KXXP11] L. Ke, Z. Xin, H. Xinyu, and Z. Peng. Analysis and design of multilayer jaumann absorbers. In *IEEE International Conference on Microwave Technology Computational Electromagnetics*, pages 81–84, May 2011.

[KZS+12] G. Kenanakis, R. Zhao, A. Stavrinidis, G. Konstantinidis, N. Katsarakis, M. Kafesaki, C. M. Soukoulis, and E. N. Economou. Flexible chiral metamaterials in the terahertz regime: a comparative study of various designs. *Optical Materials Express*, 2(12):1702–1712, Dec. 2012.

[LA02] D. M. Le Vine and S. Abraham. The effect of the ionosphere on remote sensing of sea surface salinity from space: absorption and emission at L-band. *IEEE Transactions on Geoscience and Remote Sensing*, 40(4):771–782, Apr. 2002.

[LED+04] S. Linden, C. Enkrich, G. Dolling, M. Wegener, J. Zhou, T. Koschny, and C. M. Soukoulis. Magnetic response of metamaterials at 100 terahertz. *Science*, 306(5700):1351–1353, Nov. 2004.

[LED+06] S. Linden, C. Enkrich, G. Dolling, M. W. Klein, J. Zhou, T. Koschny, C. M. Soukoulis, S. Burger, F. Schmidt, and M. Wegener. Photonic metamaterials: Magnetism at optical frequencies. *IEEE Journal of Selected Topics in Quantum Electronics*, 12(6):1097–1105, Nov. 2006.

[Lee71] S. W. Lee. Scattering by dielectric-loaded screen. *IEEE Transactions on Antennas and Propagation*, 19(5):656–665, Sep. 1971.

[LHT+07] G. Q. Luo, W. Hong, H. J. Tang, J. X. Chen, and K. Wu. Dualband frequency-selective surfaces using substrate-integrated waveguide technology. *IET Microwaves, Antennas Propagation*, 1(2):408–413, Apr. 2007.

[LHW+15] Y. Liu, Y. Hao, H. Wang, K. Li, and S. Gong. Low RCS microstrip patch antenna using frequency-selective surface and microstrip resonator. *IEEE Antennas and Wireless Propagation Letters*, 14:1290–1293, Feb. 2015.

[Lin20] K. F. Lindman. Über eine durch ein isotropes system von spiralförmigen resonatoren erzeugte rotationspolarisation der elektromagnetischen wellen. *Annalen der Physik*, 368(23):621–644, 1920.

[LS13] B. Li and Z. Shen. Synthesis of quasi-elliptic bandpass frequency-selective surface using cascaded loop arrays. *IEEE Transactions on Antennas and Propagation*, 61(6):3053–3059, Jun. 2013.

[LSM+08] N. I. Landy, S. Sajuyigbe, J. J. Mock, D. R. Smith, and W. J. Padilla. Perfect metamaterial absorber. *Physical Review Letters*, 100:207402, May 2008.

[LSTV94] I. V. Lindell, A. H. Sihvola, S. A. Tretyakov, and A. J. Viitanen. *Electromagnetic Waves in Chiral and Bi-isotropic Media*. Artech House, Boston, 1994.

[LWLG16] H. P. Li, G. M. Wang, J.-G. Liang, and X.-J. Gao. Wideband multifunctional metasurface for polarization conversion and gain enhancement. *Progress In Electromagnetics Research*, 155:115–125, May 2016.

[LWZ+10] H. Li, B. Z. Wang, G. Zheng, W. Shao, and L. Guo. A reflectarray antenna backed on FSS for low RCS and high radiation performances. *Progress In Electromagnetics Research C*, 15:145–155, Aug. 2010.

[LYMP04] Y. J. Lee, J. Yeo, R. Mittra, and W. S. Park. Design of a high-directivity electromagnetic band gap (ebg) resonator antenna using a frequency-selective surface (FSS) superstrate. *Microwave and Optical Technology Letters*, 43(6):462–467, 2004.

[LZG15] Z. Liu, Z. Zhong, and Y. Guo. Enhanced dual-band ambient RF energy harvesting with ultra-wide power range. *IEEE Microwave and Wireless Components Letters*, 25(9):630–632, Sep. 2015.

[LZL+17] X. Liu, J. Zhang, W. Li, R. Lu, L. Li, Z. Xu, and A. Zhang. Three-band polarization converter based on reflective metasurface. *IEEE Antennas and Wireless Propagation Letters*, 16:924–927, Apr. 2017.

[LZZ15] X. Lu, L. Zhang, and T. Zhang. Nanoslit-microcavity-based narrow band absorber for sensing applications. *Optics Express*, 23(16):20715–20720, Aug. 2015.

[Mal51] G. D. Malyuzhinets. A note on the radiation principle. *Zhurnal Technicheskoi Fiziki*, 21:940–942, 1951.

[Man45] L. Mandlshtam. Group velocity in a crystal lattice. *Zhurnal Eksperimentalnoii Teoreticheskoi Fiziki*, 15:476–478, 1945.

[MCT+09] B. Merabet, F. Costa, H. Takhedmit, C. Vollaire, B. Allard, L. Cirio, and O. Picon. A 2.45-ghz localized elements rectenna. In *3rd IEEE International Symposium on Microwave, Antenna, Propagation and EMC Technologies for Wireless Communications*, pages 419–422, Oct. 2009.

[MF19] G. Marconi and C. S. Franklin. Reflector for use in wireless telegraphy and telephony, Apr. 1919. U.S. Patent, 1,301,473.

[Mit04] R. Mittra. A look at some challenging problems in computational electromagnetics. *IEEE Antennas and Propagation Magazine*, 46(5):18–32, Oct. 2004.

[MML02] A. Monorchio, G. Manara, and L. Lanuzza. Synthesis of artificial magnetic conductors by using multilayered frequency selective surfaces. *IEEE Antennas and Wireless Propagation Letters*, 1:196–199, 2002.

[MMZ09] L. Mingyun, H. Minjie, and W. Zhe. Design of multi-band frequency selective surfaces using multi-periodicity combined elements. *Journal of Systems Engineering and Electronics*, 20(4):675–680, Aug. 2009.

[MTS11] G. Monti, L. Tarricone, and M. Spartano. X-band planar rectenna. *IEEE Antennas and Wireless Propagation Letters*, 10:1116–1119, 2011.

[Mun05] B. A. Munk. *Frequency Selective Surfaces: Theory and Design*. John Wiley & Sons, Inc., USA, 2005.

[Mun09] B. A. Munk. *Metamaterials: Critique and Alternatives*. John Wiley & Sons, Inc., USA, 2009.

[MVVA11] V. Marian, C. Vollaire, J. Verdier, and B. Allard. Potentials of an adaptive rectenna circuit. *IEEE Antennas and Wireless Propagation Letters*, 10:1393–1396, 2011.

[MYC92] J. O. McSpadden, T. Yoo, and K. Chang. Theoretical and experimental investigation of a rectenna element for microwave power transmission. *IEEE Transactions on Microwave Theory and Techniques*, 40(12):2359–2366, Dec. 1992.

[NKJ+13] K. Niotaki, S. Kim, S. Jeong, A. Collado, A. Georgiadis, and M. M. Tentzeris. A compact dual-band rectenna using slot-loaded dual band folded dipole antenna. *IEEE Antennas and Wireless Propagation Letters*, 12:1634–1637, 2013.

[NS71] Y. Naito and K. Suetake. Application of ferrite to electromagnetic wave absorber and its characteristics. *IEEE Transactions on Microwave Theory and Techniques*, 19(1):65–72, Jan. 1971.

[NSS17] M. Nafe, A. Syed, and A. Shamim. Gain-enhanced on-chip folded dipole antenna utilizing artificial magnetic conductor at 94 GHz. *IEEE Antennas and Wireless Propagation Letters*, 16:2844–2847, Sep. 2017.

[OKPJ67] R. H. Ott, R. G. Kouyoumjian, and L. Peters Jr. Scattering by a two-dimensional periodic array of narrow plate. *Radio Science*, 2(11):1347–1359, 1967.

[OS16] A. A. Omar and Z. Shen. Multiband high-order bandstop 3-D frequency-selective structures. *IEEE Transactions on Antennas and Propagation*, 64(6):2217–2226, Jun. 2016.

[OS17] A. A. Omar and Z. Shen. Thin bandstop frequency-selective structures based on loop resonator. *IEEE Transactions on Microwave Theory and Techniques*, 65(7):2298–2309, Jul. 2017.

[Pea12] J. M. Pearce. Limitations of nuclear power as a sustainable energy source. *Sustainability*, 4(6):1173–1187, 2012.

[Pet11] A. Petrin. *Wave Propagation*. InTech, 2011.

[PHRS99] J. B. Pendry, A. J. Holden, D. J. Robbins, and W. J. Stewart. Magnetism from conductors and enhanced nonlinear phenomena. *IEEE Transactions on Microwave Theory and Techniques*, 47(11):2075–2084, Nov. 1999.

[PHSY96] J. B. Pendry, A. J. Holden, W. J. Stewart, and I. Youngs. Extremely low frequency plasmons in metallic mesostructures. *Physical Review Letters*, 76:4773–4776, Jun. 1996.

[PM74] E. Pelton and B. Munk. A streamlined metallic radome. *IEEE Transactions on Antennas and Propagation*, 22(6):799–803, Nov. 1974.

[PMM13] E. Popovici, M. Magno, and S. Marinkovic. Power management techniques for wireless sensor networks: A review. In *5th IEEE International Workshop on Advances in Sensors and Interfaces IWASI*, pages 194–198, Jun. 2013.

[Poz11] D. M. Pozar. *Microwave Engineering, 4th Edition*. Wiley, 2011.

[PPSM17] N. Pires, T. Parra, A. K. Skrivervik, and A. A. Moreira. Design and measurement of a differential printed antenna for a wireless sensor network node. *IEEE Antennas and Wireless Propagation Letters*, 16:2228–2231, May 2017.

[RAAB12] O. M. Ramahi, T. S. Almoneef, M. AlShareef, and M. S. Boybay. Metamaterial particles for electromagnetic energy harvesting. *Applied Physics Letters*, 101(17):173903, 2012.

[Sav05] P. Saville. *Review of Radar Absorbing Materials*. Defence R & D Canada - Atlantic, Dartmouth NS (CAN), 2005.

[SB07] K. Sarabandi and N. Behdad. A frequency selective surface with miniaturized elements. *IEEE Transactions on Antennas and Propagation*, 55(5):1239–1245, May 2007.

[Sem83] B. A. Semenov. Nuclear power in the soviet union. *International Atomic Energy Agency Bulletin*, 25(2):47 – 59, 1983.

[SGD+15] M. Srbinovska, C. Gavrovski, V. Dimcev, A. Krkoleva, and V. Borozan. Environmental parameters monitoring in precision agriculture using wireless sensor networks. *Journal of Cleaner Production*, 88:297 – 307, 2015. Sustainable Development of Energy, Water and Environment Systems.

[SGHZ13] H. Sun, Y. Guo, M. He, and Z. Zhong. A dual-band rectenna using broadband yagi antenna array for ambient RF power harvesting. *IEEE Antennas and Wireless Propagation Letters*, 12:918–921, 2013.

[Sie08] D. Sievenpiper. *Modern Antenna Handbook*, chapter Artificial Impedance Surfaces, pages 737–777. John Wiley & Sons, USA, 2008.

[SIP14] B. Sanz-Izquierdo and E. A. Parker. Dual polarized reconfigurable frequency selective surfaces. *IEEE Transactions on Antennas and Propagation*, 62(2):764–771, Feb. 2014.

[Siv57] D. V. Sivukhin. The energy of electromagnetic waves in dispersive media. *Opt. Spektrosk.*, 3:308–312, 1957.

[SK15] R. Sivasamy and M. Kanagasabai. A novel dual-band angular independent FSS with closely spaced frequency response. *IEEE Microwave and Wireless Components Letters*, 25(5):298–300, May 2015.

[Sko90] M. I. Skolnik. *Radar Handbook*. McGraw-Hill, New York, 1990.

[SM98] N. Shinohara and H. Matsumoto. Experimental study of large rectenna array for microwave energy transmission. *IEEE Transactions on Microwave Theory and Techniques*, 46(3):261–268, Mar. 1998.

[SPV+00] D. R. Smith, W. J. Padilla, D. C. Vier, S. C. Nemat-Nasser, and S. Schultz. Composite medium with simultaneously negative permeability and permittivity. *Physical Review Letters*, 84:4184–4187, May 2000.

[SSC+14] J. Shin, M. Seo, J. Choi, J. So, and C. Cheon. A compact and wideband circularly polarized rectenna with high efficiency at X-band. *Progress In Electromagnetics Research*, 145:163–173, Mar. 2014.

[SSS01] R. A. Shelby, D. R. Smith, and S. Schultz. Experimental verification of a negative index of refraction. *Science*, 292(5514):77–79, 2001.

[SZG13] H. Sun, Z. Zhong, and Y. Guo. An adaptive reconfigurable rectifier for wireless power transmission. *IEEE Microwave and Wireless Components Letters*, 23(9):492–494, Sep. 2013.

[THC07] W. Tu, S. Hsu, and K. Chang. Compact 5.8-GHz rectenna using stepped-impedance dipole antenna. *IEEE Antennas and Wireless Propagation Letters*, 6:282–284, 2007.

[THC13] W. Tian, X. Hou, and Y. Che. The analysis and measurement of FSS radome for antenna RCS reduction. In *Cross Strait Quad-Regional Radio Science and Wireless Technology Conference (CSQRWC), 2013*, pages 297–299, Jul. 2013.

[Ves68] V. G Veselago. the electrodynamics of substances with simultaneously negative values of ϵ and μ. *Soviet Physics Uspekhi*, 10(4):509–514, apr 1968.

[VHS93] J. C. Vardaxoglou, A. Hossainzadeh, and A. Stylianou. Scattering from two-layer FSS with dissimilar lattice geometries. *IEE Proceedings H - Microwaves, Antennas and Propagation*, 140(1):59–61, Feb. 1993.

[Voc] International Electrotechnical Vocabulary. International electrotechnical commission. accessed: 05 august, 2019. available: http://www.electropedia.org/.

[WC16] H. B. Wang and Y. J. Cheng. Frequency selective surface with miniaturized elements based on quarter-mode substrate integrated waveguide cavity with two poles. *IEEE Transactions on Antennas and Propagation*, 64(3):914–922, Mar. 2016.

[WCS+07] T. Wark, P. Corke, P. Sikka, L. Klingbeil, Y. Guo, C. Crossman, P. Valencia, D. Swain, and G. Bishop-Hurley. Transforming agriculture through pervasive wireless sensor networks. *IEEE Pervasive Computing*, 6(2):50–57, Apr. 2007.

[WM99] D. S. Weile and E. Michielssen. Design of doubly periodic filter and polarizer structures using a hybridized genetic algorithm. *Radio Science*, 34(1):51–63, 1999.

[Wu14] T. K. Wu. Improved bandpass FSS for wireless communications. In *USNC-URSI Radio Science Meeting (Joint with AP-S Symposium)*, pages 153–153, Jul. 2014.

[WXZ+19] S. Wu, S. Xu, T. L. Zinenko, V. V. Yachin, S. L. Prosvirnin, and V. R. Tuz. 3-D printed chiral metasurface as a dichroic dual-band polarization converter. *Optics Letters*, 44(4):1056–1059, Feb. 2019.

[WYD+14] R. Wang, D. Ye, S. Dong, Z. Peng, Y. Salamin, F. Shen, J. Huangfu, C. Li, and L. Ran. Optimal matched rectifying surface for space solar power satellite applications. *IEEE Transactions on Microwave Theory and Techniques*, 62(4):1080–1089, Apr. 2014.

[XHLZ13] H. Xiong, J. S. Hong, C. M. Luo, and L. L. Zhong. An ultrathin and broadband metamaterial absorber using multi-layer structures. *Journal of Applied Physics*, 114(6):064109, 2013.

[XZZW08] R. R. Xu, H. C. Zhao, Z. Y. Zong, and W. Wu. Dual-band capacitive loaded frequency selective surfaces with close band spacing. *IEEE Microwave and Wireless Components Letters*, 18(12):782–784, Dec. 2008.

[Yee93] J. S. Yee. Frequency selective surface (FSS), May 1993. U.S. Patent, 5,208,603.

[YRWR17] P. S. Yedavalli, T. Riihonen, X. Wang, and J. M. Rabaey. Far-field RF wireless power transfer with blind adaptive beamforming for internet of things devices. *IEEE Access*, 5:1743–1752, Feb. 2017.

[YWM+16] M. Yan, J. Wang, H. Ma, M. Feng, Y. Pang, S. Qu, J. Zhang, and L. Zheng. A tri-band, highly selective, bandpass FSS using cascaded multilayer loop arrays. *IEEE Transactions on Antennas and Propagation*, 64(5):2046–2049, May 2016.

[YZXYJ14] Z. Yu, S. Zhong-Xiang, and F. Yi-Jun. Frequency-selective microwave polarization rotator using substrate-integrated waveguide cavities. *Chinese Physics B*, 23(3):034101, 2014.

[ZCC+13] J. Zhao, Q. Cheng, J. Chen, M. Q. Qi, W. X. Jiang, and T. J. Cui. A tunable metamaterial absorber using varactor diodes. *New Journal of Physics*, 15(4):043049, Apr. 2013.

[ZCZ+18] R. Zhao, H. Y. Chen, L. Zhang, F. Li, P. Zhou, J. Xie, and L.-J. Deng. Design and implementation of high efficiency and broadband transmission-type polarization converter based on diagonal split-ring resonator. *Progress In Electromagnetics Research*, 161:1–10, Feb. 2018.

[ZHW+14] X. C. Zhu, W. Hong, K. Wu, H. J. Tang, Z. C. Hao, J. X. Chen, H. X. Zhou, and H. Zhou. Design of a bandwidth-enhanced polarization rotating frequency selective surface. *IEEE Transactions on Antennas and Propagation*, 62(2):940–944, Feb. 2014.

[ZLL18] X. Zhang, H. Liu, and L. Li. Electromagnetic power harvester using wide-angle and polarization-insensitive metasurfaces. *Applied Sciences*, 8(4), Mar. 2018.

[ZPGC19] Z. Zhang, H. Pang, A. Georgiadis, and C. Cecati. Wireless power transfer—an overview. *IEEE Transactions on Industrial Electronics*, 66(2):1044–1058, Feb. 2019.

[ZQM+18] Y. Zhao, A. Qing, Y. Meng, Z. Song, and C. Lin. Dual-band circular polarizer based on simultaneous anisotropy and chirality in planar metamaterial. *Scientific Reports*, 8(1729), Jan. 2018.

[ZSA02] S. Zouhdi, A. Sihvola, and M. Arsalane. *Advances in Electromagnetics of Complex Media and Metamaterials*. Springer, 2002.

[ZZHM17] Y. Zhang, J. Zhu, C. Huang, and S. Ma. Wide-band and high-efficiency 90° polarization rotator based on tri-layered perforated metal films. *Journal of Lightwave Technology*, 35(21):4817–4823, Nov. 2017.